Modelling, simulation and optimal control of dielectric elastomer actuated systems

Modellbildung, Simulation und Optimalsteuerung von Systemen mit dielektrischen Elastomeraktoren

Der Technischen Fakultät
der Friedrich-Alexander-Universität
Erlangen-Nürnberg

zur

Erlangung des Doktorgrades Dr.-Ing.
vorgelegt von

Tristan Schlögl

aus Freiburg im Breisgau

Als Dissertation genehmigt
von der Technischen Fakultät
der Friedrich-Alexander-Universität Erlangen-Nürnberg

Tag der mündlichen Prüfung: 26. Februar 2018

Vorsitzender des Promotionsorgans: Prof. Dr.-Ing. Reinhard Lerch

Gutachter/in: Prof. Dr.-Ing. habil. Sigrid Leyendecker
Prof. Dr.-Ing. Ralf Müller

Herausgeber

Prof. Dr.-Ing. habil. Sigrid Leyendecker
Lehrstuhl für Technische Dynamik
Friedrich-Alexander-Universität Erlangen-Nürnberg
Immerwahrstraße 1
91058 Erlangen

Modelling, simulation and optimal control of dielectric elastomer actuated systems

Tristan Schlögl

Schriftenreihe Technische Dynamik
Band 3 2018
Herausgeber: Prof. Dr.-Ing. habil. Sigrid Leyendecker

Vorwort

Diese Arbeit entstand während meiner Tätigkeit als wissenschaftlicher Mitarbeiter bei Frau Prof. Dr.-Ing. habil. Sigrid Leyendecker am Lehrstuhl für Technische Dynamik an der Friedrich-Alexander-Universität Erlangen-Nürnberg im Rahmen des durch das Bayerische Landesamt für Umwelt geförderten Projekts Bionicum Forschung – Künstliche Muskeln.

Besonders danken möchte ich Frau Prof. Dr.-Ing. habil. Sigrid Leyendecker für die umfassende und fachlich intensive Betreuung meiner wissenschaftlichen Arbeit, die Ermöglichung der vielen spannenden Konferenzbesuche und das entgegengebrachte Vertrauen. Mein Dank gilt zudem Herrn Prof. Dr.-Ing. Ralf Müller für die Begutachtung meiner Arbeit, Herrn Prof. Dr.-Ing. Dietmar Drummer für die Übernahme des Prüfungsvorsitzes und Herrn Prof. Dr. Michael Stingl für die Mitwirkung in der Prüfungskommission.

Danken möchte ich außerdem meinen Kollegen am Lehrstuhl für Technische Dynamik und am benachbarten Lehrstuhl für Technische Mechanik für den kreativen Austausch, insbesondere meinen Bürokollegen Tobias Gail und Johann Penner für die angenehme Arbeitsatmosphäre, sowie Frau Beate Hegen für die Unterstützung in allen Lebenslagen.

Dem gesamten Bionicum-Team, insbesondere Herrn Dr. Korbinian Freier und Frau Dr. Eva Gebauer danke ich für die Organisation der zahlreichen Doktorandenseminare und den regen Austausch auch über den Tellerrand hinaus. Bedanken möchte ich mich auch bei den Bionicum-Kollegen Sebastian Reitelshöfer und Max Landgraf vom Lehrstuhl für Fertigungsautomatisierung und Produktionssystematik für die angenehme Zusammenarbeit.

Ein unendlich großer Dank gilt abschließend meiner gesamten Familie, die mich die ganzen Jahre unterstützt und an mich geglaubt hat, insbesondere meinen Eltern und meiner Freundin Stefanie.

Erlangen, im März 2018 Tristan Schlögl

Kurzfassung

Modellbildung, Simulation und Optimalsteuerung von Systemen mit dielektrischen Elastomeraktoren

Ziel der vorliegenden Arbeit ist der Aufbau eines Simulationsmodells zur Beschreibung und Steuerung des zeitabhängigen Verhaltens von Mehrkörpersystemen, die durch künstliche Muskeln angetrieben werden. Die künstlichen Muskeln bestehen aus gestapelten dielektrischen Elastomeraktoren, welche aufgrund elektrostatischer Kräfte beim Anlegen einer elektrischen Spannung kontrahieren. Die Beschreibung der Wechselwirkung zwischen mechanischen und elektrischen Größen macht einen domänenübergreifenden Modellierungsansatz erforderlich. Bestehende elektromechanisch gekoppelte Simulationsmodelle für dielektrische Elastomeraktoren können in zwei Gruppen eingeteilt werden. Die Modelle der ersten Gruppe basieren auf räumlichen Feldgleichungen, welche elektromagnetische Kräfte in verformbaren Kontinua mit beliebiger Geometrie beschreiben. Die zweite Gruppe enthält reduzierte Modelle mit konzentrierten Parametern, welche physikalisch komplexe Sachverhalte durch die Ausnutzung von Symmetrien, Regelmäßigkeiten und dem zu erwartenden Verhalten in räumlich diskreten Zustandsvariablen verdichten. Beide Ansätze liefern üblicherweise voneinander abweichende Simulationsergebnisse, da sie auf unterschiedlichen Annahmen, Materialmodellen und Modellierungsansätzen beruhen. Im Rahmen dieser Arbeit wird durch die Herleitung eines energiekonsistenten reduzierten Modells direkt aus der räumlichen Feldtheorie versucht, zwischen den beiden Gruppen eine Brücke zu schlagen. Da beide Modelle in der Folge auf den selben theoretischen Grundlagen beruhen, können sie besonders gut miteinander verglichen werden.

Die Arbeit beginnt mit der Einführung einer zeitabhängigen, vielseitigen und monolitischen, dreidimensionalen finite Elemente Formulierung für das elektromechanisch gekoppelte Problem der Beschreibung eines künstlichen Muskels. Ein variationelles Zeitintegrationsschema gewährleistet Strukturerhaltung in der dynamischen Simulation, sowie ein ausgesprochen gutes Energieverhalten. Flexibilität und Modularität werden durch einen elektromechanisch gekoppelten, visko-hyperelastischen Materialansatz sichergestellt. Der künstliche Muskel wird mit einem Mehrkörpersystem gekoppelt, welches die aktuierte Struktur repräsentiert. Dieser Aufbau ermöglicht es, das komplexe Verhal-

ten humanoider Strukturen zu untersuchen, die durch künstliche Muskeln anstatt durch Elektromotoren angetrieben werden. Das Mehrkörpersystem besteht aus Starrkörpern, die durch Gelenke miteinander verbunden sind. Mittels einer redundanten Formulierung werden rotatorische Freiheitsgrade und damit einhergehende Singularitäten vermieden. Als unmittelbare Folge dieser Wahl bekommt die Kopplung zwischen dem Mehrkörpersystem und dem finite Elemente Muskelmodell einen sehr modularen Charakter. Der Aufbau der Mehrkörpersysteme und die Herleitung der relevanten Gleichungen wird von der C++ Bibliothek MulDi unterstützt, welche im Rahmen dieser Arbeit entstanden ist. Um durch künstliche Muskeln aktuierte Systeme zu steuern und dabei Schwingungen zu vermeiden, die mit der elastischen Struktur der Aktoren einhergehen, wird die Theorie der Optimalsteuerung angewandt. Da die Lösung von Optimalsteuerungsproblemen sehr rechenintensiv ist, wird ein reduziertes, energiekonsistentes Muskelmodell mit konzentrierten Parametern hergeleitet. Numerische Beispiele zeigen potentielle Anwendungen.

Das verwendete variationelle Zeitintegrationsschema hat sich zur Lösung der in dieser Arbeit anfallenden elektromechanisch gekoppelten Probleme als besonders geeignet erwiesen. Neben den guten Struktur- und Energieerhaltungseigenschaften erlaubt es der variationelle Integrator, algebraische Nebenbedingungen auf Konfigurationsebene auf den diskreten Zeitknoten exakt zu erfüllen. Dies ermöglicht eine driftfreie Kopplung zwischen dem Mehrkörpersystem und den künstlichen Muskeln. Darüber hinaus kann vollständig inkompressibles Materialverhalten elegant erzwungen werden, ohne dass dabei volumetrische ‘Locking’-Effekte auftreten. Numerische Beispiele machen deutlich, dass die im Vergleich mit echten Muskeln relativ kleinen maximal erzielbaren Kontraktionen und Kräfte dielektrischer Stapelaktoren deren Anwendung in humanoiden Strukturen bisher stark einschränken. Die Anwendung der Optimalsteuerung hat sich jedoch als adäquates Mittel herausgestellt, um die mit der elastischen Natur der künstlichen Muskeln einhergehenden Schwingungen effektiv zu vermeiden.

Abstract

The aim of this work is to present a physically motivated simulation framework to predict and control the time dependent behaviour of multibody systems that are actuated via artificial muscles. The artificial muscles are composed of stacked dielectric elastomers that contract due to electrostatic forces when a voltage is applied. As both electrical and mechanical quantities are involved in this interrelation, a multidisciplinary modelling approach is required. Existing electromechanically coupled models for dielectric elastomers can be categorised in two groups. The first group covers general three-dimensional field theory of electromagnetic forces in deformable continua with arbitrary geometry. The second group contains so called lumped parameter models, where spatially discrete configuration variables condense the complex physical relationships by exploiting symmetries, regularities and predicted behaviour. Both approaches are usually based on different assumptions, material models and modelling procedures, resulting in different simulation results. This work tries to bridge these two groups by deriving an energy consistent lumped parameter model directly from the corresponding three dimensional field theory. As both models consequently share the same modelling approach, they can be easily compared and assessed.

The present work starts by introducing a time dependent, versatile and monolithic three-dimensional finite element formulation for the electromechanically coupled problem that serves as the artificial muscle model. A variational time integration scheme ensures structure preservation as well as a good energy behaviour. An electromechanically coupled, visco-hyperelastic material approach provides flexibility and modularity. The artificial muscle model is coupled with a multibody system that represents the actuated structure. This setting allows for exploring the complex behaviour of humanoid structures that are driven by artificial muscles instead of electrical drives. The multibody system is composed of rigid bodies that are connected via joints and based on a redundant formulation that avoids rotational degrees of freedom and singularities. As a result, a very modular coupling between the multibody system and the finite element muscle is obtained. The set-up of multibody systems and the derivation of relevant equations is supported by the C++ library MulDi that emerged from this work. In order to control artificial muscle actuated systems and possibly avoid oscillations that are inherent with the elastic structure of

the actuators, optimal control theory is utilised. To reduce the computational cost that is necessary to solve optimal control problems, an energy consistent lumped parameter model for dielectric elastomers is derived, where numerical examples illustrate potential applications.

The utilised variational time integration scheme turned out to be very suitable for solving electromechanically coupled problems. Apart from the preservation characteristics and the good energy behaviour, the integrator allows to solve algebraic constraints on configuration level exactly at the discrete time nodes. This allows for a neat coupling between the artificial muscles and the actuated structure. Moreover, fully incompressible material behaviour can be obtained, avoiding volumetric locking effects. Numerical examples show that the rather small achievable maximum contraction and forces of stacked actuators compared to real muscles still limit their use in human like structures. Optimal control theory, however, has been proven to provide a suitable tool for avoiding oscillations that are inherent with the elastic nature of the actuators and yields optimised voltage control trajectories.

Contents

List of symbols

$(\bullet)^{\diamond}$	isochoric component
$(\bullet)^{\circ}$	volumetric component
$(\bullet)_{\mathrm{el}}, (\bullet)^{\mathrm{el}}$	finite element quantities on a cell
$\bar{(\bullet)}$	externally prescribed quantity
$(\bullet)_r$	finite element quantities
$(\bullet)_s$	multibody system quantities
A	material area
a	spatial area
$\boldsymbol{b}_0$	material volume force density
$\mathcal{B}_0$	material configuration space
$\mathcal{B}_t$	spatial configuration space
$\underline{c}$	optimisation constraints
$\boldsymbol{C}$	right Cauchy-Green tensor
$\boldsymbol{\chi}$	deformation map
$\mathfrak{d}$	spatial electric displacement
$\boldsymbol{D}$	material electric displacement
$\boldsymbol{d}$	rigid body director
DEA	dielectric elastomer actuator
Δt	time step size
$\boldsymbol{E}$	material electric field
$\boldsymbol{e}$	spatial electric field

e	spatial electric field magnitude
ε_0	vacuum permittivity
ε_r	relative permittivity
η	damping parameter
$\underline{F}$	structure preserving integration scheme residuum
$\boldsymbol{F}$	deformation gradient
$\underline{f}^{\text{ext}}$	non-conservative generalised forces
W^{ext}	work of non-conservative contributions
$\underline{g}$	constraints
$\underline{\underline{G}}$	constraint Jacobian
$\underline{\underline{G}}_d$	discrete constraint Jacobian
$\boldsymbol{g}_{\text{v}}$	gravitation vector
H	total energy
$\underline{\underline{H}}_d$	discrete Jacobian of multibody system constraints
$\underline{h}_{\text{int}}$	internal rigid body constraints for directors
$\underline{h}_{\text{joint}}$	multibody system joint constraints
$\mathbf{1}$	3×3 identity matrix
$\underline{\underline{1}}$	6×6 identity matrix
$\tilde{\underline{\underline{1}}}$	space filling identity matrix
$\mathcal{J}$	objective function
$\boldsymbol{J}$	rigid body inertia tensor
J	determinant of the deformation gradient
$\underline{\underline{K}}$	structure preserving integration scheme matrix
κ	bulk modulus
$\mathcal{L}$	Lagrangian density
L	Lagrangian

$\underline{\lambda}$	Lagrange multipliers
L_d	discrete Lagrangian
$\underline{\underline{M}}$	mass matrix
m	mass
μ, λ	Lamé parameters
$\boldsymbol{N}$	material surface normal
$\boldsymbol{n}$	spatial surface normal
$\underline{N}_{\mathrm{el}}^{\mathrm{ele}}$	finite element shape functions for scalar electrical degrees of freedom
$\underline{\boldsymbol{N}}_{\mathrm{el}}^{\mathrm{trans}}$	finite element shape functions for translational vector valued degrees of freedom
ν	Poisson's ratio
Ω	electromechanically coupled potential energy density
p	electrostatic pressure
$\boldsymbol{P}^{\mathrm{ela}}$	conservative elastic first Piola-Kirchhoff stress
$\boldsymbol{P}^{\mathrm{ele}}$	electrostatic stress tensor
Φ	material potential energy density
ϕ	electric potential
$\boldsymbol{\varphi}$	rigid body centre of gravity vector
Π	potential energy
$\boldsymbol{P}^{\mathrm{mech}}$	first Piola-Kirchhoff stress tensor
$\underline{p}_n$	discrete conjugate momenta
$\boldsymbol{P}^{\mathrm{pol}}$	material polarisation vector
$\boldsymbol{p}^{\mathrm{pol}}$	spatial polarisation vector
$\boldsymbol{P}^{\mathrm{tot}}$	electromechanically coupled first Piola-Kirchhoff stress tensor
$\boldsymbol{P}^{\mathrm{vis}}$	viscous first Piola-Kirchhoff stress
$\bar{Q}$	externally applied surface charge density

$\underline{q}$	spatially discrete configuration
$\underline{q}^{\min}$	configuration in minimal coordinates
$\underline{q}_n$	time discrete configuration
$\underline{r}$	discrete finite element configuration
ρ	spatial mass density
ρ_0	material mass density
$\underline{s}$	multibody system configuration
S	action
$\boldsymbol{\sigma}$	Cauchy stress tensor
$\boldsymbol{\sigma}^{\text{elec}}$	spatial Maxwell stress tensor
$\mathcal{T}$	kinetic energy density
$\underline{\underline{T}}$	null space matrix
T	kinetic energy
$\bar{\boldsymbol{T}}$	surface traction
$\boldsymbol{\Theta}$	rigid body Euler tensor
t	continuous time
t_n	discrete time node
$\underline{u}$	control variables
$\boldsymbol{u}$	displacement vector
V	material volume
v	spatial volume
$\underline{x}$	optimisation variables
$\boldsymbol{X}$	material point
$\boldsymbol{x}$	spatial point
$\underline{x}_l, \underline{x}_u$	optimisation variable bounds
Y	Young's modulus

List of Figures

List of Tables

1 Introduction

Modern robotic systems still suffer some severe limitations with regard to their efficiency concerning energy and resources. Due to the high weight of electrical drives and portable batteries, they are far from being autarkic for longer times. Furthermore, the rigid coupling between electrical drives and joints does not allow for dynamic motions like they occur in nature, where flexible muscles act as an energy buffer. Due to their potential capability of solving some of these problems, dielectric elastomer actuators (DEAs) are the subject of intense research [Carp15, BC00, Zhan02, Zhan05] and many possible applications like animated toys [Korn07] and compression bandages [Lars13, MF11] are already patented.

DEAs are composed of an elastic dielectric material that is sandwiched between two compliant electrodes, as illustrated in Figure 1.1. When the electrodes are charged by applying an electric potential, charges with opposite signs attract each other, leading to a contractive force also known as electrostatic pressure [Pelr98]. When several DEA cells are stacked on top of each other, resulting in a pile-up configuration, the electrostatic pressure provides macroscopically useful displacements [Kova09]. Stacked DEAs are also referred to as artificial muscles, because they bear analogy to the behaviour of skeletal muscles in terms of contracting in length direction when stimulated.

Figure 1.2 illustrates the use of DEAs in prototypes. The idea of using artificial muscles as sophisticated actuators offers a broad variety of potential applications [Korn07]. The elastic structure acts as an energy storage and allows for dynamic motion [Fox09, Xu12] and safe human interaction. Compared to

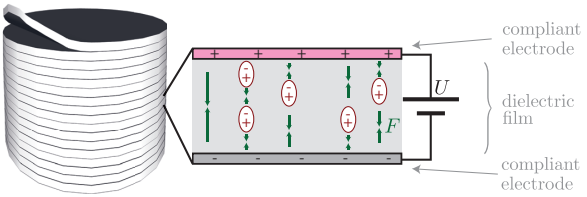

Figure 1.1: Stacked dielectric elastomer actuator with functional principle.

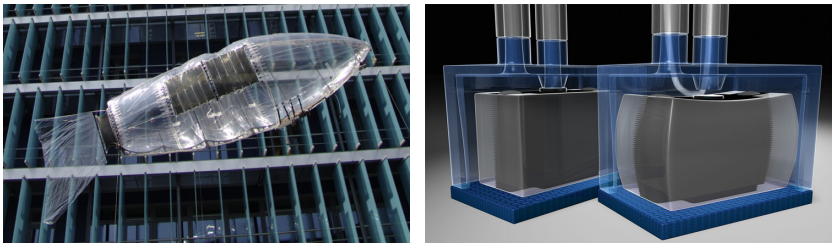

(a) Fish-like propulsion of a dielectric elastomer actuated airship [Jord10a].

(b) Festo DIELASTAR[1] project, dielectric elastomer actuated valves.

Figure 1.2: Dielectric elastomer actuator applications.

commonly used electrical drives, no gearbox is necessary and the operation is noiseless [BC00]. Due to the high efficiency, artificial muscles allow to build autarkic systems in contrast to pneumatic or hydraulic systems. However, the use of elastic actuators is also accompanied by new control challenges. Advanced control strategies need to avoid undesirable oscillations, bring the system as quickly as possible into its steady state and follow prescribed trajectories as close as possible.

Within the collaborative research project Bionicum[2], the use of artificial muscles in humanoid systems is investigated at the Friedrich-Alexander University Erlangen-Nuremberg. At the Institute for Factory Automation and Production Systems (FAPS), the development of the automated production of multilayer DEAs together with lightweight power electronics is explored [Reit13a, Reit13b, Reit14, Reit16, Schl14b]. A numerical framework to characterise the deformation process and effective forces is derived at the Chair of Applied Dynamics (LTD). The simulation of dielectric elastomer actuated multibody systems allows exploring the complex behaviour of humanoid robots that are equipped with artificial muscles instead of electrical drives. Due to their elasticity, artificial muscles can store energy and allow for dynamic and natural humanoid motion, contributing to the field of soft robotics [Triv08].

In order to control kinematic systems that are driven by dielectric elastomers, information about the time dependent behaviour of the actuators is required. Moreover, elaborate manufacturing methods result in complex inner structures of the elastomers [Reit14]. Hence, three dimensional simulations with a fine resolution are necessary to cover all non-linear effects and to understand and

[1] http://www.festo.com/group/de/cms/10274.htm
[2] http://www.bionicum.de/forschung/projekte/muskeln/

control the functional principle of artificial muscles. At the same time, the derived model needs to be as simple as possible, since complex finite element simulations tend to be computationally very costly.

1.1 Artificial muscle simulation literature review

A very general description of the behaviour of dielectric elastomers is obtained by considering the interaction between the force distribution that arises from an applied electric field and the mechanical deformation of the elastomer. While the deformation is characterised by the mechanical momentum balance and constitutive laws, the electric field distribution has to satisfy the Maxwell equations. Early theoretical considerations regarding different electromechanically coupled field theories are found in works from Eringen, Maugin and Toupin [Erin63, Erin89, Maug88, Toup56, Toup62]. In an extensive publication from Pao [Pao78], different approaches are compared to each other. Pao states that due to the complexity of the interaction of electromagnetic fields with matter and because electromagnetic fields inside materials can not be measured directly, many coexisting theories have evolved over time.

In a series of more recent publications, Dorfmann and Ogden contribute to the understanding of magnetoelastic and electroelastic coupling effects in elastic solids [Dorf03, Dorf05, Dorf06, Dorf10]. Their work is based on energy potentials that define constitutive laws and from which coupling forces can be derived by taking derivatives with respect to independent field variables (e.g. the deformation gradient and the electric field). Also Suo has been working on the theoretical background of dielectric elastomers, focusing on the virtual work of single material particles within the elastomer, from which electrostatic coupling is derived [Suo08, Suo10].

Because the electroelastic coupling equations are rather complex and can be solved analytically for special cases only (see e.g. [Dorf06]), numerical treatment is required. By identifying work-conjugate quantities in electromechanically coupled problems, McMeeking et. al. work towards a finite element implementation in [McMe05, McMe07]. Vu presents a finite element framework to numerically solve electromechanically coupled problems for arbitrary geometries and finite deformation in the static case [Vu07a, Vu07b]. Vu further investigates the influence of the free space surrounding electro-sensitive bodies via coupled finite element / boundary element simulations [Vu10, Vu12a, Vu12b]. Ask introduces viscoelastic terms that account for the damped dynamic behaviour of silicone based or acrylic dielectric elastomers and fits model parameters to

experimental measurements [Ask10, Ask12a, Ask12b, Ask15]. Applications of Ask's finite element implementation cover inverse-motion-based form finding problems of electromechanically coupled problems [Ask13]. The incompressibility of dielectric elastomers and associated numerical difficulties are discussed in [Ask13, Klas13, Klas16]. In [Klas11, Klas16, Müll10, Müll12], the effect of barium titanate inclusions with a high permittivity on the behaviour of dielectric elastomers is investigated. Dielectric elastomers are often utilised in form of a thin membrane and in [Klin13], a solid shell finite element formulation is presented. In [Gei14], stability issues of dielectric elastomers are explored.

The finite element approaches mentioned in the previous paragraph provide a very powerful and physically motivated toolset to solve electromechanically coupled problems. The implementation of the algorithms is, however, quite difficult and the simulations are computationally very costly. To find solutions for complex control problems where a multibody system is actuated by several artificial muscles at the same time as in [Schl16b], it is necessary to make use of lumped parameter models that reduce the computational cost. These reduced models are also often preferred by research groups with experimental background, because lumped parameter models allow for easier comparison with measurement data. Instead of considering field variables in geometries of arbitrary shape, the reduced models work with spatially discrete quantities, prescribed geometries and symmetric deformation.

In electronics, electrostriction generally describes the deformation of a dielectric material caused by an electric field, due to the interaction between charges [Sund92]. Considering the sandwich structure of a dielectric elastomer actuator, charges can be found on the electrodes (free charges) and in form of polarisation within the elastomer (bound charges). In 1998, using a simplified one-dimensional model, Pelrine et. al. show that for incompressible elastomers, the resulting electrostatic pressure is twice the pressure present in a rigid plate capacitor [Pelr98]. It is stated that the additional forces arise because like charges on the electrodes repel each other, facilitating the expansion of the electrode cross section area. However, when applying the principle of virtual work, Pelrine implicitly assumes that all forces act perpendicular to the capacitor plates, leading to a one-dimensional model. Due to its simplicity, the derived scalar formula

$$p = \varepsilon_0 \varepsilon_r e^2 \tag{1.1}$$

for the effective pressure p, vacuum and relative permittivity ε_0 and ε_r and the electric field e is very popular. The formula is applied to describe the behaviour of pre-stretched dielectric elastomer membranes in [Goul05, Kofo03, Kofo05, Wiss05, Wiss07a]. Its application to bending membranes is considered in [Kofo07, Loch07]. A multilayer bending actuator equipped

with so called chucking electrodes allows for variable stiffness as shown in [Imam17]. The behaviour of balloon and tubular shaped actuators is discussed in [Lu12, Mock06, Rudy12, Sole10]. Large scale dielectric elastomers and the behaviour at large deformation is modelled in [Huan12, Jord10b, Zhao08, Zhao10]. In [Kova09], Pelrine's formula is used to describe the behaviour of stacked actuators and in [Plan06], failure modes of dielectric elastomers are investigated. Other works cover dynamic analysis [Xu12] and close loop control [Kaal11] of artificial muscles, electrode free operation [Kepl10] and compression bandages [Pour14]. More recent works consider the high frequency operation of spring loaded circular dielectric elastomer membranes [Rizz15] that can also be utilised as micropumps [Chee16, Ghaz17].

Motivated by inconsistent experiments and finite element analyses, in 2007, Wissler et. al. propose a new physical interpretation of Pelrine's equation (1.1), distinguishing "in-plane" and "out-of-plane" stresses [Wiss07b]. Wissler compares measurement data to two-dimensional decoupled finite element simulations. They first evaluate the electric field distribution of a dielectric actuator in the cross section. Then, they calculate the two-dimensional mechanical pressure distribution resulting from the electric field. They find that Equation (1.1) is correct in terms of absolute values. However, the force also has components in radial ("in-plane") direction. This reveals that lumped parameter models and finite element simulations are not consistent to each other because they are based on different assumptions and modelling procedures.

1.2 Structure preserving integration and optimal control

The numerical approximation of the solution of equations of motion inevitably requires time stepping schemes that introduce a temporal discretisation. Depending on the discretisation technique, the choice of associated parameters and the time step size, the accuracy of the numerical solution is controlled, whilst taking the computational cost into account. Early works discuss the need of energy and linear momentum conservation when treating mechanical systems numerically and present appropriate time integration techniques for moving particles [LaBu75, LaBu76]. Also for finite element problems, energy conserving time integration schemes are developed [Hugh78, Bets00]. Of particular interest are symplectic integration schemes that are based on discrete variational principles and hence naturally integrate into the theory of Lagrangian mechanics [Hair06, Mars01]. These variational integrators provide a very good energy behaviour, accuracy and convergence properties [Lew03, Lew04] and are particularly suited for the treatment of constrained

mechanical systems [Leye08b].

The direct transcription method DMOC (discrete mechanics and optimal control) exploits the structure preserving characteristics of the variational integrator when solving optimal control problems. The idea of using the discrete equations of motions obtained from the variational integration scheme as constraints in an optimisation problem is first mentioned in [Jung05] and further refined in [OB11]. In [Leye09] DMOC is extended to allow for holonomic constraints, yielding DMOCC (discrete mechanics and optimal control for constrained systems).

1.3 Outline of this work

The aim of this work is to present a general, modular and consistent simulation framework to solve forward dynamics problems, obtain optimal control trajectories for dielectric elastomer actuated systems and close the gap between flexible and complex finite element simulations on the one hand and computationally cheap lumped parameter models on the other hand. Therefore, at first the complete set of physical relationships describing electromechanical coupling effects in a three dimensional space are formulated and discretised to be solved numerically. Based on this accurate model for dielectric elastomers, consistent reduced models are derived to save computational cost when solving optimal control problems.

For numerical treatment, the complex electromechanical coupling equations need to be discretised both in space as well as in time. In this work, at first the spatial discretisation is carried out using finite elements and then the temporal discretisation is introduced using a variational integrator. Chapter 2 gives a brief introduction to continuum mechanics including kinematic assumptions that are used throughout this work and presents the finite element method. The finite element discretisation allows to transform the set of partial differential field equations into a set of ordinary differential equations. The general structure of variational integration schemes for the temporal discretisation of ordinary differential equations is introduced in Chapter 3.

In Chapter 4, the previously described discretisation methods are applied to the electromechanically coupled problem in detail. Building on the static finite element formulation introduced by Vu [Vu07b], in this work inertia terms are added in order to include time effects. It is assumed that electrodynamical effects take place on a considerably smaller time scale than elastodynamical

effects. In order to simplify the model and to reduce the computational cost, magnetic interactions are not considered. A variational setting of the coupling equations is derived for which the hyperelastic material model from Vu [Vu07b] is extended by viscoelastic terms that account for damping. After discretisation, a structure preserving time integration scheme is derived to simulate the time dependent behaviour of stacked dielectric elastomer actuators. These actuators are used as artificial muscles to actuate a multibody system. The set-up of the multibody system as well as the coupling between the actuators and the system is introduced in Chapter 5.

As a part of this work, the extensive C++ library MulDi that supports the set-up, simulation and optimisation of multibody systems has been created. The basic structure of the library as well as some important algorithms regarding the generalised application of the null space method are presented in Chapter 6. Based on the finite element model of the artificial muscles, a consistent reduced model is derived in Chapter 7 and implemented into MulDi in order to save computational cost in optimal control simulations. In Chapter 8, the direct transcription method DMOCC [Leye09] is applied to obtain optimal control trajectories for artificial muscle actuated multibody systems. Finally, in Chapter 9, all findings and outcomes of this work are summarised and reviewed.

2 Continuum mechanics and the finite element method

This chapter introduces the basic assumptions of continuum mechanics, where the behaviour of materials is modelled via a continuous mass distribution rather than spatially discrete particles. The basic equations of finite deformation are presented and relevant mechanical quantities are introduced. Throughout this work, physical vectors and tensors are denoted in boldface, whereas 1-dimensional arrays are denoted by $\underline{(\bullet)}$ and matrices by $\underline{\underline{(\bullet)}}$. Material operations $\nabla_{\boldsymbol{X}} \cdot (\bullet)$ and $\nabla_{\boldsymbol{X}} \times (\bullet)$ differ from the spatial divergence $\nabla_{\boldsymbol{x}} \cdot (\bullet)$ and the spatial curl $\nabla_{\boldsymbol{x}} \times (\bullet)$. Material time derivatives are denoted with a dot $\dot{(\bullet)}$

First, kinematic assumptions are defined and the mechanical balance equations are presented (Sections 2.1 and 2.2). Then, hyper-viscoelastic material behaviour is introduced (Sections 2.3 and 2.4). Finally, the finite element approximation is briefly discussed (Section 2.5).

2.1 Kinematics

The reference configuration of the stress free dielectric elastomer at time $t = 0$ in three-dimensional space is denoted by $\mathcal{B}_0$. The reference position vector $\boldsymbol{X} \in \mathbb{R}^3$ depicts a material point of the body in reference configuration. The configuration of the body at a certain time t is denoted by $\mathcal{B}_t$, with the spatial position vector $\boldsymbol{x} = \boldsymbol{\chi}(\boldsymbol{X}, t) \in \mathbb{R}^3$ that points to the actual position of a material point $\boldsymbol{X}$, where $\boldsymbol{\chi}$ is the deformation map. The displacement vector

$$\boldsymbol{u}(\boldsymbol{X}, t) = \boldsymbol{\chi}(\boldsymbol{X}, t) - \boldsymbol{X} \quad \in \mathbb{R}^3 \tag{2.1}$$

describes the displacement of a material point and is often used as a configuration vector in the solution of continuum mechanics problems because it conveniently initialises to zero for $t = 0$.

By the introduction of the deformation gradient

$$\boldsymbol{F}(\boldsymbol{X}, t) = \frac{\partial \boldsymbol{\chi}(\boldsymbol{X}, t)}{\partial \boldsymbol{X}} \quad \in \mathbb{R}^{3\times 3} \tag{2.2}$$

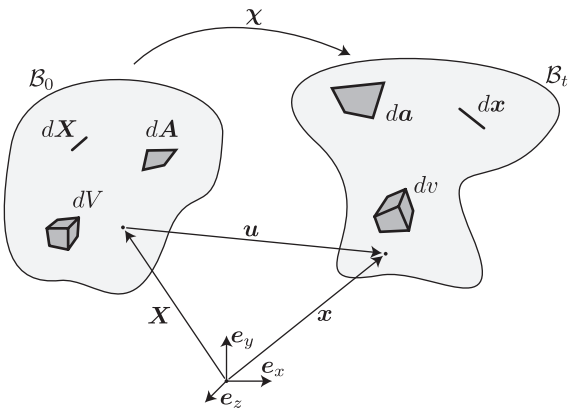

Figure 2.1: Finite deformation mapping from material to spatial configuration.

and using Nanson's formula, spatial line elements $d\boldsymbol{x}$, spatial area elements $d\boldsymbol{a} = \boldsymbol{n}da$ and spatial volume elements dv are related to their material counterparts $d\boldsymbol{X}, d\boldsymbol{A} = \boldsymbol{N}dA$ and dV by

$$d\boldsymbol{x} = \boldsymbol{F} \cdot d\boldsymbol{X} \tag{2.3}$$

$$d\boldsymbol{a} = J\boldsymbol{F}^{-T} \cdot d\boldsymbol{A} \tag{2.4}$$

$$dv = JdV \tag{2.5}$$

as illustrated in Figure 2.1, with the determinant of the deformation gradient $J = \det \boldsymbol{F}$ and the spatial and material surface normals $\boldsymbol{n} \in \mathbb{R}^3$ and $\boldsymbol{N} \in \mathbb{R}^3$, respectively. Based on the displacement vector $\boldsymbol{u}$, the deformation gradient $\boldsymbol{F}$ can also be computed as

$$\boldsymbol{F}(\boldsymbol{X}, t) = \frac{\partial \boldsymbol{u}(\boldsymbol{X}, t)}{\partial \boldsymbol{X}} + \boldsymbol{1}, \tag{2.6}$$

where $\boldsymbol{1} \in \mathbb{R}^{3\times3}$ is the 3×3 identity matrix. For symmetry reasons, the right Cauchy-Green tensor

$$\boldsymbol{C} = \boldsymbol{F}^T \cdot \boldsymbol{F} \tag{2.7}$$

is used when considering isotropic materials.

When dealing with incompressible or nearly incompressible materials, it is important to distinguish between volumetric and isochoric deformation parts. A multiplicative split of the deformation gradient

$$\boldsymbol{F} = \boldsymbol{F}^\circ \cdot \boldsymbol{F}^\diamond \tag{2.8}$$

introduces the volumetric component of the deformation gradient $\boldsymbol{F}^{\circ}$ and the isochoric component (sometimes referred to as distortional component) of the deformation gradient $\boldsymbol{F}^{\diamond}$. With the definition

$$\boldsymbol{F}^{\circ} = J^{1/3}\mathbf{1}, \tag{2.9}$$

assigning only volumetric changes to $\boldsymbol{F}^{\circ}$, it follows that the isochoric part

$$\boldsymbol{F}^{\diamond} = J^{-1/3}\boldsymbol{F} \tag{2.10}$$

contains only volume preserving components (e.g. shear deformation) and $\det(\boldsymbol{F}^{\diamond}) = 1$. Furthermore, the isochoric right Cauchy-Green tensor becomes

$$\boldsymbol{C}^{\diamond} = \boldsymbol{F}^{\diamond T} \cdot \boldsymbol{F}^{\diamond} = J^{-2/3}\boldsymbol{C}. \tag{2.11}$$

2.2 Balance equations

The general balance equation postulates that the temporal change of the volume integral of a field equals the sum of production and influx in the domain plus the flux of the field over the boundary of the body. With Reynolds' transport theorem and Gauss's divergence theorem, this integral relation can be transformed into a local form, which is applied to mechanical fields such as the mass density and the momentum density to derive the fundamental equations for a continuum [Mars94].

The conservation of mass, evaluated in the spatial as well as in the material configuration, yields the relationship

$$\rho_0 = J\rho, \tag{2.12}$$

where ρ_0 is the material mass density and ρ is the current spatial mass density. Furthermore, from the general balance equation it follows that for incompressible materials where $J \equiv 1$, the velocity field is divergence free, i.e.

$$\nabla_{\boldsymbol{X}} \cdot \dot{\boldsymbol{x}} = 0. \tag{2.13}$$

To derive the momentum balance, first a stress measure for a three-dimensional continuum needs to be defined. All material modelling in this work is based on hyperelastic approaches where the material's properties are derived from potential energy functions (see Section 2.4) and the energy functions are conveniently defined in the material domain. Therefore, the first Piola-Kirchhoff

stress tensor $\boldsymbol{P}^{\text{mech}} \in \mathbb{R}^{3\times3}$ that relates the surface stress $\bar{\boldsymbol{T}} \in \mathbb{R}^3$ to the material normal vector $\boldsymbol{N}$ such that

$$\bar{\boldsymbol{T}} = \boldsymbol{P}^{\text{mech}} \cdot \boldsymbol{N} \tag{2.14}$$

is introduced. The first Piola-Kirchhoff stress is related to its wide-spread spatial counterpart Cauchy stress $\boldsymbol{\sigma}$ via

$$\boldsymbol{P}^{\text{mech}} = J\boldsymbol{\sigma} \cdot \boldsymbol{F}^{-T}. \tag{2.15}$$

The evaluation of the general balance equation with the momentum density in the material domain then leads to the momentum equilibrium in material form

$$\nabla_{\boldsymbol{X}} \cdot \boldsymbol{P}^{\text{mech}} + \boldsymbol{b}_0 = \rho_0 \ddot{\boldsymbol{x}}, \tag{2.16}$$

which states that the divergence of the Piola-Kirchhoff stress $\boldsymbol{P}^{\text{mech}}$ plus the material volume force density $\boldsymbol{b}_0$ equals the inertia term on the right hand side including the material density ρ_0 and the material acceleration of a point $\ddot{\boldsymbol{x}}$ [Holz00].

From the angular momentum balance, it follows that the spatial Cauchy stress tensor is symmetric, i.e.

$$\boldsymbol{\sigma} = \boldsymbol{\sigma}^T. \tag{2.17}$$

However, due to the asymmetric transformation in Equation (2.15), this property does not apply to the first Piola-Kirchhoff stress $\boldsymbol{P}^{\text{mech}}$.

2.3 Viscoelastic material approach

In the past, very often acrylic materials were used to build dielectric elastomer actuators. However, the material of choice nowadays is silicone [Kofo05, Mich10, Reit14, Rizz15]. While acrylic materials such as the VHB tape from 3M are easy to obtain and handle, they also have some serious drawbacks like a bad reproducibility due to viscoplastic effects and a stretch dependent permittivity [Kofo03, Kofo08, Li11, Töl13, Wiss07b]. In contrast, silicones provide a stretch independent permittivity and only small dissipation [Mich10, Pelr02, Löwe05].

In this work, the viscoelastic material behaviour of silicones is covered by a Kelvin-Voigt like material approach, where a purely viscous damping part and a purely elastic part (both three-dimensional continuum models) are connected in parallel, resulting in an additive split of the material stress tensor such that

$$\boldsymbol{P}^{\text{mech}} = \boldsymbol{P}^{\text{ela}} + \boldsymbol{P}^{\text{vis}}, \tag{2.18}$$

where $\boldsymbol{P}^{\mathrm{ela}}(\boldsymbol{F})$ is the conservative elastic stress and $\boldsymbol{P}^{\mathrm{vis}}(\boldsymbol{F}, \dot{\boldsymbol{F}})$ the time dependent viscous part [Wrig08].

2.4 Constitutive laws

In this work, the material properties that relate the deformation gradient $\boldsymbol{F}$ with the stress tensor $\boldsymbol{P}^{\mathrm{ela}}$ are defined via a hyperelastic material approach. This approach is based on a potential energy density function Φ, from which the stress is obtained via derivation with respect to the deformation gradient. Hence, the elastic part of the total Piola-Kirchhoff stress (see Equation (2.18)) is obtained via

$$\boldsymbol{P}^{\mathrm{ela}} = \frac{\partial \Phi}{\partial \boldsymbol{F}}. \tag{2.19}$$

A well known hyperelastic material approach for isotropic compressible solids undergoing large deformation is the Neo-Hookean model. This model exists in various similar forms, e.g.

$$\Phi^{\mathrm{BW}}(\boldsymbol{F}) = \frac{\mu}{2}[\boldsymbol{C} : \mathbf{1} - 3] - \mu \ln(J) + \frac{\lambda}{2}[\ln(J)]^2 \tag{2.20}$$

from Bonet and Wood as presented in [Bone08], where μ and λ are the Lamé parameters. The material properties can be characterised by a pair of two independent material parameters of various choice. To illustrate that point, the relationship between the Lamé parameters and the pair (Y, ν), where Y is the Young's modulus and ν is Poisson's ratio is given by

$$\mu = \frac{Y}{2(1+\nu)} \tag{2.21}$$

$$\lambda = \frac{Y\nu}{(1+\nu)(1-2\nu)}. \tag{2.22}$$

Another widely used quantity is the bulk modulus κ that can be computed from the Lamé parameters via

$$\kappa = \lambda + \frac{2}{3}\mu. \tag{2.23}$$

Even though Neo-Hookean materials are not capable of representing very large strains of rubber like materials, they give quite good results for contractions to lengths being 70 to 80 % of the original specimen length [Kali97]. These strains are not expected to be exceeded within the application of DEAs as artificial muscles [Kova09] and hence stability issues for large strains that are known from literature [Xu10] are not an issue here.

Throughout this work, for the viscoelastic stress $\boldsymbol{P}^{\mathrm{vis}}$, an approach from [Wrig08] is used, where the Kelvin-Voigt model is extended for three dimensions and finite strains, resulting in a viscous second Piola-Kirchhoff stress tensor $\boldsymbol{S}^{\mathrm{vis}}$. This tensor is transformed to the material configuration by the operation $\boldsymbol{P}^{\mathrm{vis}} = \boldsymbol{F} \cdot \boldsymbol{S}^{\mathrm{vis}}$, such that after some calculation the first Piola-Kirchhoff stress tensor for viscous behaviour is given as

$$\boldsymbol{P}^{\mathrm{vis}}(\boldsymbol{F}, \dot{\boldsymbol{F}}) = \frac{1}{2} J \eta \left(\boldsymbol{F}^{-T} \cdot \dot{\boldsymbol{F}}^{T} \cdot \boldsymbol{F}^{-T} + \dot{\boldsymbol{F}} \cdot \boldsymbol{C}^{-1} \right), \tag{2.24}$$

with the damping parameter η.

The momentum balance (2.16) applied within the solid $\mathcal{B}_0$ together with the boundary conditions (2.14) on the solid surface $\partial\mathcal{B}_0$, as well as the constitutive relationship (2.19) and initial conditions $\bar{\boldsymbol{x}}_0, \bar{\dot{\boldsymbol{x}}}_0$ that prescribe the state at time $t = 0$ form a complete system to describe the temporal evolution of mechanical problems. However, in most cases, these equations can not be solved analytically but require numerical discretisation in space as well as in time. One approach to account for the spatial discretisation is the finite element method that will be introduced in the next section.

2.5 Finite element method

This section does not aim to introduce the whole concept of the finite element method including mathematical background and convergence proofs but should rather give an overview about the notation that is used in this work. Combining the finite element method with variational time integration requires a procedure that slightly deviates from the standard theory that is found in literature [Bone08, Fish07, Pari03, Wrig08].

The discretisation of the time-dependent partial differential equations

$$\nabla_{\boldsymbol{X}} \cdot \boldsymbol{P}^{\mathrm{mech}} + \boldsymbol{b}_0 = \rho_0 \ddot{\boldsymbol{x}} \qquad \text{in } \mathcal{B}_0 \tag{2.25a}$$

$$\boldsymbol{P}^{\mathrm{mech}} \cdot \boldsymbol{N} = \bar{\boldsymbol{T}} \qquad \text{in } \partial\mathcal{B}_0 \tag{2.25b}$$

$$\boldsymbol{x}(\boldsymbol{X}, 0) = \bar{\boldsymbol{x}}_0 \qquad \text{in } \mathcal{B}_0 \tag{2.25c}$$

$$\dot{\boldsymbol{x}}(\boldsymbol{X}, 0) = \bar{\dot{\boldsymbol{x}}}_0 \qquad \text{in } \mathcal{B}_0 \tag{2.25d}$$

can be accomplished in several ways. In this work, first the spatial discretisation using finite elements is performed to obtain a system of ordinary differential equations with a finite dimensional configuration. Then, a discrete variational principle yields the discrete Euler-Lagrange-Equations, which can be used to obtain a structure preserving time integration scheme (see Chapter 3).

For the spatial finite element discretisation, the so called strong or local form of the problem given by Equations (2.25) has to be transformed into an integral form (also known as weak form) that covers the whole space of interest. The integral form can be obtained by multiplying Equations (2.25a) and (2.25b) with a so-called test function and integrating over the volume. Another approach is to start with a Lagrangian description of the problem (based on the hyperelastic potential energy density) and then applying Hamilton's principle, where the variation can be interpreted as being the test function. The latter procedure is presented in detail in Section 4.2 for the electromechanically coupled problem of the dielectric elastomer actuator.

The integral form provides some advantages, e.g. natural boundary conditions (Neumann type) are enforced automatically. Moreover, via partial integration, the integral form allows to "move" derivative operations from solution quantities (e.g. $\boldsymbol{x}$) to test functions (e.g. $\delta\boldsymbol{x}$), like

$$\int_{t_0}^{t_N} \ddot{\boldsymbol{x}}\, \delta\boldsymbol{x}\; dt = -\int_{t_0}^{t_N} \dot{\boldsymbol{x}}\, \delta\dot{\boldsymbol{x}}\; dt. \tag{2.26}$$

Note that the variation $\delta\boldsymbol{x}$ vanishes at the time boundaries. As a consequence, lower continuity requirements apply to the solution variable in the discrete space (compare to [Torn14]).

The Lagrangian density is given by the difference of the kinetic $\mathcal{T}$ and potential energy density, i.e.

$$\mathcal{L}(\dot{\boldsymbol{x}}, \boldsymbol{F}) = \mathcal{T}(\dot{\boldsymbol{x}}) - \Phi(\boldsymbol{F}), \tag{2.27}$$

such that the Lagrangian L can be obtained by integrating over the Lagrangian density in space

$$L(\dot{\boldsymbol{x}}, \boldsymbol{F}) = \int_{\mathcal{B}_0} \mathcal{L}(\dot{\boldsymbol{x}}, \boldsymbol{F})\; dV. \tag{2.28}$$

The kinetic energy density is given by

$$\mathcal{T}(\dot{\boldsymbol{x}}) = \frac{1}{2}\rho_0 \dot{\boldsymbol{x}} \cdot \dot{\boldsymbol{x}}, \tag{2.29}$$

while the potential energy density Φ is given by the hyperelastic material approach as described in Section 2.4.

Introducing the spatial discretisation, first the volume integral over $\mathcal{B}_0$ of the integral form (2.28) is split into a finite number of elements $\mathcal{B}_0^{\mathrm{el}}$ such that

$$\int_{\mathcal{B}_0} \mathcal{L}(\dot{\boldsymbol{x}}, \boldsymbol{F})\; dV = \biguplus_{\mathrm{el}} \int_{\mathcal{B}_0^{\mathrm{el}}} \mathcal{L}(\dot{\boldsymbol{x}}, \boldsymbol{F})\; dV, \tag{2.30}$$

where the finite element assembly operator $\biguplus_{\text{el}}$ composes the global quantities from local element contributions. For scalar-valued functions as the Lagrangian density, the assembly operator may be replaced by the sum over all elements $\sum_{\text{el}}$. However, for vector-valued quantities, the assembly operator guarantees the assignment of local element based degrees of freedom to global vector entries.

Within a finite element, solution variables are approximated via a Galerkin ansatz that substitutes the original quantities by a linear combination of base functions such that

$$\boldsymbol{x}(\boldsymbol{X}, t) \approx \underline{q}^{\text{el}}(t) \odot \underline{\boldsymbol{N}}_{\text{el}}^{\text{trans}}(\boldsymbol{X}), \tag{2.31}$$

using finite element shape functions $\underline{\boldsymbol{N}}_{\text{el}}^{\text{trans}}$. The configuration $\underline{q}^{\text{el}} \in \mathbb{R}^{n_{\text{dof,el}}}$ contains the values of all degrees of freedom of the element with $n_{\text{dof,el}}$ being the total number of degrees of freedom of the element. If linear Lagrange shape functions are used for all space dimensions, $\underline{q}^{\text{el}}$ contains translations for each vertex of the element. Note that $\underline{\boldsymbol{N}}_{\text{el}}^{\text{trans}} \in \mathbb{R}^{n_{\text{dof,el}} \times n_{\text{dim}}}$ with $n_{\text{dim}} = 3$ being the physical space dimension. The operator $\odot$ denotes the single contraction over all degrees of freedom n_{dof}, respectively, $n_{\text{dof,el}}$. As a result of this discretisation, the discrete configuration $\underline{q}^{\text{el}}$ is only dependent on time t, whereas the shape functions $\underline{\boldsymbol{N}}_{\text{el}}^{\text{trans}}$ only depend on $\boldsymbol{X}$. Hence, the deformation gradient is approximated by

$$\boldsymbol{F}(\boldsymbol{X}, t) \approx \underline{q}^{\text{el}}(t) \odot \frac{\partial \underline{\boldsymbol{N}}_{\text{el}}^{\text{trans}}(\boldsymbol{X})}{\partial \boldsymbol{X}}, \tag{2.32}$$

where $\partial \underline{\boldsymbol{N}}_{\text{el}}^{\text{trans}}(\boldsymbol{X}) / \partial \boldsymbol{X} \in \mathbb{R}^{n_{\text{dof}} \times n_{\text{dim}} \times n_{\text{dim}}}$ and the velocity $\dot{\boldsymbol{x}}$ is approximated by

$$\dot{\boldsymbol{x}}(\boldsymbol{X}, t) \approx \dot{\underline{q}}^{\text{el}}(t) \odot \underline{\boldsymbol{N}}_{\text{el}}^{\text{trans}}(\boldsymbol{X}). \tag{2.33}$$

After introducing the approximations (2.32) and (2.33) into the right hand side of Equation (2.30), the integral can be numerically approximated using a Gauss quadrature on a reference cell $\square$ with the reference cell position vector $\boldsymbol{\xi}$ for a function f such that

$$\begin{aligned} \int_{\mathcal{B}_0^{\text{el}}} f(\boldsymbol{X})\, dV &= \int_{\square} f(\boldsymbol{X}(\boldsymbol{\xi})) \left| \frac{\partial \boldsymbol{X}}{\partial \boldsymbol{\xi}} \right| d\square \\ &\approx \sum_{n_{\text{Gauss}}} w_{n_{\text{Gauss}}} f(\boldsymbol{X}(\boldsymbol{\xi}_{n_{\text{Gauss}}})) \left| \frac{\partial \boldsymbol{X}}{\partial \boldsymbol{\xi}} \right|, \end{aligned} \tag{2.34}$$

where n_{Gauss} is the number of Gauss integration points and $w_{n_{\text{Gauss}}}$ are the Gauss weights [Wrig08].

3 Lagrangian mechanics and variational integration

All dynamic modelling in this work is based on Lagrangian mechanics. As opposed to classical mechanics being based on Newton's laws and vector valued forces, the energy related Lagrangian covers all dynamics of the system in a scalar function. One of the reasons for this choice here is the intention to use structure preserving time integration. Noether's theorem states that there is a one to one inter-relation between an invariance of the Lagrangian and a conserved quantity in the solution of the equations of motion. In general, this coherence is infringed for arbitrary time discretisation methods. However, the theorem holds true for the structure preserving integration scheme that is derived from the Lagrangian directly [Leye08b, Leye09, Maas11]. Moreover, the variational integrator shows a very good long time energy behaviour [Mars01]. There is neither numerical damping nor an artificial energy gain present and the total energy error is bounded for long simulation times. The energy band is very small and decreases if the time step size is reduced.

First, in Section 3.1 the continuous as well as the discrete Euler-Lagrange-Equations in its basic form are derived side-by-side to highlight similarities. These basic equations are extended to the case of redundant configuration variables in Sections 3.2 and 3.3, with non-conservative contributions in Section 3.4 and with control variables in Section 3.5. Section 3.3 shows how the introduction of Lagrange multipliers can be avoided when redundant configuration variables are used. Finally, in Section 3.6 the discrete Legendre transform is introduced to formulate initial conditions and allow for energy evaluation.

3.1 Derivation of the discrete Euler-Lagrange-Equations

In this section, the discrete Euler-Lagrange-Equations for conservative problems are derived in a direct comparison with the corresponding continuous counterpart. The Lagrangian

$$L(\underline{q}, \underline{\dot{q}}) = T(\underline{q}, \underline{\dot{q}}) - \Pi(\underline{q}) \tag{3.1}$$

is composed of the difference of the kinetic energy $T(\underline{q}, \underline{\dot{q}})$ and the potential energy $\Pi(\underline{q})$, where $\underline{q}(t) \in \mathbb{R}^{n_q}$ contains the spatially discrete n_q configuration

variables of the system and $\dot{\underline{q}}(t)$ their absolute time derivatives, respectively. The action S of the system is obtained by integrating the Lagrangian over the continuous time interval $[t_0, t_N]$, i.e.

$$S[\underline{q}] = \int_{t_0}^{t_N} L(\underline{q}, \dot{\underline{q}})\ dt, \tag{3.2}$$

where the action $S[\underline{q}]$ is a functional of $\underline{q}$. The action (3.2) is discretised on a time grid that consists of discrete equidistant time nodes t_n in the interval $[t_0, t_N]$ with $n = 0, 1, \ldots, N$ and constant time step size $\Delta t = t_{n+1} - t_n$ such that

$$S[\underline{q}] = \sum_{n=0}^{N-1} \int_{t_n}^{t_{n+1}} L(\underline{q}, \dot{\underline{q}})\ dt. \tag{3.3}$$

The time integral over the Lagrangian in a small time section $[t_n, t_{n+1}]$ is approximated on the discrete time grid via a generalised midpoint quadrature and finite differences, yielding the discrete Lagrangian

$$\begin{aligned} L_d(\underline{q}_n, \underline{q}_{n+1}) &= \Delta t\ L\left(\alpha\ \underline{q}_n + (1-\alpha)\ \underline{q}_{n+1}, \frac{\underline{q}_{n+1} - \underline{q}_n}{\Delta t}\right) \\ &\approx \int_{t_n}^{t_{n+1}} L(\underline{q}, \dot{\underline{q}})\ dt \end{aligned} \tag{3.4}$$

with $\alpha \in [0, 1]$ and $\underline{q}_n$ being the time discrete configuration approximating $\underline{q}(t_n)$. The discrete counterpart to the continuous action (3.2) is then given by

$$S_d(\underline{q}_0, \underline{q}_1, \ldots, \underline{q}_N) = \sum_{n=0}^{N-1} L_d(\underline{q}_n, \underline{q}_{n+1}), \tag{3.5}$$

where the discrete action $S_d(\underline{q}_0, \underline{q}_1, \ldots, \underline{q}_N)$ is a function of the discrete configurations $\underline{q}_n$ with $n = 0, \ldots, N$.

If $\underline{q}$ is given in minimal coordinates and no further constraints apply to the configuration, then Hamilton's principle states that the true evolution of a system is a stationary point of the action. This principle can be applied to the continuous, as well as to the discrete version of the action, requiring

$$\delta S = 0 \qquad\qquad \delta S_d = 0 \tag{3.6}$$

$$\int_{t_0}^{t_N} \delta L(\underline{q}, \dot{\underline{q}})\ dt = 0 \qquad\qquad \sum_{n=0}^{N-1} \delta L_d(\underline{q}_n, \underline{q}_{n+1}) = 0. \tag{3.7}$$

The variation of the continuous and discrete version of the Lagrangian reads

$$\delta L = \frac{\partial L}{\partial \underline{q}} \delta \underline{q} + \frac{\partial L}{\partial \dot{\underline{q}}} \delta \dot{\underline{q}} \qquad \delta L_d = \frac{\partial \delta L_d}{\partial \underline{q}_n} \delta \underline{q}_n + \frac{\partial \delta L_d}{\partial \underline{q}_{n+1}} \delta \underline{q}_{n+1}, \tag{3.8}$$

respectively. Inserting (3.8) into Equation (3.7) and applying partial integration to the continuous case (left hand side) allows to eliminate the variation $\delta\underline{\dot{q}}$ and factor out $\delta\underline{q}$. In the discrete case (right hand side) sum indices can be shifted to eliminate $\delta\underline{q}_{n+1}$ and factor out the variation $\delta\underline{q}_n$. In both cases, it must be considered that the variation of the configuration equals zero at the time boundaries, i.e. $\delta\underline{q}_0 = \delta\underline{q}_N = 0$, such that the variation of the action (3.7) can be written as

$$\delta S = \int_{t_0}^{t_N} \left[\frac{\partial L}{\partial \underline{q}} - \frac{d}{dt}\left(\frac{\partial L}{\partial \underline{\dot{q}}} \right) \right] \delta\underline{q} \; dt = 0 \tag{3.9}$$

in the continuous case and

$$\delta S_d = \sum_{n=1}^{N-1} \left[\frac{\partial L_d(\underline{q}_n, \underline{q}_{n+1})}{\partial \underline{q}_n} + \frac{\partial L_d(\underline{q}_{n-1}, \underline{q}_n)}{\partial \underline{q}_n} \right] \delta\underline{q}_n = 0 \tag{3.10}$$

in the discrete case. The fundamental lemma of the calculus of variations requires the brackets $[\bullet]$ in Equations (3.9) and (3.10) to equal zero for arbitrary variations. This last step leads to the well known Euler-Lagrange-Equations in the continuous case

$$\frac{\partial L(\underline{q}, \underline{\dot{q}})}{\partial \underline{q}} - \frac{d}{dt}\left(\frac{\partial L(\underline{q}, \underline{\dot{q}})}{\partial \underline{\dot{q}}} \right) = \underline{0} \quad \in \mathbb{R}^{n_q} \tag{3.11}$$

and their discrete counterpart

$$\frac{\partial L_d(\underline{q}_n, \underline{q}_{n+1})}{\partial \underline{q}_n} + \frac{\partial L_d(\underline{q}_{n-1}, \underline{q}_n)}{\partial \underline{q}_n} = \underline{0} \quad \in \mathbb{R}^{n_q}. \tag{3.12}$$

The non-linear set of equations (3.12) is a function of three consecutive configurations $\underline{q}_{n-1}, \underline{q}_n$ and $\underline{q}_{n+1}$, providing a time integration scheme for the system defined by the action S. In a forward dynamics simulation, where two preceding configurations $\underline{q}_{n-1}$ and $\underline{q}_n$ are given, the unknown configuration $\underline{q}_{n+1}$ can be determined via a Newton-Raphson scheme.

Instead of deriving the continuous equations of motion by evaluating (3.11) and discretising with a common time stepping scheme (e.g. Euler explicit/implicit, Runge-Kutta), the variational integration scheme obtained by evaluating the Euler-Lagrange-Equation (3.12) can be used directly to solve for the system's dynamics. That way, there is a discrete Noether theorem for the discrete system and the structure of the system including its symplecticity is preserved.

3.2 Redundant configuration variables

For redundant configuration variables, i.e. n_q is larger than the number of degrees of freedom n_{dof} of the system, $n_c = n_q - n_{\text{dof}}$ additional constraints $\underline{g}(\underline{q}) = \underline{0} \in \mathbb{R}^{n_c}$ apply to the configuration $\underline{q}$. Corresponding constraint forces then account for the physical conditions that decrease the number of degrees of freedom of the system.

To include the constraints, the integrand of the action integral (3.2) is extended with Lagrange multipliers $\underline{\lambda} \in \mathbb{R}^{n_c}$, such that

$$S[\underline{q}, \underline{\lambda}] = \int_{t_0}^{t_N} \left(L(\underline{q}, \dot{\underline{q}}) - \underline{g}(\underline{q}) \cdot \underline{\lambda} \right) dt, \tag{3.13}$$

where $\tilde{L}(\underline{q}, \dot{\underline{q}}, \underline{\lambda}) = L(\underline{q}, \dot{\underline{q}}) - \underline{g}(\underline{q}) \cdot \underline{\lambda}$ is also referred to as augmented Lagrangian. In the continuous case, Hamilton's principle then leads to the constrained Euler-Lagrange-Equations

$$\frac{\partial L(\underline{q}, \dot{\underline{q}})}{\partial \underline{q}} - \frac{d}{dt}\left(\frac{\partial L(\underline{q}, \dot{\underline{q}})}{\partial \dot{\underline{q}}} \right) - \underline{\underline{G}}^T(\underline{q}) \cdot \underline{\lambda} = \underline{0} \quad \in \mathbb{R}^{n_q} \tag{3.14a}$$

$$\underline{g}(\underline{q}) = \underline{0} \quad \in \mathbb{R}^{n_c}, \tag{3.14b}$$

where $\underline{\underline{G}}(\underline{q}) = {}^{\partial \underline{g}(\underline{q})}/_{\partial \underline{q}} \in \mathbb{R}^{n_c \times n_q}$ is the constraint Jacobian. The additional constraint equations (3.14b) arise from the variation of the action $S[\underline{q}, \underline{\lambda}]$ with respect to $\underline{\lambda}$. The expression $\underline{\underline{G}}^T(\underline{q}) \cdot \underline{\lambda}$ can physically be interpreted as constraint forces. The total of $n_q + n_c$ equations in (3.14) can be used to solve for the n_q redundant configuration variables in $\underline{q}$ and n_c Lagrange multipliers $\underline{\lambda}$.

In the discrete case, the additional Lagrange multiplier term in the action (3.13) is approximated analogously to the Lagrangian in (3.4). The only difference is that instead of a generalised midpoint quadrature, a generalised trapezoidal rule is used such that

$$\begin{aligned} \xi_g(\underline{q}_n, \underline{q}_{n+1}, \underline{\lambda}_n, \underline{\lambda}_{n+1}) &= \Delta t \left(\beta \ \underline{g}(\underline{q}_n) \cdot \underline{\lambda}_n + (1-\beta) \ \underline{g}(\underline{q}_{n+1}) \cdot \underline{\lambda}_{n+1} \right) \\ &\approx \int_{t_n}^{t_{n+1}} \underline{g}(\underline{q}) \cdot \underline{\lambda} \ dt, \end{aligned} \tag{3.15}$$

with $\beta \in [0, 1]$ and $\underline{\lambda}_n$ being the time discrete Lagrange multiplier at t_n, approximating $\underline{\lambda}(t_n)$. The reason for this choice of quadrature is that the constraints $\underline{g}$ shall be fulfilled exactly at the discrete time nodes (up to numerical accuracy) and not somewhere in between.

Evaluating the variation of the discrete action

$$\delta S_d = \sum_{n=0}^{N-1} \left(\delta L_d(\underline{q}_n, \underline{q}_{n+1}) - \delta \xi_g(\underline{q}_n, \underline{q}_{n+1} \right) = 0 \tag{3.16}$$

finally yields the constrained discrete Euler-Lagrange-Equations

$$\frac{\partial L_d(\underline{q}_n, \underline{q}_{n+1})}{\partial \underline{q}_n} + \frac{\partial L_d(\underline{q}_{n-1}, \underline{q}_n)}{\partial \underline{q}_n} - \underline{\underline{G}}_d^T(\underline{q}_n) \cdot \underline{\lambda}_n = \underline{0} \quad \in \mathbb{R}^{n_q} \tag{3.17a}$$

$$\underline{g}(\underline{q}_{n+1}) = \underline{0} \quad \in \mathbb{R}^{n_c}, \tag{3.17b}$$

where $\underline{\underline{G}}_d(\underline{q}_n) = \Delta t \; {}^{\partial \underline{g}(\underline{q}_n)}/_{\partial \underline{q}_n}$ is the discrete constraint Jacobian. Note that the parameter β introduced in (3.15) cancelled out and is not present any more in Equation (3.17). Also note that Equation (3.17b) is evaluated at t_{n+1}. Assuming that $\underline{q}_{n-1}$ and $\underline{q}_n$ are given, this allows to solve for the unknown configuration $\underline{q}_{n+1} \in \mathbb{R}^{n_q}$ at time t_{n+1} and unknown Lagrange multipliers $\underline{\lambda}_n \in \mathbb{R}^{n_c}$ at time t_n via the $n_q + n_c$ Equations (3.17).

3.3 Null space projection

It is well known that the introduction of Lagrange multipliers leads to ill-conditioned matrices when computing the dynamics of the system numerically. On the other hand, a more efficient formulation with minimal coordinates $\underline{q}^{\min}$ that avoids redundancies is less flexible, less modular and often accompanied by singularities that result from rotational degrees of freedom. In this work, a null space matrix (also known as tangential matrix) is used to project the discrete Euler-Lagrange-Equations (3.17a) into the tangent space, where constraint fulfilling motion on velocity level happens. Consequently, Lagrange multipliers need not be determined but can optionally be computed in post-processing.

The null space matrix $\underline{\underline{T}}(\underline{q})$ is obtained by finding a relationship between minimal velocities $\dot{\underline{q}}^{\min} \in \mathbb{R}^{n_{\text{dof}}}$ and redundant velocities $\dot{\underline{q}}$ such that

$$\dot{\underline{q}} = \underline{\underline{T}}(\underline{q}) \cdot \dot{\underline{q}}^{\min}, \tag{3.18}$$

where the null space matrix $\underline{\underline{T}}(\underline{q}) \in \mathbb{R}^{n_q \times n_{\text{dof}}}$ depends on the current configuration $\underline{q}$, see Figure 3.1. Right multiplying the null space matrix to the (discrete) constraint Jacobian returns zero, i.e.

$$\underline{\underline{G}}(\underline{q}) \cdot \underline{\underline{T}}(\underline{q}) = \underline{\underline{0}} \quad \in \mathbb{R}^{n_c \times n_{\text{dof}}}. \tag{3.19}$$

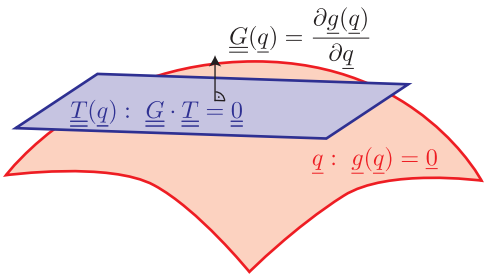

Figure 3.1: The null space matrix and the constraint manifold.

Left multiplying the transpose of the null space matrix $\underline{\underline{T}}^T$ to Equation (3.17a) leads to the null space projected discrete Euler-Lagrange-Equations

$$\underline{\underline{T}}^T(\underline{q}_n) \cdot \left(\frac{\partial L_d(\underline{q}_n, \underline{q}_{n+1})}{\partial \underline{q}_n} + \frac{\partial L_d(\underline{q}_{n-1}, \underline{q}_n)}{\partial \underline{q}_n} \right) = \underline{0} \quad \in \mathbb{R}^{n_{\text{dof}}} \tag{3.20a}$$

$$\underline{g}(\underline{q}_{n+1}) = \underline{0} \quad \in \mathbb{R}^{n_c}, \tag{3.20b}$$

where the dimension of Equation (3.20a) is reduced to the number of degrees of freedom n_{dof}.

If $\underline{q}_{n-1}$ and $\underline{q}_n$ are given, the $n_q = n_{\text{dof}} + n_c$ Equations (3.20) can be used to solve for n_q redundant configuration variables in $\underline{q}_{n+1}$. The Lagrange multipliers $\underline{\lambda}$ are not present any more. If information about constraint forces is needed, the Lagrange multipliers can be evaluated during post processing as described in [Leye08b]. Null space matrices for standard kinematic pairs are given in [Bets06, Maas12].

3.4 Non-conservative contributions

Equation (3.2) considers conservative contributions only. This means that all dynamics of the system can be derived from the kinetic energy T and an energy potential Π, while the total energy $H = T + \Pi$ is preserved. Non-conservative contributions like friction or external loads change the amount of energy stored in the system. They can be considered via the Lagrange-d'Alembert principle that reads

$$\int_{t_0}^{t_N} \delta L(\underline{q}, \dot{\underline{q}}) \ dt + \int_{t_0}^{t_N} \delta W^{\text{ext}}(t) \ dt = 0, \tag{3.21}$$

with the variation of the work of non-conservative contributions $\delta W^{\text{ext}}(t)$, also known as non-conservative virtual work. The virtual work

$$\delta W^{\text{ext}}(t) = \underline{f}^{\text{ext}}(t) \cdot \delta \underline{q} \tag{3.22}$$

contains non-conservative generalised forces $\underline{f}^{\text{ext}}(t)$ that are treated fixed during variation. When evaluating the Lagrange-d'Alembert principle in the continuous case

$$\frac{\partial L(\underline{q}, \dot{\underline{q}})}{\partial \underline{q}} - \frac{d}{dt}\left(\frac{\partial L(\underline{q}, \dot{\underline{q}})}{\partial \dot{\underline{q}}}\right) + \underline{f}^{\text{ext}}(t) = \underline{0}, \tag{3.23}$$

the generalised forces $\underline{f}^{\text{ext}}(t)$ appear as an additional term.

The discrete Lagrange-d'Alembert principle can be written as

$$\sum_{n=0}^{N-1} \left(\delta L_d(\underline{q}_n, \underline{q}_{n+1}) + \delta W_d^{\text{ext}}\right) = 0, \tag{3.24}$$

where the discrete non-conservative virtual work δW_d^{ext} approximates the continuous virtual work time integral via a midpoint quadrature such that

$$\begin{aligned} \delta W_d^{\text{ext}} &= \Delta t \, \frac{\underline{f}_n^{\text{ext}} + \underline{f}_{n+1}^{\text{ext}}}{2} \frac{\delta \underline{q}_n + \delta \underline{q}_{n+1}}{2} \\ &\approx \int_{t_n}^{t_{n+1}} \underline{f}^{\text{ext}}(t) \cdot \delta \underline{q} \, dt, \end{aligned} \tag{3.25}$$

and $\underline{f}_n^{\text{ext}}$ being the time discrete generalised external force at t_n, approximating $\underline{f}^{\text{ext}}(t_n)$. Evaluating the variation in the discrete setting analogous to the derivation in Section 3.1 (and including the shift of sum indices) leads to the discrete Euler-Lagrange-Equations for non-conservative systems

$$\frac{\partial L_d(\underline{q}_n, \underline{q}_{n+1})}{\partial \underline{q}_n} + \frac{\partial L_d(\underline{q}_{n-1}, \underline{q}_n)}{\partial \underline{q}_n} + \Delta t \, \frac{\underline{f}_{n-1}^{\text{ext}} + 2\underline{f}_n^{\text{ext}} + \underline{f}_{n+1}^{\text{ext}}}{4} = \underline{0} \in \mathbb{R}^{n_q}, \tag{3.26}$$

where the non-conservative contributions $\underline{f}^{\text{ext}}$ appear as a weighted time average in the discrete equations of motion.

The abbreviations

$$\underline{f}_n^{\text{ext}-} = \frac{\Delta t}{2} \, \frac{\underline{f}_n^{\text{ext}} + \underline{f}_{n+1}^{\text{ext}}}{2} \qquad \underline{f}_n^{\text{ext}+} = \frac{\Delta t}{2} \, \frac{\underline{f}_{n-1}^{\text{ext}} + \underline{f}_n^{\text{ext}}}{2} \tag{3.27}$$

are introduced for convenience (and consistency as seen later), where the sign $(+, -)$ alludes to the direction of the discretisation in time. This allows

for a new interpretation, where the discrete non-conservative contribution at time t_n is composed of a right hand side evaluation (in time) of the continuous generalised force, mapped backward (sign $-$), and a left hand side evaluation of the same force, mapped forward (sign $+$). Inserting abbreviations (3.27) into Equation (3.26) yields

$$\frac{\partial L_d(\underline{q}_n, \underline{q}_{n+1})}{\partial \underline{q}_n} + \frac{\partial L_d(\underline{q}_{n-1}, \underline{q}_n)}{\partial \underline{q}_n} + \underline{f}_n^{\text{ext}-} + \underline{f}_n^{\text{ext}+} = \underline{0} \quad \in \mathbb{R}^{n_q}. \tag{3.28}$$

Note that the null space projection introduced in Section 3.3 can be combined with the discrete Euler-Lagrange equations containing non-conservative contributions (3.28). The discrete generalised forces (3.27) are then projected into the tangent space via the null space matrix as well, implying a reduction of their dimension.

In some cases, the non-conservative generalised forces $\underline{f}^{\text{ext}}$ depend on the configuration $\underline{q}$ and its time derivative $\dot{\underline{q}}$ such that $\underline{f}^{\text{ext}}(\underline{q}, \dot{\underline{q}})$ (as with viscoelastic contributions, compare to Equation (2.24)). Then, the discrete generalised force counterparts $\underline{f}_n^{\text{ext}-}$ and $\underline{f}_n^{\text{ext}+}$ are given by

$$\underline{f}_n^{\text{ext}-} = \frac{\Delta t}{2}\, \underline{f}^{\text{ext}} \left(\frac{\underline{q}_n + \underline{q}_{n+1}}{2}, \frac{\underline{q}_{n+1} - \underline{q}_n}{\Delta t} \right) \tag{3.29}$$

$$\underline{f}_n^{\text{ext}+} = \frac{\Delta t}{2}\, \underline{f}^{\text{ext}} \left(\frac{\underline{q}_{n-1} + \underline{q}_n}{2}, \frac{\underline{q}_n - \underline{q}_{n-1}}{\Delta t} \right), \tag{3.30}$$

respectively.

While for conservative systems the total energy is preserved and the variational integration scheme guarantees that total energy oscillations are bounded, the total energy varies for non-conservative systems. Energy might be dissipated due to damping terms and additional energy might be introduced via external stimulation of the system. In these cases, the structure preserving integration scheme (3.28) guarantees that the difference in energy between the numerical solution and the continuous model is bounded, while the bound size decreases for smaller time step sizes. In other words, the variational integration scheme accurately represents the physically motivated change in energy due to non-conservative contributions and does neither introduce numerical damping nor an artificial energy gain.

3.5 Control variables

Even though control variables $\underline{u}$ might be considered as being part of the configuration $\underline{q}$ (when prescribing a generalised displacement) or being covered by non-conservative contributions (3.27) (when prescribing external generalised forces), they are usually handled separately during discretisation of the Lagrangian. The reason is that in practical control applications, control quantities are usually applied to the system at the beginning of the sampling time block and then kept constant for one time step until they are updated to a new value at the beginning of the next time step. In the sequel, control quantities require an appropriate quadrature rule when discretising the Lagrangian description of the system. In the present work, this applies to electrostatic degrees of freedom that are introduced in Chapter 4 and that are initially part of the configuration vector. When solving optimal control problems, however, electrostatic degrees of freedom are considered as control variables being determined by the optimisation algorithm and hence discretised accordingly.

Slightly abusing notation, the continuous Lagrangian $L(\underline{q}, \underline{u}, \dot{\underline{q}})$ can be written as a function of $\underline{q}, \dot{\underline{q}}$ and control $\underline{u}$. Then the discrete Lagrangian reads (compare to Equation (3.4))

$$\begin{aligned} L_d(\underline{q}_n, \underline{u}_n, \underline{q}_{n+1}) &= \Delta t \; L\left(\alpha \; \underline{q}_n + (1-\alpha) \; \underline{q}_{n+1}, \underline{u}_n, \frac{\underline{q}_{n+1} - \underline{q}_n}{\Delta t}\right) \\ &\approx \int_{t_n}^{t_{n+1}} L(\underline{q}, \underline{u}, \dot{\underline{q}}) \; dt, \end{aligned} \tag{3.31}$$

where $\underline{u}_n$ is the discrete control configuration at time t_n. If non-conservative contributions depend on $\underline{u}$, the same temporal approximation applies here as well.

3.6 Discrete Legendre transform and consistent energy evaluation

The discrete Euler-Lagrange-Equations can also be written as

$$\underline{p}_n^+ - \underline{p}_n^- = \underline{0} \tag{3.32a}$$

$$\underline{g}(\underline{q}_{n+1}) = \underline{0}, \tag{3.32b}$$

where the conjugate momenta $\underline{p}_n^+, \underline{p}_n^-$ at time t_n for a constrained and non-conservative system are defined via the discrete Legendre transforms

$$\underline{p}_n^-(\underline{q}_n, \underline{q}_{n+1}) = -\frac{\partial L_d(\underline{q}_n, \underline{q}_{n+1})}{\partial \underline{q}_n} + \frac{1}{2}\underline{\underline{G}}_d^T(\underline{q}_n) \cdot \underline{\lambda}_n - \underline{f}_n^{\text{ext}-} \tag{3.33a}$$

$$\underline{p}_n^+(\underline{q}_{n-1}, \underline{q}_n) = \frac{\partial L_d(\underline{q}_{n-1}, \underline{q}_n)}{\partial \underline{q}_n} - \frac{1}{2}\underline{\underline{G}}_d^T(\underline{q}_n) \cdot \underline{\lambda}_n + \underline{f}_n^{\text{ext}+}. \tag{3.33b}$$

This allows for a new interpretation of the Euler-Lagrange-Equations in terms of forcing the equivalence of conjugate momenta, i.e. $\underline{p}_n^+ = \underline{p}_n^-$. While $\underline{p}_n^+$ refers to the left-sided momentum evaluation (in terms of temporal evolution), $\underline{p}_n^-$ refers to the right-sided evaluation. In other words, the left-sided part of the time integral approximation on the interval $[t_{n-1}, t_n]$ is mapped forward in time (sign $+$) and the right-sided integral approximation on the interval $[t_n, t_{n+1}]$ is mapped backward in time (sign $-$) to obtain the conjugate momentum $\underline{p}_n = \underline{p}_n^+ = \underline{p}_n^-$ at time t_n.

The introduction of conjugate momenta is used to provide consistent initial conditions in a forward dynamics simulation and allows for a consistent energy evaluation.

3.6.1 Consistent initial conditions

At time $t = 0$, the Euler-Lagrange-Equations (3.17a) can not be evaluated because the configuration $\underline{q}_{n-1}$ does not exist. Instead, the Equations

$$\bar{\underline{p}}_0 - \underline{p}_0^-(\underline{q}_0, \underline{q}_1) = \underline{0} \tag{3.34a}$$

$$\underline{g}(\underline{q}_1) = \underline{0} \tag{3.34b}$$

are used in the first time step, where $\bar{\underline{p}}_0$ is the externally prescribed initial momentum. Using the discrete Legendre transform to prescribe the initial momentum enforces consistent initial conditions. If instead the initial velocity $\dot{\underline{q}}_0$ is prescribed and discretised via finite differences, then the initial condition would not be fulfilled at $t = 0$ but somewhere within the interval $[t_0, t_1]$.

Note that equivalently to the approach in Equation (3.34a), end conditions at time t_N can be prescribed such that

$$\underline{p}_N^+(\underline{q}_{N-1}, \underline{q}_N) - \bar{\underline{p}}_N = \underline{0}, \tag{3.35}$$

where $\bar{\underline{p}}_N$ is the prescribed momentum at t_N. This is of interest when solving optimal control problems including rest-to-rest constraints.

3.6.2 Consistent energy evaluation

While the evaluation of the potential energy $\Pi(\underline{q})$ only requires the configuration $\underline{q}$ to be known, the kinetic energy $T(\underline{q}, \underline{\dot{q}})$ additionally requires the time derivative of the configuration $\underline{\dot{q}}$. In the discrete space, the potential energy Π_n at time t_n can be evaluated via

$$\Pi_n = \Pi(\underline{q}_n), \tag{3.36}$$

however, evaluation of the kinetic energy would require some finite difference discretisation for $\underline{\dot{q}}$, as the configuration $\underline{q}_n$ is only available at the discrete time nodes t_n. Using finite differences, e.g. in the interval $[t_n, t_{n+1}]$, would however not represent the velocity at time t_n but in the middle of the interval $[t_n, t_{n+1}]$.

To achieve a consistent energy evaluation, the discrete Legendre transform can be used. After evaluating the conjugate momentum $\underline{p}_n$ at time t_n with either $\underline{p}_n^+$ or $\underline{p}_n^-$ as illustrated in Equation (3.33), the kinetic energy at time t_n is obtained via

$$T_n = \frac{1}{2}\, \underline{p}_n \cdot \underline{\underline{M}}^{-1}(\underline{q}_n) \cdot \underline{p}_n, \tag{3.37}$$

where $\underline{\underline{M}}(\underline{q}_n)$ is the mass matrix.

For the Lagrangian introduced in (3.1) representing mechanical systems (where the kinetic energy depends on the squared velocity and the potential is independent of $\underline{\dot{q}}$), the mass matrix can generally be obtained via

$$\underline{\underline{M}}(\underline{q}) = \frac{\partial^2 L(\underline{q}, \underline{\dot{q}})}{\partial \underline{\dot{q}}^2}. \tag{3.38}$$

4 Electromechanical coupling in deformable continua – the actuator model

In literature, dielectric elastomer simulation seems to be separated into two groups. On the one hand, there are research groups that come from practical applications, where different materials and settings are explored via test rigs and measurement data is compared to simple and easy to use (so called lumped parameter) simulations models, e.g. [Pelr98, Tröl13, Li11, Carp15, Kofo05]. On the other hand, there are research groups with a continuum mechanics background that establish their simulation models on electromechanically coupled three-dimensional field theory, but face the difficulty to provide model parameters that match real materials, e.g. [Dorf05, Vu07b, Park12, Klas16, Ask10]. Even though quite good fits to measurement data can be obtained by using lumped parameter models [Rizz15], it has also been shown that these models sometimes not adequately represent the physics and functional principles of dielectric elastomer deformation [Wiss07b]. In this work, the modelling is based on the electromechanically coupled three-dimensional field theory. On this basis, the derivation and performance of lumped parameter models is investigated in Chapter 7. Note that this chapter is to a great extend based on [Schl16c].

In general, all time-dependent electromagnetic phenomena in three-dimensional space are covered by the Maxwell equations

$$\nabla_{\boldsymbol{x}} \times \boldsymbol{e} + \dot{\mathfrak{b}} = \boldsymbol{0} \tag{4.1a}$$

$$\nabla_{\boldsymbol{x}} \cdot \mathfrak{d} = \rho^f \tag{4.1b}$$

$$\nabla_{\boldsymbol{x}} \times \boldsymbol{h} - \dot{\mathfrak{d}} = \boldsymbol{j}^f \tag{4.1c}$$

$$\nabla_{\boldsymbol{x}} \cdot \mathfrak{b} = 0, \tag{4.1d}$$

with the electric field $\boldsymbol{e}$, magnetic induction $\mathfrak{b}$, magnetic field $\boldsymbol{h}$, electric displacement $\mathfrak{d}$, electric current density $\boldsymbol{j}^f$ and the density of free charges ρ^f, all being spatial quantities. The Maxwell Equations originate from fundamental laws about the interaction between single discrete charges that are generalised for fields with a continuous charge density distribution [Grif12]. Usually, when exploring the behaviour of dielectric elastomer actuators, only a reduced subset of the Maxwell Equations is considered. It is assumed that electrodynamic

effects take place on a considerably smaller time scale than elastodynamic effects, thus $\dot{\mathfrak{b}} = \mathbf{0}$ and $\dot{\mathfrak{d}} = \mathbf{0}$ is assumed. In order to keep the model simple, magnetic interactions are not considered, resulting in equations describing electrostatics.

In Section 4.1, the electrostatic equations are introduced in a material context and the coupling with mechanical fields is investigated. Then, in Section 4.2, an integral form for the electromechanically coupled problem is presented and verified. Based on this integral form, a variational time discretisation scheme is derived for the electromechanically coupled problem in Section 4.3. Finally, in Section 4.4, some numerical examples illustrate the application of the derived framework for dielectric elastomer simulation.

4.1 Electromechanically coupled equations of motion

In the absence of magnetic fields, electric currents and free charges and with the assumption of quasi-static theory, Maxwell's equations (4.1) reduce to

$$\nabla_{\boldsymbol{x}} \times \boldsymbol{e} = \mathbf{0} \tag{4.2a}$$

$$\nabla_{\boldsymbol{x}} \cdot \mathfrak{d} = 0 \tag{4.2b}$$

describing electrostatics [Dorf05, Grif12, Vu07b]. Considering the integral forms of Equations (4.2)

$$\oint_{\mathcal{C}_t} \boldsymbol{e} \cdot d\boldsymbol{s} = 0 \tag{4.3a}$$

$$\oint_{\mathcal{S}_t} \mathfrak{d} \cdot d\boldsymbol{a} = 0 \tag{4.3b}$$

with a closed curve $\mathcal{C}_t$ bounding a regular surface $\mathcal{S}_t$ of the spatial domain $\mathcal{B}_t$, material counterparts for $\boldsymbol{e}$ and $\mathfrak{d}$ can be obtained by rewriting the integral forms with the help of Equations (2.3)

$$\oint_{\mathcal{C}_0} \left(\boldsymbol{F}^T \cdot \boldsymbol{e}\right) \cdot d\boldsymbol{S} = 0 \tag{4.4a}$$

$$\oint_{\mathcal{S}_0} \left(J\boldsymbol{F}^{-1} \cdot \mathfrak{d}\right) \cdot d\boldsymbol{A} = 0 \tag{4.4b}$$

with associated material quantities $\mathcal{C}_0$ and $\mathcal{S}_0$ of $\mathcal{B}_0$. The definitions

$$\boldsymbol{E} = \boldsymbol{F}^T \cdot \boldsymbol{e} \tag{4.5a}$$

$$\boldsymbol{D} = J\boldsymbol{F}^{-1} \cdot \mathfrak{d} \tag{4.5b}$$

motivate a material counterpart to Equations (4.2)

$$\nabla_{\boldsymbol{X}} \times \boldsymbol{E} = \boldsymbol{0} \tag{4.6a}$$

$$\nabla_{\boldsymbol{X}} \cdot \boldsymbol{D} = 0, \tag{4.6b}$$

using the material electric field $\boldsymbol{E}$ and the material electric displacement $\boldsymbol{D}$ [Vu12a]. From Equation (4.6a), it directly follows that $\boldsymbol{E}$ can be expressed as the gradient of a scalar electric potential ϕ

$$\boldsymbol{E} = -\frac{\partial \phi(\boldsymbol{X})}{\partial \boldsymbol{X}}. \tag{4.7}$$

Due to polarisation effects, an electric field exerts a material force $\boldsymbol{b}_0^{\mathrm{ele}} \in \mathbb{R}^3$ on condensed matter that is given by

$$\boldsymbol{b}_0^{\mathrm{ele}} = \frac{\partial \left(\boldsymbol{F}^{-T} \cdot \boldsymbol{E} \right)}{\partial \boldsymbol{X}} \cdot \boldsymbol{P}^{\mathrm{pol}}, \tag{4.8}$$

where $\boldsymbol{P}^{\mathrm{pol}} \in \mathbb{R}^3$ is the material polarisation vector [Pao78, Vu12a]. Together with the relationship

$$\boldsymbol{D} = \varepsilon_0 J \boldsymbol{C}^{-1} \cdot \boldsymbol{E} + \boldsymbol{P}^{\mathrm{pol}}, \tag{4.9}$$

and Equations (4.6), the force $\boldsymbol{b}_0^{\mathrm{ele}}$ can be rewritten as [Vu07a]

$$\boldsymbol{b}_0^{\mathrm{ele}} = \nabla_{\boldsymbol{X}} \cdot \left(\boldsymbol{F}^{-T} \cdot \boldsymbol{E} \otimes \boldsymbol{D} - \frac{1}{2} \varepsilon_0 J \left[\boldsymbol{E} \cdot \boldsymbol{C}^{-1} \cdot \boldsymbol{E} \right] \boldsymbol{F}^{-T} \right). \tag{4.10}$$

This allows for the introduction of an electrostatic stress tensor

$$\boldsymbol{P}^{\mathrm{ele}} = \boldsymbol{F}^{-T} \cdot \boldsymbol{E} \otimes \boldsymbol{D} - \frac{1}{2} \varepsilon_0 J \left[\boldsymbol{E} \cdot \boldsymbol{C}^{-1} \cdot \boldsymbol{E} \right] \boldsymbol{F}^{-T}, \tag{4.11}$$

such that

$$\boldsymbol{b}_0^{\mathrm{ele}} = \nabla_{\boldsymbol{X}} \cdot \boldsymbol{P}^{\mathrm{ele}}. \tag{4.12}$$

The volume force $\boldsymbol{b}_0$ in Equation (2.25) is split into a purely mechanical part $\boldsymbol{b}_0^{\mathrm{mech}}$ and an electrical term $\boldsymbol{b}_0^{\mathrm{ele}}$, such that

$$\boldsymbol{b}_0 = \boldsymbol{b}_0^{\mathrm{mech}} + \boldsymbol{b}_0^{\mathrm{ele}}. \tag{4.13}$$

If the material force (4.12) is then inserted into the mechanical momentum balance (2.25), the electromechanically coupled problem can conveniently be written as

$$\nabla_{\boldsymbol{X}} \cdot \boldsymbol{P}^{\mathrm{tot}} + \boldsymbol{b}_0^{\mathrm{mech}} = \rho_0 \ddot{\boldsymbol{x}} \quad \text{in} \quad \mathcal{B}_0 \tag{4.14a}$$

$$\boldsymbol{P}^{\mathrm{tot}} \cdot \boldsymbol{N} = \bar{\boldsymbol{T}} \quad \text{in} \quad \partial \mathcal{B}_0 \tag{4.14b}$$

$$\nabla_{\boldsymbol{X}} \cdot \boldsymbol{D} = 0 \quad \text{in} \quad \mathcal{B}_0 \tag{4.14c}$$

$$\boldsymbol{D} \cdot \boldsymbol{N} = -\bar{Q} \quad \text{in} \quad \partial \mathcal{B}_{0q}, \tag{4.14d}$$

where the total stress $\boldsymbol{P}^{\mathrm{tot}}$ is composed of

$$\boldsymbol{P}^{\mathrm{tot}} = \boldsymbol{P}^{\mathrm{ela}} + \boldsymbol{P}^{\mathrm{vis}} + \boldsymbol{P}^{\mathrm{ele}}, \tag{4.15}$$

$\bar{\boldsymbol{T}}$ is an external traction on the boundary and $\bar{Q}$ is the electric charge density on the boundary.

If Equations (4.14) are complemented with initial conditions and constitutive laws, they allow for solving electromechanically coupled problems including mechanical inertia terms and viscoelastic behaviour. In the next section, a corresponding integral form is introduced.

4.2 Electromechanically coupled integral form

This section is split into three parts. In Section 4.2.1, the conservative contributions are considered, whereas in Section 4.2.2, non-conservative contributions are taken into account and the Lagrange-d'Alembert principle is applied to show equivalence of the integral form with the strong form presented in Section 4.1. In Section 4.2.3, an electromechanically coupled hyperelastic material model is introduced.

4.2.1 Conservative contributions

The dynamic behaviour of the system is covered by the action S (see Equation (3.2)) that is here defined as the space-time integral

$$S[\boldsymbol{x}, \phi] = \int_{t_0}^{t_N} \int_{\mathcal{B}_0} \mathcal{L}(\dot{\boldsymbol{x}}, \boldsymbol{F}, \boldsymbol{E})\, dV dt \tag{4.16}$$

over the Lagrangian density

$$\mathcal{L}(\dot{\boldsymbol{x}}, \boldsymbol{F}, \boldsymbol{E}) = \mathcal{T}(\dot{\boldsymbol{x}}) - \Omega(\boldsymbol{F}, \boldsymbol{E}) \tag{4.17}$$

for the time interval $[t_0, t_N]$. The kinetic energy density can be taken from Equation (2.29), while the coupled potential energy density $\Omega(\boldsymbol{F}, \boldsymbol{E})$ extends the purely mechanical energy density Φ from Equation (2.27) with purely electrical as well as electromechanical coupling terms. Note that instead of using the electric field $\boldsymbol{E}$ as the independent electrical variable, also the electric

displacement field $\boldsymbol{D}$ might be used as shown in [Dorf05]. The variation of the action $S[\boldsymbol{x}, \phi]$ is obtained by

$$\delta S = \int_{t_0}^{t_N} \int_{\mathcal{B}_0} (\delta \mathcal{T} - \delta \Omega)\, dV\, dt, \tag{4.18}$$

with the variation of the kinetic energy density δT and the variation of the potential energy density $\delta\Omega$. While the variation of the kinetic energy density can explicitly be written as

$$\delta \mathcal{T} = \rho_0 \dot{\boldsymbol{x}} \cdot \delta \dot{\boldsymbol{x}}, \tag{4.19}$$

the variation of the potential energy density is given by

$$\delta \Omega = \frac{\partial \Omega}{\partial \boldsymbol{F}} : \delta \boldsymbol{F} + \frac{\partial \Omega}{\partial \boldsymbol{E}} \cdot \delta \boldsymbol{E}, \tag{4.20}$$

where the colon (:) denotes the double contraction which in this case is the Frobenius inner product. Considering the relationships

$$\delta \boldsymbol{F} = \frac{\partial \delta \boldsymbol{x}}{\partial \boldsymbol{X}} \tag{4.21}$$

and

$$\delta \boldsymbol{E} = -\frac{\partial \delta \phi}{\partial \boldsymbol{X}}, \tag{4.22}$$

applying integration by parts and using Gauss's divergence theorem

$$\int_{\mathcal{B}_0} \nabla_{\boldsymbol{X}} \cdot (\bullet)\, dV = \oint_{\partial \mathcal{B}_0} (\bullet) \cdot \boldsymbol{N}\, dA, \tag{4.23}$$

the variation of the action δS can be expressed in terms of the translational variation $\delta \boldsymbol{x}$ and the electric potential variation $\delta\phi$ as

$$\begin{aligned} \delta S = \int_{t_0}^{t_N} \Bigg\{ \int_{\mathcal{B}_0} \left[\delta \boldsymbol{x} \cdot \left(-\rho_0 \ddot{\boldsymbol{x}} + \nabla_{\boldsymbol{X}} \cdot \frac{\partial \Omega}{\partial \boldsymbol{F}} \right) + \delta \phi \left(-\nabla_{\boldsymbol{X}} \cdot \frac{\partial \Omega}{\partial \boldsymbol{E}} \right) \right] dV \\ + \int_{\partial \mathcal{B}_0} \left[\delta \boldsymbol{x} \cdot \left(-\frac{\partial \Omega}{\partial \boldsymbol{F}} \cdot \boldsymbol{N} \right) + \delta \phi \left(\frac{\partial \Omega}{\partial \boldsymbol{E}} \cdot \boldsymbol{N} \right) \right] dA \Bigg\} dt. \end{aligned} \tag{4.24}$$

Note that the variation $\delta \boldsymbol{x}$ vanishes at the time boundaries as illustrated in Equation (2.26).

4.2.2 Non-conservative contributions

Non-conservative forces result from external surface stress $\bar{\boldsymbol{T}}$, associated with the surface stress work $W^{\boldsymbol{T}}$, external volume force $\boldsymbol{b}_0^{\text{mech}}$, associated with the volume force work $W^{\boldsymbol{b}}$, external surface charge density $\bar{Q}$, associated with the surface charge work W^{Q}, and internal viscous stress $\boldsymbol{P}^{\text{vis}}$, associated with the viscous work W^{vis}. The total non-conservative work W^{ext} and its variation δW^{ext} are given by

$$W^{\text{ext}} = W^{\boldsymbol{T}} + W^{\boldsymbol{b}} + W^{Q} + W^{\text{vis}} \tag{4.25}$$

and

$$\delta W^{\text{ext}} = \delta W^{\boldsymbol{T}} + \delta W^{\boldsymbol{b}} + \delta W^{Q} + \delta W^{\text{vis}}, \tag{4.26}$$

respectively. The variation of the non-conservative work contributions

$$W^{\boldsymbol{T}} = \int_{\partial\mathcal{B}_0} \boldsymbol{x} \cdot \bar{\boldsymbol{T}} dA \tag{4.27a}$$

$$W^{\boldsymbol{b}} = \int_{\mathcal{B}_0} \boldsymbol{x} \cdot \boldsymbol{b}_0^{\text{mech}} dV \tag{4.27b}$$

$$W^{Q} = -\int_{\partial\mathcal{B}_0} \phi \bar{Q} dA \tag{4.27c}$$

$$W^{\text{vis}} = -\int_{\mathcal{B}_0} \boldsymbol{F} : \boldsymbol{P}^{\text{vis}} dV \tag{4.27d}$$

is given by

$$\delta W^{\boldsymbol{T}} = \int_{\partial\mathcal{B}_0} \delta\boldsymbol{x} \cdot \bar{\boldsymbol{T}} dA \tag{4.28a}$$

$$\delta W^{\boldsymbol{b}} = \int_{\mathcal{B}_0} \delta\boldsymbol{x} \cdot \boldsymbol{b}_0^{\text{mech}} dV \tag{4.28b}$$

$$\delta W^{Q} = -\int_{\partial\mathcal{B}_0} \delta\phi \bar{Q} dA \tag{4.28c}$$

$$\delta W^{\text{vis}} = -\int_{\mathcal{B}_0} \delta\boldsymbol{F} : \boldsymbol{P}^{\text{vis}} dV. \tag{4.28d}$$

Note that non-conservative quantities $\bar{\boldsymbol{T}}, \boldsymbol{b}_0^{\text{mech}}, \bar{Q}$ and $\boldsymbol{P}^{\text{vis}}$ are treated as fixed during variation. Using integration by parts, the divergence theorem and relationship (4.21), the variation of the viscous work (4.28d) is expressed as

$$\delta W^{\text{vis}} = \int_{\mathcal{B}_0} \delta\boldsymbol{x} \cdot \left(\nabla_{\boldsymbol{X}} \cdot \boldsymbol{P}^{\text{vis}}\right) dV - \int_{\partial\mathcal{B}_0} \delta\boldsymbol{x} \cdot \boldsymbol{P}^{\text{vis}} \cdot \boldsymbol{N}\, dA. \tag{4.29}$$

Inserting the variational form of the action (4.24) and the non-conservative work (4.28) into the Lagrange-d'Alembert principle (3.21) that requires stationarity and considering the fundamental lemma of the calculus of variations, four independent equations

$$\nabla_{\boldsymbol{X}} \cdot \left(\frac{\partial \Omega}{\partial \boldsymbol{F}} + \boldsymbol{P}^{\mathrm{vis}} \right) + \boldsymbol{b}_0^{\mathrm{mech}} = \rho_0 \ddot{\boldsymbol{x}} \qquad \text{in } \mathcal{B}_0 \tag{4.30a}$$

$$\left(\frac{\partial \Omega}{\partial \boldsymbol{F}} + \boldsymbol{P}^{\mathrm{vis}} \right) \cdot \boldsymbol{N} = \bar{\boldsymbol{T}} \qquad \text{in } \partial\mathcal{B}_0 \tag{4.30b}$$

$$-\nabla_{\boldsymbol{X}} \cdot \frac{\partial \Omega}{\partial \boldsymbol{E}} = 0 \qquad \text{in } \mathcal{B}_0 \tag{4.30c}$$

$$-\frac{\partial \Omega}{\partial \boldsymbol{E}} \cdot \boldsymbol{N} = -\bar{Q} \qquad \text{in } \partial\mathcal{B}_0, \tag{4.30d}$$

are obtained. If the coupled potential energy density Ω is chosen such that

$$\frac{\partial \Omega}{\partial \boldsymbol{F}} = \boldsymbol{P}^{\mathrm{ela}} + \boldsymbol{P}^{\mathrm{ele}} \tag{4.31}$$

and

$$\frac{\partial \Omega}{\partial \boldsymbol{E}} = -\boldsymbol{D}, \tag{4.32}$$

then the set of Equations (4.14) is recovered. This means that Equations (4.24) and (4.28) together with (3.21) form a variational setting that is consistent to the problem formulated in Equations (4.14).

4.2.3 Coupled hyperelastic material model

According to Dorfmann et. al. 2004 [Dorf05], from a constitutive point of view, electroelastic materials have much in common with transversely isotropic materials like fibre reinforced composites, where the preferred direction in electroelastic materials is affected by the electric field. The main difference is that the electric field vector is not normalised as opposed to the fibre direction of composites. Therefore, electromechanically coupled, hyperelastic material models for isotropic DEAs can be formulated based on six invariants

$$I_1 = \boldsymbol{C} : \boldsymbol{1} \tag{4.33a}$$

$$I_2 = \frac{1}{2}\Big[(\boldsymbol{C} : \boldsymbol{1})^2 - \boldsymbol{C}^2 : \boldsymbol{1} \Big] \tag{4.33b}$$

$$I_3 = \det(\boldsymbol{C}) \tag{4.33c}$$

$$I_4 = \boldsymbol{E} \cdot \boldsymbol{E} \tag{4.33d}$$

$$I_5 = \boldsymbol{E} \cdot \boldsymbol{C}^{-1} \cdot \boldsymbol{E} \tag{4.33e}$$

$$I_6 = \boldsymbol{E} \cdot \boldsymbol{C}^{-2} \cdot \boldsymbol{E}. \tag{4.33f}$$

From the electrostatic stress given in Equation (4.11) it follows that the potential energy density Ω must be composed of a condensed matter term Φ and a free space term including the vacuum permittivity ε_0 such that

$$\Omega(\boldsymbol{F}, \boldsymbol{E}) = \Phi(\boldsymbol{F}, \boldsymbol{E}) - \frac{1}{2}\varepsilon_0 J \boldsymbol{C}^{-1} : [\boldsymbol{E} \otimes \boldsymbol{E}], \tag{4.34}$$

as shown in [Vu07b]. Here, the Neo-Hookean approach from Vu et. al. [Vu07b] is used, such that Φ becomes

$$\Phi^{\mathrm{V_U}}(\boldsymbol{F}, \boldsymbol{E}) = \Phi^{\mathrm{BW}}(\boldsymbol{F}) + c_1 \boldsymbol{E} \cdot \boldsymbol{E} + c_2 \boldsymbol{C} : [\boldsymbol{E} \otimes \boldsymbol{E}], \tag{4.35}$$

with two electrical parameters c_1 and c_2 and Φ^{BW} taken from Equation (2.20). Note that c_1 is a purely electrical parameter, whereas c_2 affects the electromechanical coupling term.

This material model allows for easy identification of the parameters:

1. The mechanical Lamé parameters μ and λ can be identified by comparing static and purely mechanical simulation results to measurement data of a specimen. In case of incompressible materials, only one parameter has to be determined. From tensile testing results, the Young's modulus Y can be identified.

2. Evaluating static coupled problems, the coupling parameter c_2 can be determined such that the contraction for applied voltages matches measurement data. Note that the contraction is independent of parameter c_1 since it is a purely electrical parameter as seen in Equation (4.35).

3. Parameter c_1 can be identified by comparing simulation results to the real amount of charge that is necessary to maintain a voltage. To illustrate that point, the capacity of the simulated geometry has to match the capacity of the real actuator. Parameter c_1 affects the potential energy that is stored in the electric field of the actuator.

4. The damping parameter η that affects the viscoelastic losses can be identified by evaluating hysteresis effects in stress-strain curves or numerous other possibilities as presented in [Lake04].

Note that the potential energy density (4.34) can be extended to allow for gravity effects by adding the term

$$\Phi_g = -\rho_0 \boldsymbol{g}_{\mathrm{v}} \cdot \boldsymbol{x} \tag{4.36}$$

where $\boldsymbol{g}_{\mathrm{v}} \in \mathbb{R}^3$ is the gravitation vector.

4.3 Discretisation, linearisation and implementation

The weak form of the electromechanically coupled problem will first be discretised in space via finite elements (see Section 2.5), yielding a spatially discrete Lagrangian. This spatially discrete Lagrangian will then be used as a basis to derive a structure preserving integration scheme as shown in Chapter 3. In order to solve the non-linear variational integration scheme numerically within a Newton-Raphson scheme, the equations need to be linearised with respect to the unknown configuration of the next time step. In the sequel it is shown that the parameter α of the general midpoint quadrature (see Equation (3.4)) can not be chosen arbitrarily in the electromechanically coupled case as a result of missing inertia terms for the electrostatic variables. Finally, the electromechanically coupled variational integration scheme is implemented into a custom finite element software written in C++. Note that the discrete finite element configuration is denoted with $\underline{r}$ (instead of $\underline{q}$) throughout this chapter. This allows to separate finite element degrees of freedom from multibody system degrees of freedom that are introduced in Chapter 5.

4.3.1 Discretisation

Introducing a space-time grid, the action integral (4.16) can be split into small time sections $[t_n, t_{n+1}]$ and finite elements $\mathcal{B}_0^{\mathrm{el}}$, such that

$$S = \sum_{n=0}^{N-1} \int_{t_n}^{t_{n+1}} \biguplus_{\mathrm{el}} \int_{\mathcal{B}_0^{\mathrm{el}}} \mathcal{L}(\dot{\boldsymbol{x}}, \boldsymbol{F}, \boldsymbol{E})\, dV dt. \tag{4.37}$$

In addition to the finite element approaches for translational quantities $\boldsymbol{x}, \dot{\boldsymbol{x}}$ and $\boldsymbol{F}$ that read (compare to Equations (2.32) and (2.33))

$$\boldsymbol{x}(\boldsymbol{X}, t) \approx \underline{r}^{\mathrm{el}}(t) \odot \underline{\boldsymbol{N}}_{\mathrm{el}}^{\mathrm{trans}}(\boldsymbol{X}) \tag{4.38}$$

$$\dot{\boldsymbol{x}}(\boldsymbol{X}, t) \approx \dot{\underline{r}}^{\mathrm{el}}(t) \odot \underline{\boldsymbol{N}}_{\mathrm{el}}^{\mathrm{trans}}(\boldsymbol{X}) \tag{4.39}$$

$$\boldsymbol{F}(\boldsymbol{X}, t) \approx \underline{r}^{\mathrm{el}}(t) \odot \frac{\partial \underline{\boldsymbol{N}}_{\mathrm{el}}^{\mathrm{trans}}(\boldsymbol{X})}{\partial \boldsymbol{X}}, \tag{4.40}$$

respectively, approximations for electrical quantities ϕ and $\boldsymbol{E}$ are introduced such that

$$\phi(\boldsymbol{X}, t) \approx \underline{r}^{\mathrm{el}}(t) \odot \underline{N}_{\mathrm{el}}^{\mathrm{ele}}(\boldsymbol{X}) \tag{4.41}$$

and

$$\boldsymbol{E}(\boldsymbol{X}, t) \approx -\underline{r}^{\mathrm{el}}(t) \odot \frac{\partial \underline{N}_{\mathrm{el}}^{\mathrm{ele}}(\boldsymbol{X})}{\partial \boldsymbol{X}}. \tag{4.42}$$

using finite element shape functions $\underline{N}_{\mathrm{el}}^{\mathrm{ele}}$. The array $\underline{r}^{\mathrm{el}}$ contains the values of all degrees of freedom of the element n_{dof}, both mechanical and electrical. If linear Lagrange shape functions are used for all space dimensions and the electric potential, $\underline{r}^{\mathrm{el}}$ contains three translations and one electric potential for each node of the element. Note that $\underline{N}_{\mathrm{el}}^{\mathrm{ele}} \in \mathbb{R}^{n_{\mathrm{dof}}}$ and $\partial \underline{N}_{\mathrm{el}}^{\mathrm{ele}}(\boldsymbol{X})/\partial \boldsymbol{X} \in \mathbb{R}^{n_{\mathrm{dof}} \times n_{\mathrm{dim}}}$ with $n_{\mathrm{dim}} = 3$. The approach of summarising multidisciplinary configuration variables (mechanical translations and electrical potentials) into a single configuration array $\underline{r}^{\mathrm{el}}$ when handling multiplication with shape functions is taken from [Bang07].

The spatially discrete Lagrangian L is obtained by introducing the approximations given in Equations (2.32), (2.33), (4.41) and (4.42) into the Lagrangian density $\mathcal{L}(\dot{\boldsymbol{x}}, \boldsymbol{F}, \boldsymbol{E})$ and integrating over space

$$L(\underline{r}, \underline{\dot{r}}) = \biguplus_{\mathrm{el}} \int_{\mathcal{B}_0^{\mathrm{el}}} \mathcal{L}\left(\underline{\dot{r}}^{\mathrm{el}} \odot \underline{\boldsymbol{N}}_{\mathrm{el}}^{\mathrm{trans}}, \underline{r}^{\mathrm{el}} \odot \frac{\partial \underline{\boldsymbol{N}}_{\mathrm{el}}^{\mathrm{trans}}}{\partial \boldsymbol{X}}, -\underline{r}^{\mathrm{el}} \odot \frac{\partial \underline{N}_{\mathrm{el}}^{\mathrm{ele}}}{\partial \boldsymbol{X}} \right) dV, \quad (4.43)$$

with the global array $\underline{r}(t)$ containing the values of all degrees of freedom of the model, i.e.

$$\underline{r}(t) = \biguplus_{\mathrm{el}} \underline{r}^{\mathrm{el}}(t) \quad (4.44)$$

and

$$\underline{\dot{r}}(t) = \biguplus_{\mathrm{el}} \underline{\dot{r}}^{\mathrm{el}}(t). \quad (4.45)$$

Note that the spatial integral in Equation (4.43) can numerically be evaluated using a Gauss quadrature as introduced in Equation (2.34).

The spatially discrete Lagrangian (4.43) is temporally discretised according to Equation (3.4) to obtain the discrete Lagrangian $L_d(\underline{r}_n, \underline{r}_{n+1})$. Inserting the discrete Lagrangian into Equation (3.10) and evaluating the derivatives, the variation of the discrete action can be given as

$$\begin{aligned} \delta S_d = \Delta t \sum_{n=1}^{N-1} \delta \underline{r}_n \odot \biguplus_{\mathrm{el}} \Bigg\{ & \\ & \int_{\mathcal{B}_0^{\mathrm{el}}} \left[\underline{\boldsymbol{N}}_{\mathrm{el}}^{\mathrm{trans}} \rho_0 \cdot \underline{\boldsymbol{N}}_{\mathrm{el}}^{\mathrm{trans}} \right] dV \odot \frac{-\underline{r}_{n+1}^{\mathrm{el}} + 2\underline{r}_n^{\mathrm{el}} - \underline{r}_{n-1}^{\mathrm{el}}}{\Delta t^2} \\ & - \int_{\mathcal{B}_0^{\mathrm{el}}} \left[\partial_{\boldsymbol{X}} \underline{\boldsymbol{N}}_{\mathrm{el}}^{\mathrm{trans}} : \left(\alpha \partial_{\boldsymbol{F}} \Omega_n^- + (1-\alpha) \partial_{\boldsymbol{F}} \Omega_n^+ \right) \right] dV \\ & + \int_{\mathcal{B}_0^{\mathrm{el}}} \left[\partial_{\boldsymbol{X}} \underline{N}_{\mathrm{el}}^{\mathrm{ele}} \cdot \left(\alpha \partial_{\boldsymbol{E}} \Omega_n^- + (1-\alpha) \partial_{\boldsymbol{E}} \Omega_n^+ \right) \right] dV \Bigg\}, \end{aligned} \quad (4.46)$$

with abbreviated derivatives $\partial_\xi(\bullet) = {}^{\partial(\bullet)}/_{\partial\xi}$ and

$$\Omega_n^- = \Omega(\alpha \boldsymbol{F}_n + (1-\alpha)\boldsymbol{F}_{n+1}, \alpha \boldsymbol{E}_n + (1-\alpha)\boldsymbol{E}_{n+1}) \tag{4.47}$$

as well as

$$\Omega_n^+ = \Omega(\alpha \boldsymbol{F}_{n-1} + (1-\alpha)\boldsymbol{F}_n, \alpha \boldsymbol{E}_{n-1} + (1-\alpha)\boldsymbol{E}_n). \tag{4.48}$$

Note that this is consistent with the midpoint quadrature regarding $\underline{r}$ introduced in Equation (3.4) since $\boldsymbol{F}$ is linear in $\boldsymbol{x}$ and $\boldsymbol{E}$ is linear in ϕ. The finite element mass matrix is introduced by

$$\underline{\underline{M}}_r = \biguplus_{\text{el}} \int_{\mathcal{B}_0^{\text{el}}} \left[\underline{\boldsymbol{N}}_{\text{el}}^{\text{trans}} \rho_0 \cdot \underline{\boldsymbol{N}}_{\text{el}}^{\text{trans}} \right] dV \tag{4.49}$$

and hence constant in time. The acceleration term that is right multiplied to the mass matrix is abbreviated by

$$\underline{\ddot{r}}_d = \frac{\underline{r}_{n+1} - 2\underline{r}_n + \underline{r}_{n-1}}{\Delta t^2}, \tag{4.50}$$

and the translational ($\underline{R}_{\boldsymbol{F}}$) and electrical ($\underline{R}_{\boldsymbol{E}}$) contributions are defined by

$$\underline{R}_{\boldsymbol{F}} = \biguplus_{\text{el}} \int_{\mathcal{B}_0^{\text{el}}} \left[\partial_{\boldsymbol{X}} \underline{\boldsymbol{N}}_{\text{el}}^{\text{trans}} : \left(\alpha \partial_{\boldsymbol{F}} \Omega_n^- + (1-\alpha) \partial_{\boldsymbol{F}} \Omega_n^+ \right) \right] dV \tag{4.51}$$

and

$$\underline{R}_{\boldsymbol{E}} = \biguplus_{\text{el}} \int_{\mathcal{B}_0^{\text{el}}} \left[\partial_{\boldsymbol{X}} \underline{N}_{\text{el}}^{\text{ele}} \cdot \left(\alpha \partial_{\boldsymbol{E}} \Omega_n^- + (1-\alpha) \partial_{\boldsymbol{E}} \Omega_n^+ \right) \right] dV, \tag{4.52}$$

respectively. Then, the variation of the discrete action can be written as

$$\delta S_d = \Delta t \sum_{n=1}^{N-1} \delta \underline{r}_n \odot \left\{ -\underline{\underline{M}}_r \odot \underline{\ddot{r}}_d - \underline{R}_{\boldsymbol{F}} + \underline{R}_{\boldsymbol{E}} \right\}. \tag{4.53}$$

Equation (4.53) is the core of the numerical problem that has to be solved including linear inertia terms ($\underline{\underline{M}}_r \odot \underline{\ddot{r}}_d$), non-linear internal forces ($\underline{R}_{\boldsymbol{F}}$) and non-linear internal charge densities ($\underline{R}_{\boldsymbol{E}}$).

As described in Section 3.4, a midpoint quadrature is used to approximate the contribution of non-conservative quantities (4.28). While the viscous stress $\boldsymbol{P}^{\text{vis}}(\boldsymbol{F}, \dot{\boldsymbol{F}})$ is a function of the deformation gradient an hence the configuration $\underline{r}$ in the discrete setting, for the sake of simplicity it is assumed that the other non-conservative contributions $\bar{\boldsymbol{T}}(t), \boldsymbol{b}_0^{\text{mech}}(t)$ and $\bar{Q}(t)$ depend on time t only. For surface related contributions $\bar{\boldsymbol{T}}$ and $\bar{Q}$, the surface shape functions $\underline{\boldsymbol{N}}_{\text{f}}^{\text{trans}}$ and $\underline{N}_{\text{f}}^{\text{ele}}$ are introduced, where $\underline{\boldsymbol{N}}_{\text{f}}^{\text{trans}} \in \mathbb{R}^{n_{\text{face}} \times n_{\text{dim}}}$ connects

finite element surface degrees of freedom n_{face} on $\partial\mathcal{B}_0^{\text{f}}$ to translations $\boldsymbol{x}$ and $\underline{N}_{\text{f}}^{\text{ele}} \in \mathbb{R}^{n_{\text{face}}}$ connects surface degrees of freedom to electric potentials ϕ.

After spatial discretisation, temporal discretisation and variation of the non-conservative terms (4.28), the discretised virtual work contributions (see Section 3.4) are given by

$$\begin{aligned} \int_{t_0}^{t_N} \delta W_d^{\boldsymbol{T}}\, dt &= \Delta t \sum_{n=1}^{N-1} \delta \underline{r}_n \odot \underline{\bar{R}}_{\boldsymbol{T}} \\ \text{with} \quad \underline{\bar{R}}_{\boldsymbol{T}} &= \biguplus_{\text{f}} \int_{\partial\mathcal{B}_0^{\text{f}}} \underline{\boldsymbol{N}}_{\text{f}}^{\text{trans}} \cdot \left(\frac{\bar{\boldsymbol{T}}_n^- + \bar{\boldsymbol{T}}_n^+}{2} \right) dA, \end{aligned} \tag{4.54}$$

associated with the external surface stress $\bar{\boldsymbol{T}}$,

$$\begin{aligned} \int_{t_0}^{t_N} \delta W_d^{\boldsymbol{b}}\, dt &= \Delta t \sum_{n=1}^{N-1} \delta \underline{r}_n \odot \underline{\bar{R}}_{\boldsymbol{b}} \\ \text{with} \quad \underline{\bar{R}}_{\boldsymbol{b}} &= \biguplus_{\text{el}} \int_{\mathcal{B}_0^{\text{el}}} \underline{\boldsymbol{N}}_{\text{el}}^{\text{trans}} \cdot \left(\frac{(\boldsymbol{b}_0^{\text{mech}})_n^- + (\boldsymbol{b}_0^{\text{mech}})_n^+}{2} \right) dV, \end{aligned} \tag{4.55}$$

associated with the external volume force $\boldsymbol{b}_0^{\text{mech}}$ and

$$\begin{aligned} \int_{t_0}^{t_N} \delta W_d^{Q}\, dt &= -\Delta t \sum_{n=1}^{N-1} \delta \underline{r}_n \odot \underline{\bar{R}}_{Q} \\ \text{with} \quad \underline{\bar{R}}_{Q} &= \biguplus_{\text{f}} \int_{\partial\mathcal{B}_0^{\text{f}}} \underline{N}_{\text{f}}^{\text{ele}} \left(\frac{\bar{Q}_n^- + \bar{Q}_n^+}{2} \right) dA, \end{aligned} \tag{4.56}$$

associated with the external surface charge density $\bar{Q}$. The variation of the work caused by the viscous stress tensor is given by

$$\begin{aligned} \int_{t_0}^{t_N} \delta W_d^{\text{vis}}\, dt &= -\Delta t \sum_{n=1}^{N-1} \delta \underline{r}_n \odot \underline{R}_{\text{vis}} \\ \text{with} \quad \underline{R}_{\text{vis}} &= \biguplus_{\text{el}} \int_{\mathcal{B}_0^{\text{el}}} \partial_{\boldsymbol{X}} \underline{\boldsymbol{N}}_{\text{el}}^{\text{trans}} : \left(\frac{(\boldsymbol{P}^{\text{vis}})_n^- + (\boldsymbol{P}^{\text{vis}})_n^+}{2} \right) dV, \end{aligned} \tag{4.57}$$

where

$$(\boldsymbol{P}^{\text{vis}})_n^- = \boldsymbol{P}^{\text{vis}} \left(\frac{\boldsymbol{F}_n + \boldsymbol{F}_{n+1}}{2}, \frac{\boldsymbol{F}_{n+1} - \boldsymbol{F}_n}{\Delta t} \right) \tag{4.58}$$

and $(\boldsymbol{P}^{\text{vis}})_n^+ = (\boldsymbol{P}^{\text{vis}})_{n-1}^-$. Note that this is consistent with the midpoint quadrature regarding $\underline{r}$ introduced in Equation (3.25) since $\boldsymbol{F}$ is linear in $\boldsymbol{x}$

and hence $\underline{r}$. The variational integration scheme is obtained by evaluating the discrete version of the Lagrange-d'Alembert principle (3.25) with

$$\delta W_d = \delta W_d^{\boldsymbol{T}} + \delta W_d^{\boldsymbol{b}} + \delta W_d^{Q} + \delta W_d^{\mathrm{vis}}, \tag{4.59}$$

such that

$$\Delta t \sum_{n=1}^{N-1} \delta \underline{r}_n \odot \left\{ -\underline{\underline{M}}_r \odot \ddot{\underline{r}}_d - \underline{R}_{\boldsymbol{F}} + \underline{R}_{\boldsymbol{E}} + \bar{\underline{R}}_{\boldsymbol{T}} + \bar{\underline{R}}_{\boldsymbol{b}} - \bar{\underline{R}}_Q - \underline{R}_{\mathrm{vis}} \right\} = 0. \tag{4.60}$$

Due to the arbitrariness of the variations $\delta \underline{r}_n$, it follows that

$$\underline{F}_r(\underline{r}_{n-1}, \underline{r}_n, \underline{r}_{n+1}) = \underline{0} \tag{4.61}$$

with

$$\underline{F}_r = \Delta t \left(-\underline{\underline{M}}_r \odot \ddot{\underline{r}}_d - \underline{R}_{\boldsymbol{F}} + \underline{R}_{\boldsymbol{E}} + \bar{\underline{R}}_{\boldsymbol{T}} + \bar{\underline{R}}_{\boldsymbol{b}} - \bar{\underline{R}}_Q - \underline{R}_{\mathrm{vis}} \right), \tag{4.62}$$

where the size of $\underline{F}_r(\underline{r}_{n-1}, \underline{r}_n, \underline{r}_{n+1})$ corresponds to the total number of degrees of freedom in the finite element model. Note that the constant time step size Δt in Equation (4.62) might be crossed out. However, keeping the term results in better condition numbers during time integration as well as consistent units compared to the continuous system. Equation (4.61) is the non-linear coupled variational integration scheme. For given states $\underline{r}_{n-1}$ and $\underline{r}_n$, the next state $\underline{r}_{n+1}$ can be computed.

Like introduced in Section 3.6, the integration scheme can also be written in terms of conjugate momenta such that

$$\underline{F}_r(\underline{r}_{n-1}, \underline{r}_n, \underline{r}_{n+1}) = \underline{p}^{+}_{r,n}(\underline{r}_{n-1}, \underline{r}_n) - \underline{p}^{-}_{r,n}(\underline{r}_n, \underline{r}_{n+1}) = \underline{0}. \tag{4.63}$$

The conjugate momenta are then given by

$$\begin{aligned} \underline{p}^{+}_{r,n} = \Delta t \biguplus_{\mathrm{el}} \Bigg\{ \int_{\mathcal{B}_0^{\mathrm{el}}} \Bigg[& \underline{\boldsymbol{N}}_{\mathrm{el}}^{\mathrm{trans}} \rho_0 \cdot \underline{\boldsymbol{N}}_{\mathrm{el}}^{\mathrm{trans}} \odot \frac{\underline{r}_n^{\mathrm{el}} - \underline{r}_{n-1}^{\mathrm{el}}}{\Delta t^2} \\ & - (1-\alpha)\, \partial_{\boldsymbol{X}} \underline{\boldsymbol{N}}_{\mathrm{el}}^{\mathrm{trans}} : \partial_{\boldsymbol{F}} \Omega_n^{+} \\ & + (1-\alpha)\, \partial_{\boldsymbol{X}} \underline{N}_{\mathrm{el}}^{\mathrm{ele}} \cdot \partial_{\boldsymbol{E}} \Omega_n^{+} \\ & + \frac{1}{2}\, \underline{\boldsymbol{N}}_{\mathrm{el}}^{\mathrm{trans}} \cdot (\boldsymbol{b}_0^{\mathrm{mech}})_n^{+} - \frac{1}{2}\, \partial_{\boldsymbol{X}} \underline{\boldsymbol{N}}_{\mathrm{el}}^{\mathrm{trans}} : (\boldsymbol{P}^{\mathrm{vis}})_n^{+} \Bigg] dV \\ + \int_{\partial \mathcal{B}_0^{\mathrm{f}}} & \left[\frac{1}{2}\, \underline{\boldsymbol{N}}_{\mathrm{f}}^{\mathrm{trans}} \cdot \bar{\boldsymbol{T}}_n^{+} - \frac{1}{2}\, \underline{N}_{\mathrm{f}}^{\mathrm{ele}} \bar{Q}_n^{+} \right] dA \Bigg\} \end{aligned} \tag{4.64}$$

and

$$\begin{aligned}\underline{p}^{-}_{r,n} = \Delta t \bigcup_{\text{el}} \Bigg\{ \int_{\mathcal{B}_0^{\text{el}}} \Bigg[& \underline{\boldsymbol{N}}^{\text{trans}}_{\text{el}} \rho_0 \cdot \underline{\boldsymbol{N}}^{\text{trans}}_{\text{el}} \odot \frac{\underline{r}^{\text{el}}_{n+1} - \underline{r}^{\text{el}}_{n}}{\Delta t^2} \\ & + \alpha \, \partial_{\boldsymbol{X}} \underline{\boldsymbol{N}}^{\text{trans}}_{\text{el}} : \partial_{\boldsymbol{F}} \Omega^{-}_{n} - \alpha \, \partial_{\boldsymbol{X}} \underline{N}^{\text{ele}}_{\text{el}} \cdot \partial_{\boldsymbol{E}} \Omega^{-}_{n} \\ & - \frac{1}{2} \underline{\boldsymbol{N}}^{\text{trans}}_{\text{el}} \cdot (\boldsymbol{b}^{\text{mech}}_{0})^{-}_{n} + \frac{1}{2} \partial_{\boldsymbol{X}} \underline{\boldsymbol{N}}^{\text{trans}}_{\text{el}} : (\boldsymbol{P}^{\text{vis}})^{-}_{n} \Bigg] dV \\ + \int_{\partial \mathcal{B}_0^{\text{f}}} \Bigg[& - \frac{1}{2} \underline{\boldsymbol{N}}^{\text{trans}}_{\text{f}} \cdot \bar{\boldsymbol{T}}^{-}_{n} + \frac{1}{2} \underline{N}^{\text{ele}}_{\text{f}} \bar{Q}^{-}_{n} \Bigg] dA \Bigg\}, \end{aligned} \tag{4.65}$$

respectively.

4.3.2 Linearisation

For general midpoint quadrature with parameter $\alpha \in [0, 1]$, it follows that $\underline{R}_{\boldsymbol{F}} = \underline{R}_{\boldsymbol{F}}(\underline{r}_{n-1}, \underline{r}_{n}, \underline{r}_{n+1})$, $\underline{R}_{\boldsymbol{E}} = \underline{R}_{\boldsymbol{E}}(\underline{r}_{n-1}, \underline{r}_{n}, \underline{r}_{n+1})$ and Equation (4.61) can not be solved explicitly.

Implicit solver If Equation (4.61) is to be solved for arbitrary α and damping, the integration scheme $\underline{F}_r$ needs to be linearised with respect to the unknown configuration $\underline{r}_{n+1}$. The partial derivative of $\underline{F}_r$ with respect to $\underline{r}_{n+1}$ is obtained by

$$\frac{\partial \underline{F}_r}{\partial \underline{r}_{n+1}} = \Delta t \left(- \frac{\underline{\underline{M}}_r}{\Delta t^2} - \frac{\partial \underline{R}_{\boldsymbol{F}}}{\partial \underline{r}_{n+1}} + \frac{\partial \underline{R}_{\boldsymbol{E}}}{\partial \underline{r}_{n+1}} - \frac{\partial \underline{R}_{\text{vis}}}{\partial \underline{r}_{n+1}} \right). \tag{4.66}$$

After some calculation using the chain rule, the partial derivative of $\underline{F}_r$ can be written as

$$\frac{\partial \underline{F}_r}{\partial \underline{r}_{n+1}} = \Delta t \left(- \frac{\underline{\underline{M}}_r}{\Delta t^2} - \alpha(1-\alpha) \underline{\underline{K}} - \underline{\underline{D}} \right), \tag{4.67}$$

where

$$\begin{aligned} \underline{\underline{K}} = \bigcup_{\text{el}} \int_{\mathcal{B}_0^{\text{el}}} \Big[& \partial_{\boldsymbol{X}} \underline{\boldsymbol{N}}^{\text{trans}}_{\text{el}} : \left(\partial_{\boldsymbol{F}\boldsymbol{E}} \Omega^{-}_{n} \right) \cdot \left(- \partial_{\boldsymbol{X}} \underline{N}^{\text{ele}}_{\text{el}} \right) \\ & + \partial_{\boldsymbol{X}} \underline{\boldsymbol{N}}^{\text{trans}}_{\text{el}} : \left(\partial_{\boldsymbol{F}\boldsymbol{F}} \Omega^{-}_{n} \right) : \partial_{\boldsymbol{X}} \underline{\boldsymbol{N}}^{\text{trans}}_{\text{el}} \\ & + \left(- \partial_{\boldsymbol{X}} \underline{N}^{\text{ele}}_{\text{el}} \right) \cdot \left(\partial_{\boldsymbol{E}\boldsymbol{E}} \Omega^{-}_{n} \right) \cdot \left(- \partial_{\boldsymbol{X}} \underline{N}^{\text{ele}}_{\text{el}} \right) \\ & + \left(- \partial_{\boldsymbol{X}} \underline{N}^{\text{ele}}_{\text{el}} \right) \cdot \left(\partial_{\boldsymbol{E}\boldsymbol{F}} \Omega^{-}_{n} \right) : \partial_{\boldsymbol{X}} \underline{\boldsymbol{N}}^{\text{trans}}_{\text{el}} \Big] dV \end{aligned} \tag{4.68}$$

and

$$\underline{\underline{D}} = \biguplus_{\text{el}} \int_{\mathcal{B}_0^{\text{el}}} \Big[\partial_{\boldsymbol{X}} \underline{\boldsymbol{N}}_{\text{el}}^{\text{trans}} : \Big(\alpha(1-\alpha) \left(\partial_{\boldsymbol{F}} \boldsymbol{P}^{\text{vis}} \right)_n^- + \frac{\alpha}{\Delta t} \left(\partial_{\dot{\boldsymbol{F}}} \boldsymbol{P}^{\text{vis}} \right)_n^- \Big) : \partial_{\boldsymbol{X}} \underline{\boldsymbol{N}}_{\text{el}}^{\text{trans}} \Big] dV. \tag{4.69}$$

With the abbreviation

$$\underline{\underline{K}}_r = \Delta t \left(\frac{\underline{\underline{M}}_r}{\Delta t^2} + \alpha(1-\alpha) \underline{\underline{K}} + \underline{\underline{D}} \right), \tag{4.70}$$

the linearised system is then given by

$$\underline{\underline{K}}_r \odot \Delta \underline{r}_{n+1} = \underline{F}_r(\underline{r}_{n+1}) \tag{4.71}$$

for given $\underline{r}_{n-1}$ and $\underline{r}_n$, where $\Delta \underline{r}_{n+1}$ is the incremental update of the configuration. A Newton-Raphson scheme can be used with Equation (4.71) in order to solve for the unknown quantities $\underline{r}_{n+1}$ for each time step iteratively. Note that in contrast to $\underline{\underline{M}}_r$ and $\underline{\underline{D}}$, only $\underline{\underline{K}}$ has entries being different from zero for electrical degrees of freedom. Therefore, the total matrix of the left hand side of Equation (4.71) becomes singular and hence not invertible for $\alpha \to 0$ and $\alpha \to 1$.

Explicit solver Regarding Equation (4.61), $\alpha = 0$ or $\alpha = 1$ implies that $\underline{R}_{\boldsymbol{F}} = \underline{R}_{\boldsymbol{F}}(\underline{r}_n)$ and $\underline{R}_{\boldsymbol{E}} = \underline{R}_{\boldsymbol{E}}(\underline{r}_n)$. If additionally damping is either not present in the model ($\boldsymbol{P}^{\text{vis}} = 0$), or $\underline{R}_D$ is linear in $\underline{r}_{n+1}$, then Equation (4.61) can be solved explicitly for the unknown configuration $\underline{r}_{n+1}$. Note that $\ddot{\underline{r}}_d$ is always linear in $\underline{r}_{n+1}$. Because electrical degrees of freedom have no entry in the mass matrix $\underline{\underline{M}}_r$, the matrix is singular and can not be inverted directly. If $\underline{r}$ is split into mechanical degrees of freedom $\underline{r}^{\boldsymbol{F}}$ and electrical degrees of freedom $\underline{r}^{\boldsymbol{E}}$ such that

$$\underline{r} = \begin{pmatrix} \underline{r}^{\boldsymbol{F}} \\ \underline{r}^{\boldsymbol{E}} \end{pmatrix}, \tag{4.72}$$

the mass matrix can be written as

$$\underline{\underline{M}}_r = \begin{pmatrix} \underline{\underline{M}}_{\boldsymbol{F}} & \underline{\underline{0}} \\ \underline{\underline{0}} & \underline{\underline{0}} \end{pmatrix}. \tag{4.73}$$

Assuming that no damping is present and $\alpha = 0$, Equation (4.61) can then be solved in two steps

1. $\underline{r}_{n+1}^{\boldsymbol{F}} = \Delta t^2 \underline{\underline{M}}_{\boldsymbol{F}}^{-1} \odot \underline{R}_{\boldsymbol{F}}^{\text{all}} + 2\underline{r}_n^{\boldsymbol{F}} - \underline{r}_{n-1}^{\boldsymbol{F}}$ and

2. $\underline{r}^{\boldsymbol{E}}_{n+1}:\ \underline{R}^{\mathrm{all}}_{\boldsymbol{E}}(\underline{r}_{n+1}) = 0,$

where

$$\underline{R}^{\mathrm{all}} = -\underline{R}_{\boldsymbol{F}} + \underline{R}_{\boldsymbol{E}} + \bar{\underline{R}}_{\boldsymbol{T}} + \bar{\underline{R}}_{\boldsymbol{b}} - \bar{\underline{R}}_{Q} = \begin{pmatrix} \underline{R}^{\mathrm{all}}_{\boldsymbol{F}} \\ \underline{R}^{\mathrm{all}}_{\boldsymbol{E}} \end{pmatrix}. \tag{4.74}$$

From Equation (4.52) it can be seen that $\underline{R}_{\boldsymbol{E}}$ is linear in $\partial_{\boldsymbol{E}}\Omega$. For the material model chosen in this work (see Section 4.2.3), $\partial_{\boldsymbol{E}}\Omega$ is linear in $\boldsymbol{E}$ and hence $\underline{r}_{\boldsymbol{E}}$, such that the second step of the explicit integration scheme can indeed be solved explicitly.

Remark Applying the splitting technique (4.72) to Equation (4.61) and linearising the problem for arbitrary α and damping, the following form is obtained for the second step calculating $\underline{r}^{\boldsymbol{E}}_{n+1}$

$$\Delta\underline{r}^{\boldsymbol{E}}_{n+1} = \underline{\underline{K}}_{\boldsymbol{EE}} \odot \left(\frac{\underline{F}_{\boldsymbol{E}}}{\Delta t\, \alpha(1-\alpha)} - \underline{\underline{K}}_{\boldsymbol{EF}} \odot \Delta\underline{r}^{\boldsymbol{F}}_{n+1} \right) \tag{4.75}$$

for given $\Delta\underline{r}^{\boldsymbol{F}}_{n+1}$ and

$$\underline{\underline{K}} = \begin{pmatrix} \underline{\underline{K}}_{\boldsymbol{FF}} & \underline{\underline{K}}_{\boldsymbol{FE}} \\ \underline{\underline{K}}_{\boldsymbol{EF}} & \underline{\underline{K}}_{\boldsymbol{EE}} \end{pmatrix}. \tag{4.76}$$

From Equation (4.75) it is clear that $\lim\limits_{\alpha\to 0} \Delta\underline{r}^{\boldsymbol{E}}_{n+1} = \infty$ and $\lim\limits_{\alpha\to 1} \Delta\underline{r}^{\boldsymbol{E}}_{n+1} = \infty$. This is because there is no electrical inertia in the model. As a result, the general problem with arbitrary α can not be solved. Therefore, a value of $\alpha = 0.5$ is used for the numerical implementation in this work.

Static solver In order to obtain an initial guess about the behaviour of the dielectric actuator for a given voltage, the steady state can be obtained by using a static solver. Starting from Equation (4.61), the static state

$$\underline{r} = \underline{r}_{n-1} = \underline{r}_{n} = \underline{r}_{n+1} \tag{4.77}$$

is introduced, $\boldsymbol{P}^{\mathrm{vis}} = 0$ and Equation (4.61) reduces to

$$\underline{F}_{\mathrm{static}} = \underline{R}_{\boldsymbol{F}} + \underline{R}_{\boldsymbol{E}} + \bar{\underline{R}}_{\boldsymbol{T}} + \bar{\underline{R}}_{\boldsymbol{b}} - \bar{\underline{R}}_{Q} = 0. \tag{4.78}$$

Now, $\underline{R}_{\boldsymbol{F}} = \underline{R}_{\boldsymbol{F}}(\underline{r})$ and $\underline{R}_{\boldsymbol{E}} = \underline{R}_{\boldsymbol{E}}(\underline{r})$. Linearising the static problem in $\underline{r}$, the following system is obtained

$$\underline{\underline{K}} \odot \Delta\underline{r} = \underline{F}_{\mathrm{static}}(\underline{r}), \tag{4.79}$$

where $\Delta\underline{r}$ is the incremental steady state update. This Equation can be used with a Newton-Raphson scheme in order to obtain a static solution, as shown in [Vu07b]. For large load steps, a damped Newton scheme, respectively, load incrementation is necessary.

4.3.3 Numerical Implementation

The integration schemes discussed in the previous section are implemented as C++ code using the library deal.II [Bang07]. Hexahedral elements with linear shape functions are used for the spatial discretisation of translational as well as electrical degrees of freedom. Eight-point Gauss quadrature is used to solve the spatial integrals. Block sparse matrices allow for minimum memory requirements. Thread based parallelisation using work streams [Bang07] splits the computation of local contributions and the assembly of global quantities into independent processes, resulting in a very efficient code.

Hyperelastic material models are implemented analytically including their first derivatives with respect to the deformation gradient $\boldsymbol{F}$ and the electric field $\boldsymbol{E}$. Other derivatives that are required for the evaluation of the linearised finite element cell matrices are obtained via automatic differentiation using the C++ library Sacado that is part of the Trilinos project [Hero05].

Most of the quantities being present when simulating dielectric elastomers differ several orders of magnitude from standard SI-units. For better condition numbers, an alternative unit system is chosen. The base units are given as follows: length in mm, mass in g, time in ms and current in A. The relevant derived units are then given by: work in mJ, acceleration in $^{\mathrm{mm}}/_{\mathrm{ms}^2}$, density in $^{\mathrm{g}}/_{\mathrm{mm}^3}$, stress in MPa, force in N, permittivity in $^{\mathrm{F}}/_{\mathrm{m}}$, electric field strength in $^{\mathrm{V}}/_{\mathrm{mm}}$, capacity in mF, charge in mC and voltage in V.

4.4 Numerical examples

The silicone used to build dielectric actuators within this project (Wacker Elastosil P 7670) is almost incompressible, therefore the bulk modulus is approximated with a large number of $\kappa = 1000\,\mathrm{MPa}$. Measurements show that the Young's modulus can be chosen as $E = 0.7\,\mathrm{MPa}$ [Pelr98]. From these two values, the mechanical parameters used in the material model become $\mu = 0.233\,\mathrm{MPa}$ for the shear modulus and $\lambda = 999.8\,\mathrm{MPa}$. The density is set to $\rho_0 = 1 \cdot 10^{-3}\,{}^{\mathrm{g}}/_{\mathrm{mm}^3}$.

Next, the electrical parameter c_2 is chosen such that an elastic capacitor with an electrode distance of $10\,\mu\mathrm{m}$ shows about $20\,\%$ contraction when it is charged with a supply voltage of $100\,\mathrm{V}$. After testing different parameter values, $c_2 = 1 \cdot 10^{-9}\,{}^{\mathrm{N}}/_{\mathrm{V}^2}$ is used for further simulations. Note that the parameter c_1 does not affect the contraction, but only the amount of charge

necessary for maintaining a certain voltage. Using the well known formula for the capacity of a rigid plate capacitor with area a, plate distance $\hat{z}$ and relative permittivity ε_r

$$C = \varepsilon_0 \varepsilon_r \frac{a}{\hat{z}}, \tag{4.80}$$

parameter $c_1 = 5 \cdot 10^{-8}\,\mathrm{N/V^2}$ is chosen such that the amount of charge necessary to maintain the applied voltage corresponds to the relative permittivity $\varepsilon_r \approx 3$ for the used silicone.

The following examples illustrate the capabilities of the derived simulation framework for dielectric elastomers. First, the effect of the viscoelastic damping model on the transient response of an actuated dielectric elastomer is investigated. Then, a scaling benchmark gives a rough indication of the computational effort required to solve electromechanically coupled problems. Finally, a small-scale simulation illustrates the microscopic surface deformation of a stacked actuator and a large-scale simulation of a long stacked actuator demonstrates the macroscopic contraction and blocked forces.

4.4.1 Damping parameter influence

The first example geometry is a cube with an edge length of 2 mm, having its centre in the origin of the global coordinate system. The cube is uniformly split into 512 hexahedral elements, resulting in 729 nodes with a total of 2916 degrees of freedom. Essential boundary conditions are applied as follows: Symmetry requirements are applied to three faces of the cube. Translation along the x-axis is fixed to zero for all nodes located on the (y-z)-plane at $x = -1\,\mathrm{mm}$. Translation along the y-axis is fixed to zero for all nodes located on the (x-z)-plane at $y = -1\,\mathrm{mm}$. Translation along the z-axis is fixed to zero for all nodes located on the (x-y)-plane at $z = -1\,\mathrm{mm}$. The electric potential at the bottom face ((x-z)-plane at $y = -1\,\mathrm{mm}$) is fixed to zero. The electric potential of the left half of the top surface ((x-z)-plane at $y = 1\,\mathrm{mm}$ for $x < 0$) is fixed to 20 kV for all t.

Initialising ϕ with zero at all nodes for which no essential electric condition is specified, results in very large electric field intensities between nodes where electric potentials are specified and their close neighbours that are initialised with zero. These initial electric fields lead to large electric stresses during the first time step that cause the geometry to oscillate. To avoid these effects, in a first step, the purely electrical problem is solved for the given boundary conditions by fixing all translational degrees of freedom. The obtained state, to be observed in Figure 4.1, is then used as the initial condition for subsequent

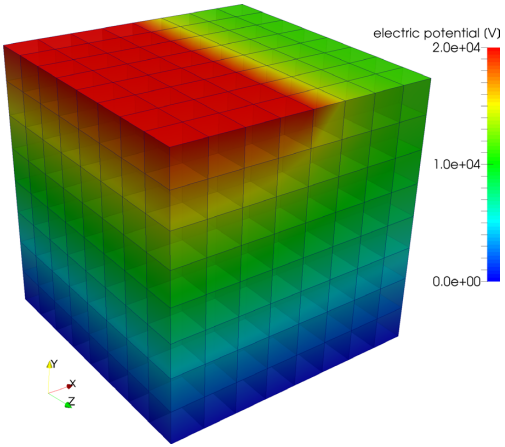

Figure 4.1: Cube for numerical examples with orientation of coordinate axes, electrical boundary conditions and resulting potential distribution.

time integration steps. As the electric field is considered quasi-static, this allows for a consistent initial electric field distribution.

500 time steps with a time step size of $\Delta t = 1 \cdot 10^{-3}$ ms are simulated for the given boundary conditions, resulting in a total simulation time of 0.5 ms. The damping parameter η is varied in a range from 0 to 0.1 $\mathrm{g/ms\,mm}$. Two quantities are evaluated. The height of the cube is defined as the distance between material points $(-1\,\mathrm{mm}, -1\,\mathrm{mm}, 0\,\mathrm{mm})$ and $(-1\,\mathrm{mm}, 1\,\mathrm{mm}, 0\,\mathrm{mm})$, projected on the y-axis. The total energy is the sum of the potential energy and the kinetic energy. The potential energy is given by Equation (3.36) and can be evaluated directly at time t_n. In contrast to the direct evaluation of the potential energy, the kinetic energy is obtained by first evaluating the discrete conjugate momentum using Equation (4.64) or (4.65). Then, all entries of $\underline{p}_{r,n}$ that are associated with essential boundary conditions are set to zero. Finally, the kinetic energy is obtained by

$$T_n = \frac{1}{2} \underline{p}^{\boldsymbol{F}}_{r,n} \cdot \underline{\underline{M}}^{-1}_{\boldsymbol{F}} \cdot \underline{p}^{\boldsymbol{F}}_{r,n}, \tag{4.81}$$

where $\underline{p}^{\boldsymbol{F}}_{r,n}$ is the discrete conjugate momentum of translational degrees of freedom. Note that the mass matrix (4.73) has no entries for electrical degrees of freedom and can not be inverted in total as in Equation (3.37).

The simulation results can be observed in Figure 4.2. For zero damping, high

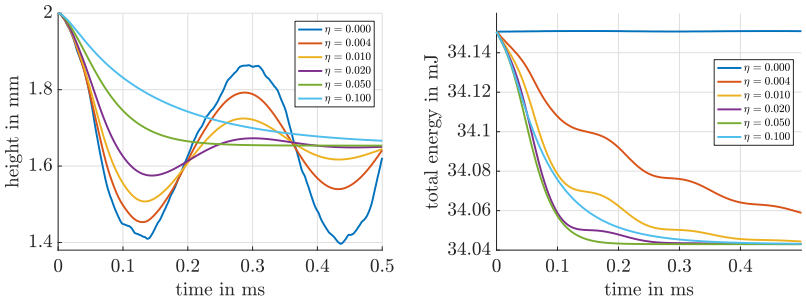

(a) Height. (b) Total energy.

Figure 4.2: Transient response of a dielectric elastomer cube for different damping parameters η.

frequency oscillations are observed (Figure 4.2a). These frequencies are fully damped for small damping values, compare $\eta = .004\,\mathrm{g/ms\,mm}$. Further increase of the damping parameter results in less overall oscillations. For the critical damping value $\eta = .05\,\mathrm{g/ms\,mm}$, overshooting has vanished. If the damping intensity is further increased, the time until the simulation reaches its steady state rises.[1] As all time quantities are of very small order, it is assumed that damping plays a major role in the simulation of dielectric actuators and dominates other dynamic effects.

The energy plot in Figure 4.2b confirms the good energy behaviour of the structure preserving integration scheme. For zero damping, the total energy shows minor oscillations, but is not decreasing or increasing overall. Also note that for the critical damping value $\eta = .05\,\mathrm{g/ms\,mm}$, the energy decrease is the quickest.

4.4.2 Scaling benchmark

The same geometry and boundary conditions as described in the previous example (Section 4.4.1) are used to benchmark computational costs for different numbers of elements. The results serve as a cost estimate for future simulations. In the first simulation run, the cube is represented by eight elements. Then, all elements are split into eight sub-elements, resulting in a total of eight times the elements of the previous discretisation. This procedure is repeated several

[1] see video of simulation: http://dx.doi.org/10.1016/j.cma.2015.10.017

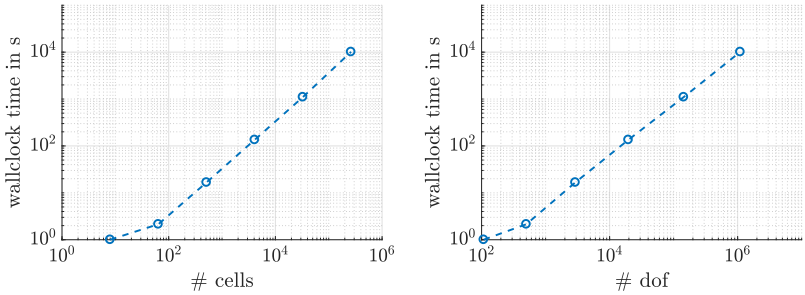

(a) Versus number of finite element cells. (b) Versus number of degrees of freedom.

Figure 4.3: Computational cost for solving the electrodynamically coupled problem.

times. In each simulation run, ten time steps are evaluated with a time step size of $\Delta t = 1 \cdot 10^{-4}$ ms. The damping parameter is set to the large value $\eta = .4\,\mathrm{g/ms\,mm}$, such that each time step requires only two Newton iterations for convergence. The simulation is run on single socket compute nodes with Intel Xeon E3-1240 v3 processors (4-core "Haswell", 3.4 GHz, 8 GB RAM).

As seen in Figures 4.3, the computational cost scales quite nicely with the number of elements, respectively, the number of degrees of freedom. For systems with more than about 100 elements (or 1000 degrees of freedom), the overhead of initialising the system becomes negligible and the total simulation time, called "wall clock time", grows linearly with the number of elements. Note that a large system with 262 144 elements and 1 098 500 degrees of freedom takes only about 2.81 h to be simulated, with the 8 GB of RAM of the compute node still being sufficient.

4.4.3 Real geometry analysis

A stacked dielectric actuator consists of an array of single actuator elements in a pile-up configuration [Kova09]. The stacked actuator being developed within the project Bionicum is expected to meet the following criteria: cylinder shape, diameter of 1 cm, electrode distance of 10 μm and electrode thickness of 2 μm. These values serve as a basis to create a mesh representing three single stacked actuator elements. Each electrode layer is discretised with five finite element layers, each finite element layer having a height of $4 \cdot 10^{-4}$ mm. Each insulating silicone layer is discretised with 25 finite element layers as described

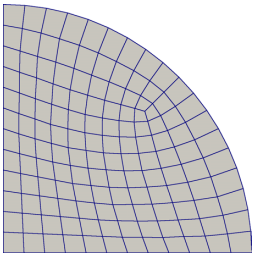

Figure 4.4: Finite element mesh of dielectric actuator with real geometry properties.

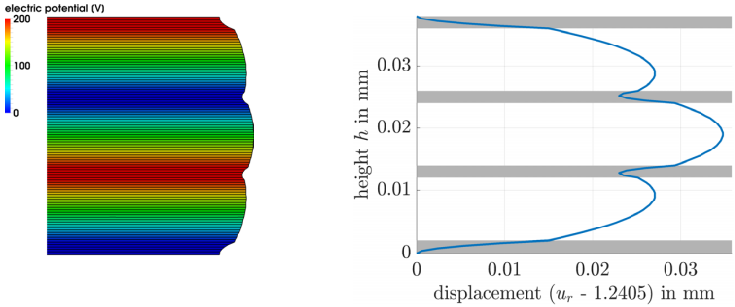

(a) The deformation in horizontal direction is scaled with a factor of 100.

(b) Electrodes are coloured grey.

Figure 4.5: Deformed surface of actuator cells with real geometry.

above. A total of four electrodes and three separating silicone layers results in 95 finite element layers. For symmetry reasons, only a quarter of the cross section area is modelled. Figure 4.4 shows the finite element mesh layer. This layer is extruded orthogonally to reach the height of $4 \cdot 10^{-4}$ mm. The total model consists of 12,825 finite elements and 60,288 degrees of freedom.

Mechanical boundary conditions are applied to meet the symmetry requirements. Moreover, the bottom layer is fixed in height direction. The electrodes are alternately charged with 0 V, respectively, 200 V. The deformed state is evaluated using the static solver (4.79). Figure 4.5 shows the simulation results. It can be observed that the insulating silicone layers contract in length direction and expand in radial direction due to incompressibility. This expansion, however, interferes with the passive behaviour of the electrode layers that do not contract and hence not expand actively. As a result, a waveform in height

direction can be observed on the surface of the stacked actuator. The electrode layers have smaller diameter than the insulating silicone layers. This effect, however, is very small and becomes visible only if the visualised diameter is scaled with a factor of about 100, as shown in Figure 4.5a.

4.4.4 Reduced layer muscle model

A stacked dielectric actuator of the geometry introduced in Section 4.4.3 and a length of $l_0 = 100\,\mathrm{mm}$ consists of thousands of single DEA cells. Discretising the whole muscle with a high resolution finite element mesh as in Section 4.4.3 results in almost 200 000 000 degrees of freedom—a system too large for shared memory computations. A model reduction approach allows to reduce the total number of degrees of freedom while still providing accurate results. First, a whole stack of DEA cells is replaced by a single finite element. Then, the Dirichlet conditions for the electric potential are modified such that they lead to similar electric field intensities as the original model [Schl14a]. The muscle is discretised with 512 finite elements and 3300 degrees of freedom. It consists of $n_{\mathrm{lay}} = 32$ finite element layers in length direction. Zero electric potential and the replacement voltage

$$U_{\mathrm{repl}} = U_{\mathrm{orig}} \frac{l_0}{n_{\mathrm{lay}} \hat{z}} \tag{4.82}$$

with the applied voltage U_{orig} and electrode distance $\hat{z}$ of the original model are applied alternately at the node layers.

Two different sets of mechanical boundary conditions are considered. At first, the bottom muscle face as well as the top muscle face are fixed for all translations such that the muscle is undeformed. The steady-state is simulated using the static solver for voltages ranging between 0 and 200 V. In Figure 4.6a, the reaction forces are illustrated with arrows. Note that the electric potential that is actually applied is much larger than 200 V. This results from the replacement voltage given in Equation (4.82). In Figure 4.6b, the quadratic interrelation between the applied voltage and the resulting force can be observed, which is consistent to Equation (1.1).

When the top muscle face is released, the muscle contracts. Figure 4.7 illustrates the deformed steady state for voltages ranging between 0 and 200 V. The length of the muscle is measured between the centre of the top face and the centre of the bottom face. With decreasing total length, the cross section area increases, as the material is incompressible. However, because the bottom

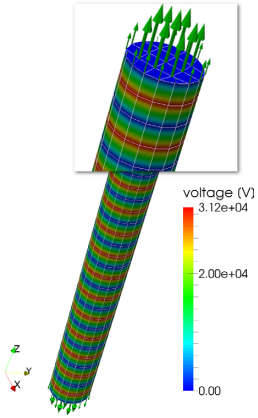

(a) Visualisation of reaction forces.

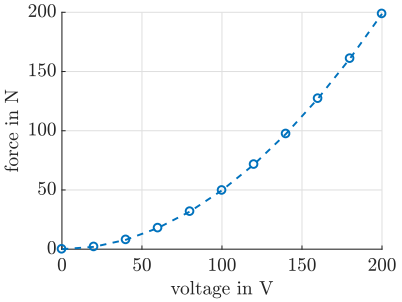

(b) Total reaction force versus applied voltage.

Figure 4.6: Resulting total blocked force of a reduced dielectric actuator model for different voltages.

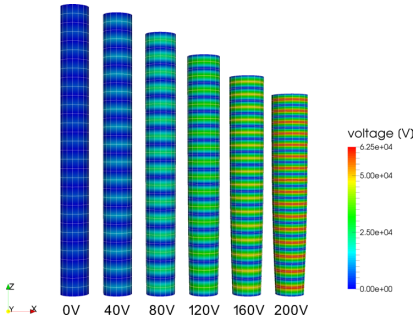

(a) Deformation state.

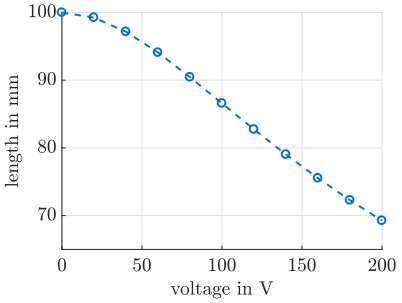

(b) Contracted length versus applied voltage.

Figure 4.7: Contraction of a reduced dielectric actuator model for different voltages.

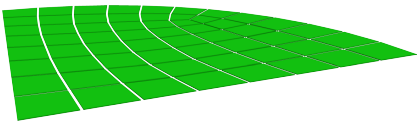

Figure 4.8: Base mesh layer for the performance analysis of the layer reduction method.

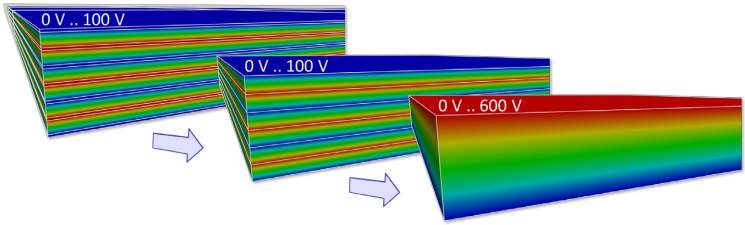

Figure 4.9: Step-by-step layer reduction process. The colour visualises the electric potential distribution.

face is mechanically fixed, the expansion of the cross section area is locally inhibited.

4.4.5 Performance analysis of the reduced layer muscle model

The effect of the reduction method presented in the previous example on the accuracy and computational cost is further investigated. This example is mainly based on [Schl14a]. The test model consists of a circular actuator with a diameter of 1 cm, an electrode distance of 10 µm and an electrode thickness of 2 µm. For symmetry reasons, the finite element base mesh layer represents a quarter of the cross section area of the stacked actuator and consists of 60 finite elements, as illustrated in Figure 4.8.

The full reference model ("full") that is illustrated in Figure 4.9 on the left hand side consists of six stacked dielectric actuator cells and in 13 finite element mesh layers with a total of $60 \cdot 13 = 780$ elements. All electrode layers as well as all insulating silicone layers in between consist of only one finite element layer. The electrodes have a finite volume that acts as "passive" material during contraction and the electrodes are alternately charged with 0 V and 100 V.

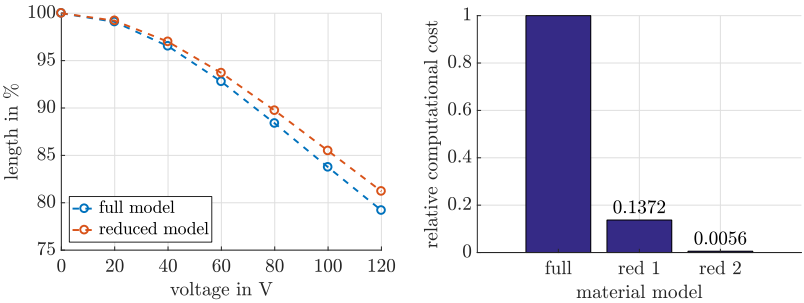

(a) Length versus applied voltage.

(b) Computational cost.

Figure 4.10: Accuracy and computational cost for different model layer reduction states.

In a first reduction step ("red 1"), the finite volume of the electrode layers is replaced by infinitely thin finite element node layers while keeping the total volume of the actuator constant (Centre image in Figure 4.9). This step is accompanied by two effects on the simulation accuracy that partially cancel out each other. On the one hand, the "passive" material volume of the electrodes is moved to the silicone layers, increasing the volume of "active" material. This increases the total contractive force. On the other hand, the electrode distance is increased, resulting in a smaller electric field. This decreases the total contractive force. The total number of elements is reduced to $60 \cdot 6 = 360$.

In a second reduction step (Figure 4.9 on the right hand side, "red 2"), all electrode layers within the material are removed and replaced with consistent boundary conditions at the top and at the bottom that lead to the same electric field intensity. In this case, the applied voltage increases by a factor of six to 600 V to compensate for the five removed electrode layers. This last step mainly decreases the computational cost as the total number of elements is reduced to 60 while there is no influence on the contraction behaviour.

Figure 4.10 illustrates the effect of the layer reduction on the accuracy of the simulation results regarding contracted actuator length and computational cost. Note that the electromechanically coupled static solver used for this example is based on a non-optimised MATLAB implementation and does not make use of the optimised C++ finite element library deal.II. Figure 4.10a compares the contracted lengths of the actuator for different applied voltages and the full and layer reduced model. Note that the intermediate reduction ("red 1") provides identical lengths to the full reduction and is omitted in this

plot. It can be seen that the differences are relatively small with a maximum deviation of approximately 2 % of the total actuator length for full contraction. Accepting this loss of accuracy, the simulation time can be reduced by more than 99 % as visualised in Figure 4.10b.

5 Flexible multibody dynamics – the actuated system

In this chapter, a three-dimensional electro-mechanically coupled finite element model for dielectric elastomers is utilised to actuate multibody systems. This setting allows exploring the complex behaviour of humanoid robots that are driven by artificial muscles instead of electrical drives. Some example configurations are presented in Figure 5.1. The complex dynamic behaviour of such soft robots requires sophisticated control strategies that are based on reliable mathematical models.

The coupling between the finite element muscle model and the rigid bodies is formulated at configuration level, where Lagrange multipliers account for constraint forces, leading to differential algebraic equations of index-3 [Leye08a]. A well-chosen set of redundant configuration variables for the multibody system avoids any rotational degrees of freedom and leads to linear coupling constraints. As a result, the coupling between the artificial muscles and the multibody system can be formulated in a very modular way that allows for easy future extension. The applied structure preserving time integration scheme provides excellent long time energy behaviour. In addition, the index-3 system is solved directly with numerical accuracy, avoiding index reduction approximations. This chapter is to a great extend based on [Schl16b].

In Section 5.1, the redundant multibody system formulation is introduced. The

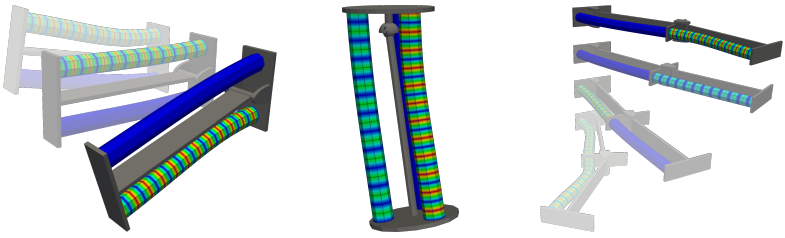

(a) Revolute joint. (b) Universal joint. (c) Serial revolute joints.

Figure 5.1: Flexible multibody systems. Finite element discretised artificial muscles actuate kinematic structures.

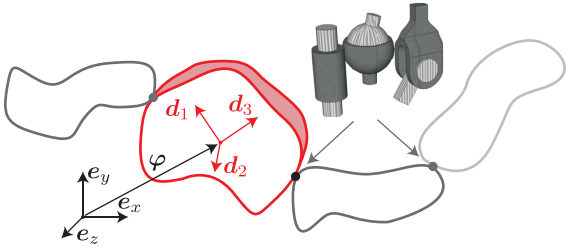

Figure 5.2: Kinematic chain with director coordinates that span a local Euclidean coordinate system.

system is actuated via the finite element artificial muscle model from Chapter 4. The corresponding coupling equations and the block structure of the coupled system are presented in Section 5.2. In Section 5.3, the evaluation of the kinetic energy of the coupled system is explained. Finally, in Section 5.4, numerical examples illustrate the application of the derived simulation framework to simulate artificial muscle actuated systems. Note that the multibody system configuration is denoted with $\underline{s}$ (instead of $\underline{q}$) throughout this chapter for distinction from finite element degrees of freedom $\underline{r}$.

5.1 Multibody system formulation

The multibody system consists of a chain of rigid bodies that are connected by joints. The rigid bodies are numbered by $j \in \{1, \dots, J\}$ and the joints are modelled by constraining the relative motion of neighbouring bodies. The configuration

$$\underline{s}^j(t) = \begin{pmatrix} \boldsymbol{\varphi}^j(t) & \boldsymbol{d}_1^j(t) & \boldsymbol{d}_2^j(t) & \boldsymbol{d}_3^j(t) \end{pmatrix}^T \quad \in \mathbb{R}^{12} \tag{5.1}$$

of each rigid body j is characterised by twelve quantities, namely three for the translational position of the body's centre of mass $\boldsymbol{\varphi}^j \in \mathbb{R}^3$ and three quantities for each director $\boldsymbol{d}_i^j \in \mathbb{R}^3,\ i \in \{1, 2, 3\}$ that together span a local Euclidean coordinate system, as illustrated in Figure 5.2. Note that the expression in Equation (5.1) is simplified for convenience. The transpose operator is omitted for the individual contributions that together compose the one-dimensional array $\underline{s}^j$. This notation is used throughout this work. The directors can be understood as the columns of a rotation matrix that accounts for the orientation of the body. The total configuration

$$\underline{s} = \begin{pmatrix} \underline{s}^1 & \underline{s}^2 & \dots & \underline{s}^J \end{pmatrix}^T \quad \in \mathbb{R}^{12J} \tag{5.2}$$

collects the configurations of all rigid bodies.

With this formulation, the kinetic energy is given by

$$T_s(\underline{\dot{s}}) = \frac{1}{2}\underline{\dot{s}} \cdot \underline{\underline{M}}_s \cdot \underline{\dot{s}}, \tag{5.3}$$

with the constant total diagonal mass matrix

$$\underline{\underline{M}}_s = \begin{pmatrix} \underline{\underline{M}}^1 & \underline{\underline{0}} & \dots & \underline{\underline{0}} \\ \underline{\underline{0}} & \underline{\underline{M}}^2 & \dots & \underline{\underline{0}} \\ \vdots & \vdots & \ddots & \vdots \\ \underline{\underline{0}} & \underline{\underline{0}} & \dots & \underline{\underline{M}}^J \end{pmatrix}, \tag{5.4}$$

where $\underline{\underline{M}}^j$ is the single rigid body mass matrix. Assuming that the directors coincide with the principle axis of inertia of the rigid body, the corresponding mass matrix is given by

$$\underline{\underline{M}}^j = \begin{pmatrix} m^j\mathbf{1} & \mathbf{0} & \mathbf{0} & \mathbf{0} \\ \mathbf{0} & \Theta_1\mathbf{1} & \mathbf{0} & \mathbf{0} \\ \mathbf{0} & \mathbf{0} & \Theta_2\mathbf{1} & \mathbf{0} \\ \mathbf{0} & \mathbf{0} & \mathbf{0} & \Theta_3\mathbf{1} \end{pmatrix} \quad \in \mathbb{R}^{12\times 12}, \tag{5.5}$$

where m^j is the rigid body mass and

$$\boldsymbol{\Theta} = \begin{pmatrix} \Theta_1 & 0 & 0 \\ 0 & \Theta_2 & 0 \\ 0 & 0 & \Theta_3 \end{pmatrix} \quad \in \mathbb{R}^{3\times 3} \tag{5.6}$$

is the Euler tensor [Bets06]. The Euler tensor $\boldsymbol{\Theta}$ is related to the inertia tensor $\boldsymbol{J}$ by

$$\boldsymbol{\Theta} = \frac{1}{2}\left(\boldsymbol{J} : \mathbf{1}\right)\mathbf{1} - \boldsymbol{J}. \tag{5.7}$$

The potential energy is given by

$$\Pi_s(\underline{s}) = -\sum_j m^j \boldsymbol{\varphi}^j \cdot \boldsymbol{g}_{\mathrm{v}} \tag{5.8}$$

with the constant gravitation vector $\boldsymbol{g}_{\mathrm{v}}$.

Each rigid body has six degrees of freedom in a three-dimensional space, namely three translational and three rotational. As the director formulation assigns

twelve configuration variables to each rigid body, six additional constraints are required. The so called internal constraints

$$\underline{h}^j_{\text{int}}(\underline{s}^j) = \begin{pmatrix} {}^1\!/_2 \left(\boldsymbol{d}^j_1 \cdot \boldsymbol{d}^j_1 - 1\right) \\ {}^1\!/_2 \left(\boldsymbol{d}^j_2 \cdot \boldsymbol{d}^j_2 - 1\right) \\ {}^1\!/_2 \left(\boldsymbol{d}^j_3 \cdot \boldsymbol{d}^j_3 - 1\right) \\ \boldsymbol{d}^j_1 \cdot \boldsymbol{d}^j_2 \\ \boldsymbol{d}^j_1 \cdot \boldsymbol{d}^j_3 \\ \boldsymbol{d}^j_2 \cdot \boldsymbol{d}^j_3 \end{pmatrix} = 0 \quad \in \mathbb{R}^6 \tag{5.9}$$

for each rigid body j ensure orthonormality of the directors [Bets06]. From a physical point of view, the internal constraints avoid scaling and shearing and hence account for rigidity. The constraint array

$$\underline{h}_{\text{int}}(\underline{s}) = \begin{pmatrix} \underline{h}^1_{\text{int}} & \underline{h}^2_{\text{int}} & \dots & \underline{h}^J_{\text{int}} \end{pmatrix}^T \quad \in \mathbb{R}^{6J} \tag{5.10}$$

collects the internal constraints from all rigid bodies.

Additional joint constraints $\underline{h}_{\text{joint}}(\underline{s})$ restrict the motion of two neighbouring bodies relative to each other. The constraints for various types of joints like spherical, cylindrical, revolute, prismatic and planar can be found in [Bets06]. All n_h multibody system constraints are summarised in the array

$$\underline{h}(\underline{s}) = \begin{pmatrix} \underline{h}_{\text{int}} & \underline{h}_{\text{joint}} \end{pmatrix}^T \quad \in \mathbb{R}^{n_h} \tag{5.11}$$

and for the multibody system with redundant coordinates, the constrained discrete Euler-Lagrange-Equations (3.17) read

$$\frac{\partial L_{s,d}(\underline{q}_n, \underline{s}_{n+1})}{\partial \underline{s}_n} + \frac{\partial L_{s,d}(\underline{s}_{n-1}, \underline{s}_n)}{\partial \underline{s}_n} - \underline{\underline{H}}^T_d(\underline{s}_n) \cdot \underline{\lambda}_{s,n} = \underline{0} \tag{5.12a}$$

$$\underline{h}(\underline{s}_{n+1}) = \underline{0}. \tag{5.12b}$$

The multibody system Lagrangian is given by

$$L_s(\underline{s}, \dot{\underline{s}}) = T_s(\dot{\underline{s}}) - \Pi_s(\underline{s}), \tag{5.13}$$

the Lagrange multipliers $\lambda_{s,n}$ account for the rigid body constraints $\underline{h}$ and

$$\underline{\underline{H}}_d(\underline{s}_n) = \Delta t \, \frac{\partial \underline{h}(\underline{s}_n)}{\partial \underline{s}_n} \tag{5.14}$$

is the discrete constraint Jacobian. Note that for consistency with the discretisation of the finite element Lagrangian (compare to Section 4.3.2), the parameter α of the general midpoint quadrature (3.4) is chosen to be $\alpha = 0.5$ for the multibody system as well. For the sake of simplicity, specific non-conservative contributions for the multibody system (e.g. friction in joints) are

not introduced here, however they can be considered following the procedure of Section 3.4.

In order to avoid ill-conditioned matrices that result from the introduced Lagrange multipliers $\underline{\lambda}_s$, a null space matrix is used to project the discrete equations of motion (5.12a) into the tangent space, where constraint fulfilling motion happens. Consequently, Lagrange multipliers need not be considered but can optionally be evaluated in post-processing [Leye08b].

Analogously to Section 3.3, the null space matrix here connects the multibody system velocities $\dot{\underline{s}}$ with minimal velocities $\dot{\underline{s}}^{\min}$ such that

$$\dot{\underline{s}} = \underline{\underline{T}}(\underline{s}) \cdot \dot{\underline{s}}^{\min}, \tag{5.15}$$

and the null space matrix now depends on the current configuration $\underline{s}$. Right multiplying the null space matrix to the constraint Jacobian returns zero, i.e.

$$\underline{\underline{H}}_d(\underline{s}_n) \cdot \underline{\underline{T}}(\underline{s}_n) = \underline{0}. \tag{5.16}$$

Left multiplying the transpose of the null space matrix $\underline{\underline{T}}^T$ to Equation (5.12a) leads to

$$\underline{\underline{T}}^T(\underline{s}_n) \cdot \left(\frac{\partial L_{s,d}(\underline{s}_n, \underline{s}_{n+1})}{\partial \underline{s}_n} + \frac{\partial L_{s,d}(\underline{s}_{n-1}, \underline{s}_n)}{\partial \underline{s}_n} \right) = \underline{0} \tag{5.17a}$$

$$\underline{h}(\underline{s}_{n+1}) = \underline{0}, \tag{5.17b}$$

where the dimension of Equation (5.17a) is reduced to the number of degrees of freedom [Bets06, Leye08b]. Equation (5.17a) is abbreviated by

$$\underline{F}_s(\underline{s}_{n-1}, \underline{s}_n, \underline{s}_{n+1}) = \underline{\underline{T}}^T(\underline{s}_n) \cdot \left(\frac{\partial L_{s,d}(\underline{s}_n, \underline{s}_{n+1})}{\partial \underline{s}_n} + \frac{\partial L_{s,d}(\underline{s}_{n-1}, \underline{s}_n)}{\partial \underline{s}_n} \right). \tag{5.18}$$

The non-linear integration scheme given by Equations (5.17) is linearised as

$$\begin{pmatrix} \underline{F}_s \\ \underline{h} \end{pmatrix} + \begin{pmatrix} \underline{\underline{K}}_s \\ \underline{\underline{H}} \end{pmatrix} \cdot \Delta \underline{s}_{n+1} = \underline{0}, \tag{5.19}$$

where $\Delta \underline{s}_{n+1}$ is the incremental configuration update of the multibody system, $\underline{\underline{H}}(\underline{s}) = {}^{\partial \underline{h}(\underline{s})}/_{\partial \underline{s}}$ the constraint Jacobian and

$$\underline{\underline{K}}_s(\underline{s}_n, \underline{s}_{n+1}) = \frac{\partial \underline{F}_s(\underline{s}_{n-1}, \underline{s}_n, \underline{s}_{n+1})}{\partial \underline{s}_{n+1}}, \tag{5.20}$$

such that the problem can be solved iteratively for $\underline{s}_{n+1}$ using a Newton-Raphson scheme.

5.2 Coupling between dielectric elastomer and multibody system

The coupling between the finite element muscle model and the multibody system is formulated at position level. Certain nodes on the surface of the finite element mesh are bound to specific points on the rigid bodies. For linear Lagrange finite element shape functions, node positions of the mesh directly correspond to translational degrees of freedom of the associated element. The configuration vector

$$\underline{q} = \begin{pmatrix} \underline{r} \\ \underline{s} \end{pmatrix} \tag{5.21}$$

contains all degrees of freedom of the coupled model. The kinetic and potential energies of the coupled system are given by

$$T(\dot{\underline{q}}) = T_r(\dot{\underline{r}}) + T_s(\dot{\underline{s}}) \tag{5.22}$$

and

$$\Pi(\underline{q}) = \Pi_r(\underline{r}) + \Pi_s(\underline{s}), \tag{5.23}$$

respectively. Without coupling constraints, the independent models can be solved simultaneously by evaluating

$$\begin{pmatrix} \underline{F}_r(\underline{r}_{n-1}, \underline{r}_n, \underline{r}_{n+1}) \\ \underline{F}_s(\underline{s}_{n-1}, \underline{s}_n, \underline{s}_{n+1}) \\ \underline{h}(\underline{s}_{n+1}) \end{pmatrix} = \underline{0}, \tag{5.24}$$

with the linearised form

$$\begin{pmatrix} \underline{F}_r \\ \underline{F}_s \\ \underline{h} \end{pmatrix} + \begin{pmatrix} \underline{\underline{K}}_r & \underline{\underline{0}} \\ \underline{\underline{0}} & \underline{\underline{K}}_s \\ \underline{\underline{0}} & \underline{\underline{H}} \end{pmatrix} \cdot \begin{pmatrix} \Delta\underline{r}_{n+1} \\ \Delta\underline{s}_{n+1} \end{pmatrix} = \underline{0}. \tag{5.25}$$

Note that for the sake of simplicity, from now on the use of the finite element contraction operator $\odot$ is omitted and replaced by the single contraction operator $(\cdot)$.

Fixing a single node $c \in \{1, \ldots, C\}$ of the finite element mesh to a rigid body j requires the constraints

$$\boldsymbol{g}_c(\underline{r}, \underline{s}) = \underbrace{\boldsymbol{x}^c}_{\text{muscle model}} \quad \underbrace{-\boldsymbol{\varphi}^j - \xi_1^c \boldsymbol{d}_1^j - \xi_2^c \boldsymbol{d}_2^j - \xi_3^c \boldsymbol{d}_3^j}_{\text{multibody system}} = \boldsymbol{0} \quad \in \mathbb{R}^3, \tag{5.26}$$

where $\boldsymbol{x}^c$ is the finite element node position and the constant parameters ξ_1^c, ξ_2^c and ξ_3^c describe the location of the finite element node in the local rigid

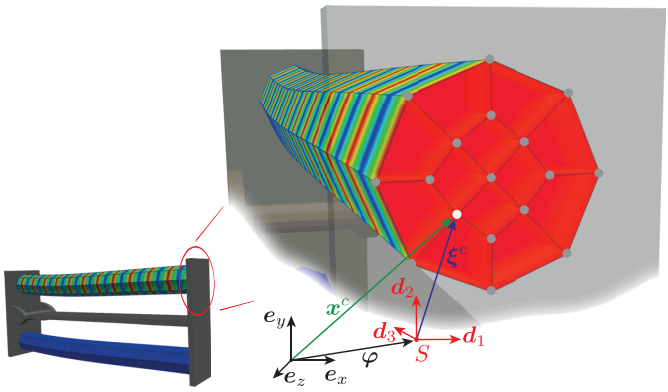

Figure 5.3: Coupling of multibody system with flexible artificial muscle at position level.

body coordinate system, as illustrated in Figure 5.3. Hence, a total of C vector valued node constraints results in $3C$ scalar constraints that account for the coupling between the artificial muscle and the multibody system. The constraints are summarised in the array

$$\underline{g}(\underline{r},\underline{s}) = \begin{pmatrix} \boldsymbol{g}_1(\underline{r},\underline{s}) & \boldsymbol{g}_2(\underline{r},\underline{s}) & \dots & \boldsymbol{g}_C(\underline{r},\underline{s}) \end{pmatrix}^T \in \mathbb{R}^{3C}. \tag{5.27}$$

The constraint Jacobian $\underline{\underline{G}}$ is separated such that

$$\underline{\underline{G}} = \begin{pmatrix} \underline{\underline{G}}_r & \underline{\underline{G}}_s \end{pmatrix} \tag{5.28}$$

with

$$\underline{\underline{G}}_r = \frac{\partial \underline{g}(\underline{r},\underline{s})}{\partial \underline{r}} \tag{5.29a}$$

$$\underline{\underline{G}}_s = \frac{\partial \underline{g}(\underline{r},\underline{s})}{\partial \underline{s}}, \tag{5.29b}$$

where $\underline{\underline{G}}_r$ accounts for the derivatives of the coupling constraints with respect to finite element degrees of freedom and $\underline{\underline{G}}_s$ accounts for the derivatives of the coupling constraints with respect to multibody system degrees of freedom. The discrete counterpart of the constraint Jacobian is obtained by $\underline{\underline{G}}_d = \Delta t\, \underline{\underline{G}}$, where $\underline{\underline{G}}_d$ is composed of $\underline{\underline{G}}_{r,d}$ and $\underline{\underline{G}}_{s,d}$. Note that the constraint Jacobian $\underline{\underline{G}}$ is constant as a result of the director formulation that leads to linear coupling

constraints. The finite element part of the constraint Jacobian has the form

$$\underline{\underline{G}}_r = \begin{pmatrix} \ddots & \vdots & \vdots & \vdots & \iddots \\ \dots & 1 & 0 & 0 & \dots \\ \dots & 0 & 1 & 0 & \dots \\ \dots & 0 & 0 & 1 & \dots \\ \iddots & \vdots & \vdots & \vdots & \ddots \end{pmatrix}. \tag{5.30}$$

For each row of $\underline{\underline{G}}_r$ (that corresponds to a single constraint) only one entry is one whereas all other entries are zero. The entry being different from zero corresponds to the global finite element degree of freedom that is constrained. The multibody part of the constraint Jacobian has the form

$$\underline{\underline{G}}_s = \begin{pmatrix} \ddots & \vdots & \vdots & \vdots & \vdots & \iddots \\ \dots & -\mathbf{1} & -\xi_1\mathbf{1} & -\xi_2\mathbf{1} & -\xi_3\mathbf{1} & \dots \\ \iddots & \vdots & \vdots & \vdots & \vdots & \ddots \end{pmatrix} \tag{5.31}$$

for the three spatial constraints of one finite element node being fixed on the rigid body.

Introducing the coupling constraints to the discrete Euler-Lagrange-Equations (3.17) yields the non-linear integration scheme

$$\begin{pmatrix} \underline{F}_r \\ \underline{F}_s \\ \underline{h} \\ \underline{0} \end{pmatrix} + \begin{pmatrix} -\underline{\underline{G}}_{r,d}^T \cdot \underline{\lambda} \\ -\underline{\underline{T}}^T \cdot \underline{\underline{G}}_{s,d}^T \cdot \underline{\lambda} \\ \underline{0} \\ \underline{g} \end{pmatrix} = \underline{0}, \tag{5.32}$$

where $\underline{F}_r$, $\underline{F}_s$ and $\underline{h}$ are given by Equations (4.62), (5.18) and (5.11), respectively. The linearised form reads

$$\begin{pmatrix} \underline{F}_r - \underline{\underline{G}}_{r,d}^T \cdot \underline{\lambda} \\ \underline{F}_s - \underline{\underline{T}}^T \cdot \underline{\underline{G}}_{s,d}^T \cdot \underline{\lambda} \\ \underline{h} \\ \underline{g} \end{pmatrix} + \begin{pmatrix} \underline{\underline{K}}_r & \underline{\underline{0}} & -\underline{\underline{G}}_{r,d}^T \\ \underline{\underline{0}} & \underline{\underline{K}}_s & -\underline{\underline{T}}^T \cdot \underline{\underline{G}}_{s,d}^T \\ \underline{\underline{0}} & \underline{\underline{H}} & \underline{\underline{0}} \\ \underline{\underline{G}}_r & \underline{\underline{G}}_s & \underline{\underline{0}} \end{pmatrix} \cdot \begin{pmatrix} \Delta\underline{r}_{n+1} \\ \Delta\underline{s}_{n+1} \\ \Delta\underline{\lambda}_n \end{pmatrix} = \underline{0}. \tag{5.33}$$

For each time step, the unknown configuration of the finite element model $\underline{r}_{n+1}$ and of the rigid body model $\underline{s}_{n+1}$ as well as the unknown Lagrange multipliers $\underline{\lambda}_n$ are obtained by solving Equations (5.33) iteratively with a Newton-Raphson scheme. Note that the non-linear system of coupled equations (5.32)

consists of the isolated contributions of the subsystems in the first term (compare to Equation (5.24)) where just another array containing the coupling constraints and their derivatives including the associated Lagrange multipliers is added in the second term. Hence, the linearised matrix given in Equation (5.33) also consists of mainly the isolated contributions of the subsystems (5.25). Here, just another row block as well as another column block containing constraint gradients is added.

5.3 Kinetic energy evaluation of the coupled system

The evaluation of the kinetic energy of the coupled system via the conjugate momentum (3.33) requires the Lagrange multipliers $\underline{\lambda}$ to be known. Whereas the Lagrange multipliers associated with the coupling constraints $\underline{g}$ are available, the Lagrange multipliers that belong to the rigid body constraints $\underline{h}$ are not present, because the integration scheme has been projected into the tangent space using the null space matrix $\underline{\underline{T}}$. The calculation of the Lagrange multipliers can be avoided by projecting the Legendre transform into a tangent space (Q-projection) as described below.

As only translational degrees of freedom contribute to the kinetic energy of the system, the new configuration

$$\hat{\underline{q}} = \begin{pmatrix} \underline{r}^{\boldsymbol{F}} \\ \underline{s} \end{pmatrix} \tag{5.34}$$

is introduced, where $\underline{r}^{\boldsymbol{F}}$ contains only finite element degrees of freedom that are associated with translational quantities (compare to Equation (4.72)). A global constraint Jacobian $\hat{\underline{\underline{G}}}(\hat{\underline{q}})$ accounts for all constraints in the system, both multibody system constraints $\underline{h}$ and coupling constraints $\underline{g}$, with respect to the translational configuration quantities $\hat{\underline{q}}$ such that

$$\hat{\underline{\underline{G}}} = \begin{pmatrix} \underline{\underline{0}} & \underline{\underline{H}} \\ \underline{\underline{G}}_r^{\boldsymbol{F}} & \underline{\underline{G}}_s \end{pmatrix}, \tag{5.35}$$

where $\underline{\underline{G}}_r^{\boldsymbol{F}}$ contains only entries from (5.29a) that are associated with translational degrees of freedom. Additionally, the global and invertible mass matrix

$$\hat{\underline{\underline{M}}}(\hat{\underline{q}}) = \begin{pmatrix} \underline{\underline{M}}_{\boldsymbol{F}} & \underline{\underline{0}} \\ \underline{\underline{0}} & \underline{\underline{M}}_s \end{pmatrix} \tag{5.36}$$

is introduced, where $\underline{\underline{M}}_{\boldsymbol{F}}$ is taken from Equation (4.73).

From these quantities, the projection matrix $\underline{\underline{Q}}(\hat{\underline{q}})$ (see [Leye08b]) is obtained as

$$\underline{\underline{Q}} = \underline{\underline{\tilde{1}}} - \underline{\underline{\hat{G}}}^T \cdot \left(\underline{\underline{\hat{G}}} \cdot \underline{\underline{\hat{M}}}^{-1} \cdot \underline{\underline{\hat{G}}}^T \right)^{-1} \cdot \underline{\underline{\hat{G}}} \cdot \underline{\underline{\hat{M}}}^{-1}, \tag{5.37}$$

where all quantities are evaluated at $\hat{\underline{q}}$ and $\underline{\underline{\tilde{1}}}$ is the identity matrix of appropriate size. Based on $\underline{\underline{Q}}$, the projected discrete Legendre transform at time t_n is given by

$${}^{Q}\hat{\underline{p}}_n^- = \underline{\underline{Q}}(\hat{\underline{q}}_n) \cdot \begin{pmatrix} \hat{\underline{p}}_{r,n}^- \\ -\frac{\partial L_{s,d}(\underline{s}_n, \underline{s}_{n+1})}{\partial \underline{s}_n} \end{pmatrix} \tag{5.38}$$

$${}^{Q}\hat{\underline{p}}_n^+ = \underline{\underline{Q}}(\hat{\underline{q}}_n) \cdot \begin{pmatrix} \hat{\underline{p}}_{r,n}^+ \\ \frac{\partial L_{s,d}(\underline{s}_{n-1}, \underline{s}_n)}{\partial \underline{s}_n} \end{pmatrix}, \tag{5.39}$$

where $\hat{\underline{p}}_{r,n}^-$ and $\hat{\underline{p}}_{r,n}^+$ are taken from (4.65) and (4.64), respectively, but only entries associated with translational degrees of freedom are considered and entries for which Dirichlet boundary conditions apply are set to zero.

The kinetic energy of the system at time t_n can then be computed by (compare to Equation (3.37))

$${}^{Q}T_n = \frac{1}{2} \, {}^{Q}\hat{\underline{p}}_n \cdot \underline{\underline{\hat{M}}}^{-1} \cdot {}^{Q}\hat{\underline{p}}_n. \tag{5.40}$$

Because there is no coupling between finite element associated entries and multibody system entries in the global mass matrix $\underline{\underline{\hat{M}}}$, the total energy of the system can easily be split and assigned to the finite element system and the multibody system via a block-wise evaluation of Equation (5.40).

5.4 Numerical examples

The numerical examples presented in this work give insight into the capabilities of the introduced simulation framework. The modular structure of the equations, as a result of the director formulation, allows for easy future adaption to advanced finite element models. The structure preserving integration scheme has two important advantages compared to standard methods: First, the differential algebraic system resulting from the coupling between the muscle model and the multibody system can be solved directly and with numerical accuracy, avoiding numerical drift for the constraints. Second, the integration scheme does not show numerical dissipation, representing the physical system realistically with respect to energy and momentum and allowing for meaningful energy investigations.

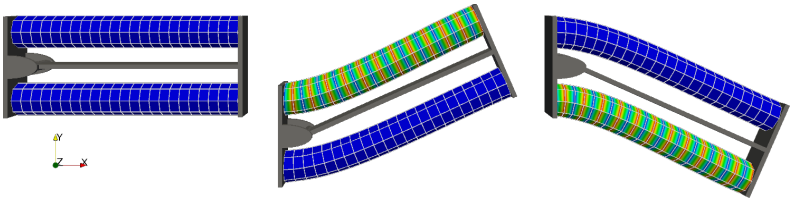

Figure 5.4: Revolute joint with two artificial muscles in agonist-antagonist configuration, reference configuration (left) and deflected states (mid, right) with applied electric potential in red and ground in blue.

Table 5.1: Numerical example parameters for the revolute joint in agonist-antagonist configuration.

parameter	value	unit
μ	0.233	MPa
λ	10	MPa
c_1	$5 \cdot 10^{-8}$	$\mathrm{N} \,/\, \mathrm{V}^2$
c_2	$1 \cdot 10^{-9}$	$\mathrm{N} \,/\, \mathrm{V}^2$
ε_0	$8.8542 \cdot 10^{-12}$	$\mathrm{A\,s} \,/\, (\mathrm{V\,m})$
ρ_0	$1 \cdot 10^{-3}$	$\mathrm{g} \,/\, \mathrm{mm}$
m	40	g
J^S	$3.17 \cdot 10^5$	$\mathrm{g\,mm}^2$
ℓ	46	mm
$\boldsymbol{g}_\mathrm{v}$	$\begin{pmatrix} 0 & -9.81 & 0 \end{pmatrix}^T$	$\mathrm{m/s}^2$

Basis for the following examples is a small multibody system consisting of a single rigid body that is fixed in space via a revolute joint and that is actuated by two artificial muscles. Applying a voltage to the artificial muscles allows controlling the deflection angle α of the revolute joint.

The example geometry is shown in Figure 5.4. Actuating electric fields are obtained by prescribing voltages to the nodes of the finite element model in form of Dirichlet boundary conditions. When electric field strengths are given in the following examples, they refer to the electric field magnitude in the initial reference state where $\alpha = 0$ and the muscles are undeformed. The rigid body in form of a pendulum with mass m and inertia J^S has its centre of mass S located at the distance ℓ from the revolute joint (see Table 5.1 for values). The joint is placed in the origin of the global coordinate system with its rotation

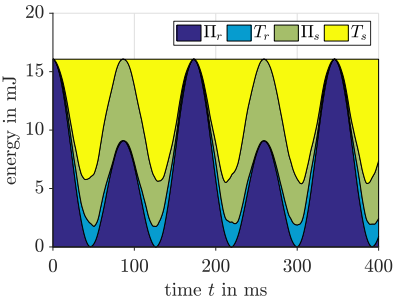

Figure 5.5: Energy exchange between the finite element model and the rigid body.

axis being identical to the z-axis. The angle α describes the pendulum swing relative to its reference configuration, where the pendulum points along the x-axis. The two muscles each have a length of 100 mm and a diameter of 10 mm. In reference configuration, the muscles run parallel to the x-axis. The right ends of the muscles are connected to the pendulum via constraints, whereas the left ends of the muscles are fixed in space at the position $x = -10\,\mathrm{mm}$ via Dirichlet boundary conditions. The assembly is symmetric and the centre lines of the muscles are 30 mm apart. The zero level for potential energy due to gravitation is the origin of the global coordinate system. Each muscle is discretised with 92 finite elements and tri-linear shape functions. Gravity in negative y-direction is active only for some examples as stated later. The finite element potential energy density and viscoelastic damping model are taken from Equations (4.35) and (2.24), respectively. The damping parameter η is specified individually for each of the following simulations.

5.4.1 Energy behaviour of the variational integrator

In the first simulation, the energy behaviour of the derived structure preserving integration scheme is analysed. The integration scheme is known for its good energy behaviour, meaning neither numerical dissipation, nor artificial energy gain is present and the energy error is bounded even for long simulations [Hair00]. This is best seen for conservative problems, where the total energy is constant. Therefore, the damping parameter $\eta = 0$ is chosen such that there is no damping present at all. When a voltage is applied to the upper muscle such that the electric field magnitude in reference configuration is $E = 6\,\mathrm{kV/mm}$, the pendulum starts oscillating. As seen in Figure 5.5, initially all energy

Table 5.2: Long time simulation energy error.

Δt	$H_{\max}^{\text{err}}$
2.0 ms	$9.61 \cdot 10^{-5}$ %
1.0 ms	$2.29 \cdot 10^{-5}$ %
0.1 ms	$2.88 \cdot 10^{-7}$ %

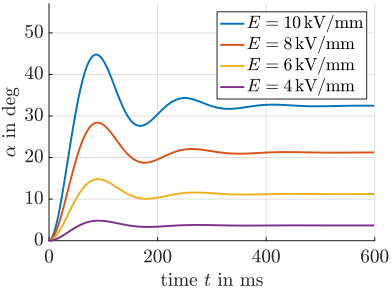

Figure 5.6: Transient response for different applied voltages.

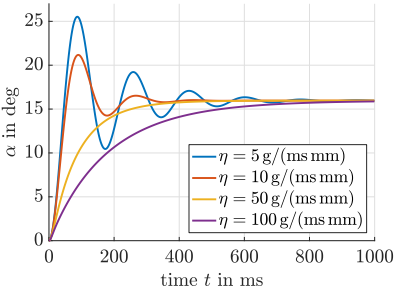

Figure 5.7: Transient response for different damping parameters.

is stored as potential energy in the electric field of the upper muscle. With increasing time, the pendulum as well as the muscles start moving and energies are exchanged, however, the total energy is conserved almost exactly. Note that for visualization reasons the baseline of Figure 5.5 is chosen such that the minimum potential energy of the finite element model is zero.

Table 5.2 shows the maximum energy error $H_{\max}^{\text{err}}$ for a long term simulation with $t_N = 5\,\text{s}$ and different time step sizes. The energy error is given relative to the initial total energy, which is 25 963 mJ. The total energy is oscillating but bounded, such that the energy is neither increasing nor decreasing in total, even for a large number of time steps. For smaller time step sizes, the energy deviation is decreasing as expected, leading to a narrower energy band.

5.4.2 Transient response for constant voltages

In Figure 5.6, the transient response of the revolute joint for different electric field strengths is shown. The damping parameter is set to $\eta = 10\,\text{g/ms mm}$.

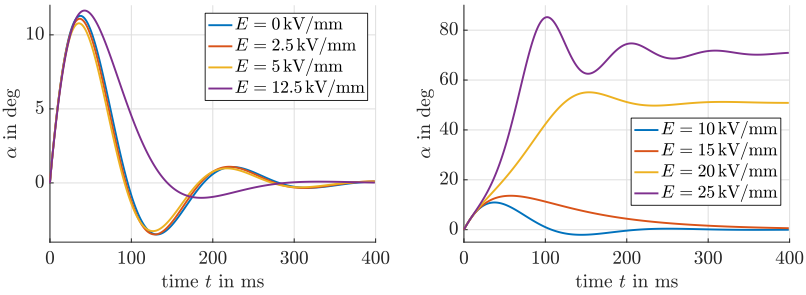

(a) Stiffness variation. (b) Non-linear effect and snap-through.

Figure 5.8: Response of the joint to external shock.

After an oscillatory phase for the first 400 ms, all kinetic energy is dissipated by the viscoelastic damping terms and the revolute joint reaches its steady state. The larger the electric field strength is, the higher is the final deflection angle. According to the finite element material model given in Equation (4.35), the induced electromechanical stress grows quadratically with the electric field strength. Also note that larger electric fields result in stronger oscillations. These oscillations have to be controlled in order to obtain appropriate positioning behaviour.

Figure 5.7 shows the transient response of the revolute joint for different damping parameters η and an electric field strength of $7\,\mathrm{kV/mm}$ in reference configuration. If η is increased, oscillations are damped until critical damping is reached. This is the case for some value of η between the red and the yellow line. If the critical damping value is exceeded, no oscillations occur any more. If η is further increased, the system takes longer until the steady state is reached. Note that, however, usually the damping parameter η is given by the material characteristics and cannot be chosen arbitrarily.

5.4.3 Passive behaviour joint stiffness variation

In the next example, gravity is neglected, viscoelastic damping is set to $\eta = 10\,\mathrm{g/ms\,mm}$ and the revolute joint has an initial angular momentum of $p_0 = 5000\,\mathrm{N\,mm\,ms}$ that might result from an external shock. The blue curve in Figure 5.8a shows the oscillatory response of the revolute joint without any additional electrical loading. The pendulum reaches a maximum angle of about 11 deg, before it oscillates back to its reference state. Now, the same voltage is

applied to both muscles at the same time. It can be observed that small values for E (red and yellow line) make the revolute joint stiffer. The maximum deflection angle decreases and the oscillatory frequency increases. This effect grows for larger electric fields. However, the effect is quite small compared to the total pendulum swing. If the electric field is further increased (purple line), the effect inverts. The maximum angle increases and the oscillation frequency decreases.

Figure 5.8b shows the response of the revolute joint for even larger electric fields. If the electric field in reference state exceeds a certain limit (yellow line), the pendulum does not return back to its initial state, but reaches another equilibrium point. This new equilibrium point depends on the applied electric field, as the steady state angle grows with increasing electric field magnitude.

The reason for this non-linear effect is the varying electric field strength, when the muscles deform. If the pendulum moves upwards, the upper muscle is compressed while the lower muscle is stretched. For constant electrical boundary conditions, i.e. constant voltage at finite element nodes, this leads to an increasing electric field magnitude for the compressed upper muscle, while the electric field strength is decreasing for the stretched lower muscle. The resulting larger electromechanical stress in the upper muscle favours the motion upwards. If the applied voltage is very large, the effect reinforces itself until the tensile fore of the lower muscle is large enough to stop further deflection.

5.5 Volumetric locking in dielectric elastomer actuated systems

The mechanical properties of commonly used polymers for dielectric elastomers are well covered by hyperelastic material models, where the stress-strain relation is derived from a strain energy function. Incompressibility is often approximated by a Poisson's ratio close to 0.5 or a very large bulk modulus. This, however, is like enforcing the incompressibility condition with a penalty method [Oden82] that, due to the spatial finite element discretisation, might lead to volumetric locking [Bone08, Brin96, Hugh80, Mieh94, Pari03, Weis06]. As a result, the material is artificially stiffened, not leading to physically meaningful simulation results. In analogy to the three-field formulation for purely mechanical problems, in this section additional degrees of freedom are added to the electromechanically coupled material model, leading to a multi-field formulation. Combined with reduced spatial integration for the additional fields, volumetric locking for incompressible and nearly incompressible materials

is avoided. Depending on the specific choice of additional fields, different formulations are obtained. In the framework of dielectric elastomer actuator simulation and structure preserving time integration, these formulations are compared in terms of achievable incompressibility, tendency to volume-locking and computational cost. Parts of this section were presented at the EuroEAP conference 2016 [Schl16a].

5.5.1 Volumetric-isochoric split of hyperelastic material models and reduced integration

In order to treat volumetric and isochoric effects separately, the strain energy from the purely mechanical hyperelastic material approach (e.g. Equation (2.20)) is split such that

$$\Phi(\boldsymbol{F}) = \Phi^{\diamond}(\boldsymbol{F}^{\diamond}) + \Phi^{\circ}(\boldsymbol{F}^{\circ}), \tag{5.41}$$

where $\Phi^{\diamond}(\boldsymbol{F}^{\diamond})$ is the isochoric part of the strain energy and $\Phi^{\circ}(\boldsymbol{F}^{\circ})$ is the volumetric part of the strain energy. The isochoric part usually has the same form for all Neo-Hookean approaches and reads [Bone08, Pari03]

$$\Phi^{\diamond}(\boldsymbol{F}^{\diamond}) = \frac{\mu}{2}[\boldsymbol{C}^{\diamond} : \mathbf{1} - 3]. \tag{5.42}$$

For the volumetric part Φ° however, different approaches are found in literature. The existence of a purely volumetric term like $-\mu \ln J$ is important in order to allow for a stress free state in the undeformed configuration [Brin96]. Bonet and Wood [Bone08] extend this term with a quadratic component to obtain

$$\Phi^{\circ\,\mathrm{BW}}(\boldsymbol{F}^{\circ}) = -\mu \ln(J) + \frac{\lambda}{2}[\ln(J)]^2 \tag{5.43}$$

for general compressible materials. This approach fulfils the basic requirements on hyperelastic material models, i.e. $\lim_{J\to 0} \Phi^{\circ\,\mathrm{BW}} = \infty$ and $\lim_{J\to\infty} \Phi^{\circ\,\mathrm{BW}} = \infty$. For nearly incompressible materials, Parisch [Pari03] as well as Bonet and Wood [Bone08] propose the following form

$$\Phi^{\circ\,\mathrm{PAR}}(\boldsymbol{F}^{\circ}) = \frac{\kappa}{2}\,(J-1)^2\,. \tag{5.44}$$

This form does not strictly satisfy the requirements on hyperelastic models, because $\lim_{J\to 0} \Phi^{\circ\,\mathrm{PAR}} \neq \infty$. According to [Pari03], this does not lead to problems for nearly incompressible materials in practical applications. More important than the specific choice of the volumetric material model is the value for the bulk modulus κ. For nearly incompressible materials where $\kappa \in [10^3, 10^4]\mu$,

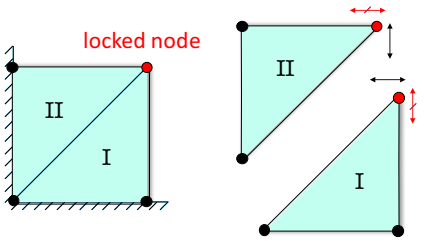

Figure 5.9: Simplified volumetric locking illustration for a two-dimensional problem.

the bulk modulus acts as a penalty parameter that enforces the restriction $J \approx 1$.

Low order finite element discretisations of the displacement variables, like linear shape functions, might not provide enough degrees of freedom to satisfy the (nearly) incompressibility restriction (2.13) for every point in the continuum, resulting in volumetric locking. If volumetric locking happens, the material behaviour is overly stiff. In the extreme case, the material is totally stiff, allowing for no motion at all. A simplified two-dimensional example shall illustrate that point.

Consider a plain quadratic geometry as illustrated in Figure 5.9. The left as well as the bottom edge of the geometry are fixed via Dirichlet boundary conditions. The surface is split into two triangular finite elements (I and II) with linear shape functions. Each vertex of the finite element has two translational degrees of freedom to move within the plane. Due to the boundary conditions, only the upper right (red) vertex is free to move. Imposing incompressibility conditions on the geometry still allows for motion: The upper right vertex can move diagonally (to the upper left and to the lower right direction) without changing the volume of the geometry as a whole. However, considering the individual finite elements separately, motion is prohibited. While the first element only allows for horizontal motion of the red vertex, the second element only allows for vertical motion of the red vertex such that the volume is preserved for the finite elements individually. Because the two elements share the degrees of freedom associated with the red vertex, in total, no motion is possible any more. As a result of the specific finite element discretisation, the geometry is locked.

If the incompressibility condition is “softened” to hold true for the whole geometry rather than for individual elements, the locking problem might be

avoided. This idea can be transferred to more complicated three-dimensional problems, leading to the mean dilatation method [Hugh80, Mieh94]. The general idea of the mean dilatation method is summarised as follows:

1. Introduce a new dilatation field $\hat{J}$ to the problem. Besides the deformation gradient field that primarily accounts for isochoric deformation, the new dilatation field is responsible for volumetric deformation.

2. Under-integrate the dilatation field during finite element assembly. Under-integration is obtained by using a lower order finite element approximation approach than for displacement variables. If linear shape functions are used for the displacement, the dilatation field is constant per cell and hence discontinuous along finite element boundaries.

3. Apply the (nearly) incompressibility constraint to the under-integrated dilatation field. Due to the reduced integration approach, the incompressibility constraint is "softened" as it affects only one degree of freedom per finite element.

4. Connect the dilatation field to the geometry's kinematics $\hat{J} = \det \boldsymbol{F}$ via an under-integrated Lagrange multiplier. The Lagrange multiplier $\hat{p}$ turns out to be the hydrostatic pressure within a finite element.

For purely mechanical problems with a deformation field $\boldsymbol{F}$ only, this procedure adds two more fields to the problem, namely the dilatation field $\hat{J}$ and the pressure field $\hat{p}$. The resulting system is composed of a total of three fields and this procedure is also known as the three-field formulation.

In the following section, the three-field formulation is extended with electromechanical coupling terms, resulting in a multi-field formulation. Different variations of the common theory are presented and compared in terms of achievable incompressibility, tendency to volume-locking and computational cost.

5.5.2 Electromechanically coupled and nearly incompressible multi-field formulations

The total potential energy density of the coupled system is separated such that

$$\Omega = \Phi^{\diamond} + \Phi^{\circ} + \Phi^{\mathrm{ele}} + \Phi^{\text{free space}}, \tag{5.45}$$

where $\Phi^{\diamond}(\boldsymbol{F}^{\diamond})$ is the purely mechanical isochoric part that is taken from Equation (5.42),

$$\Phi^{\text{ele}}(\boldsymbol{F}, \boldsymbol{E}) = c_1 \boldsymbol{E} \cdot \boldsymbol{E} + c_2 \boldsymbol{C} : [\boldsymbol{E} \otimes \boldsymbol{E}] \tag{5.46}$$

contains purely electrical and electromechanical coupling parts (compare to Section 4.2.3) and

$$\Phi^{\text{free space}} = -\frac{1}{2} \varepsilon_0 J \boldsymbol{C}^{-1} : [\boldsymbol{E} \otimes \boldsymbol{E}] \tag{5.47}$$

is the free space contribution [Vu07b] from Equation (4.34).

For the volumetric energy density Φ°, four different material models are considered. The first model

$$\Phi^{\circ}_{\text{I}}(\boldsymbol{F}^{\circ}) = \frac{\kappa}{2}(J-1)^2 \tag{5.48}$$

is based on a classical displacement formulation, extended by electromechanical coupling terms. In contrast to the model presented in Equation (2.20) and used throughout Chapter 4, the volumetric contribution is here based on the approach introduced in Equation (5.44). The total electromechanically coupled model based on $\Phi^{\circ}_{\text{I}}(\boldsymbol{F}^{\circ})$ is a two-field model $(\boldsymbol{F}, \boldsymbol{E})$. The second model

$$\Phi^{\circ}_{\text{II}}(\boldsymbol{F}^{\circ}, \hat{J}, \hat{p}) = \frac{\kappa}{2}(\hat{J}-1)^2 + \hat{p}(J - \hat{J}) \tag{5.49}$$

is formulated in analogy to a nearly incompressible three-field formulation for purely mechanical problems. Together with electromechanical coupling terms, a four-field model is obtained $(\boldsymbol{F}, \boldsymbol{E}, \hat{J}, \hat{p})$. Model III

$$\Phi^{\circ}_{\text{III}}(\boldsymbol{F}^{\circ}, \hat{J}, \hat{p}, \hat{\lambda}) = \hat{p}(J - \hat{J}) + \hat{\lambda}(\hat{J} - 1) \tag{5.50}$$

extends model II by another field $\hat{\lambda}$ accounting for incompressibility. The under-integrated field $\hat{\lambda}$ acts as a Lagrange multiplier that enforces incompressibility via the "weak" dilatation field. The result is an electromechanically coupled five-field formulation $(\boldsymbol{F}, \boldsymbol{E}, \hat{J}, \hat{p}, \hat{\lambda})$ that allows for true incompressibility. Note that in the variational time integration scheme, additional constraints that are enforced via Lagrange multipliers can be considered directly and without index reduction and the constraints are fulfilled exactly at the discrete time nodes as shown in Section 3.2. Finally, model IV

$$\Phi^{\circ}_{\text{IV}}(\boldsymbol{F}^{\circ}, \hat{\lambda}) = \hat{\lambda}(J - 1) \tag{5.51}$$

is based on the idea to decrease the amount of additional fields that are necessary to obtain fully incompressible behaviour. The incompressibility constraint is here applied to the determinant of the deformation gradient J

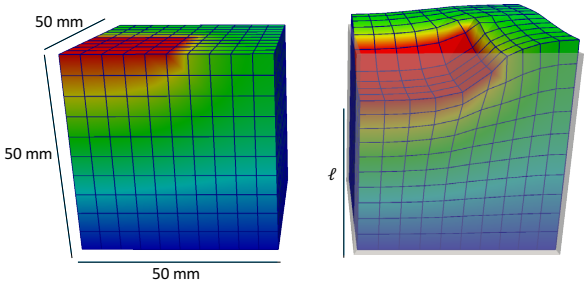

Figure 5.10: Boxed dielectric elastomer cube to investigate volumetric locking.

directly, however the associated Lagrange multiplier $\hat{\lambda}$ is under-integrated. The electromechanically coupled model based on $\Phi^{\circ}_{\mathrm{IV}}(\boldsymbol{F}^{\circ})$ is a three-field formulation $(\boldsymbol{F}, \boldsymbol{E}, \hat{\lambda})$. Note that all quantities with a hat $(\hat{\bullet})$ are under-integrated.

While the under-integrated dilatation field $\hat{J}$ is temporally discretised via a general midpoint quadrature, the additional under-integrated fields $(\hat{p}, \hat{\lambda})$ are considered as Lagrange multipliers and discretised with a trapezoidal quadrature when evaluating the discrete Euler-Lagrange-Equations as described in Section 3.2. This way, the incompressibility constraints are enforced exactly at the discrete time nodes (to numerical accuracy).

In addition to the finite element discretisations for the displacement (2.31) and electric potential (4.41), lower order shape functions are introduced for the additional fields, i.e.

$$\hat{J}(\boldsymbol{X}, t) \approx \underline{r}^{\mathrm{el}}(t) \odot \underline{N}^{\mathrm{dil}}_{\mathrm{el}}(\boldsymbol{X}) \tag{5.52a}$$

$$\hat{p}(\boldsymbol{X}, t) \approx \underline{r}^{\mathrm{el}}(t) \odot \underline{N}^{\mathrm{p}}_{\mathrm{el}}(\boldsymbol{X}) \tag{5.52b}$$

$$\hat{\lambda}(\boldsymbol{X}, t) \approx \underline{r}^{\mathrm{el}}(t) \odot \underline{N}^{\lambda}_{\mathrm{el}}(\boldsymbol{X}) \tag{5.52c}$$

where the finite element configuration $\underline{r}$ is accordingly extended with additional degrees of freedom for $\hat{J}, \hat{\lambda}$ and $\hat{p}$.

5.5.3 Performance of different multi-field approaches

The four Neo-Hookean material models (5.45) with $\Phi^{\circ}_{\mathrm{I}}, \ldots, \Phi^{\circ}_{\mathrm{IV}}$ are tested with three numerical examples that are typical for dielectric actuator simulation. The first numerical example is a DEA cube where all sides except the top

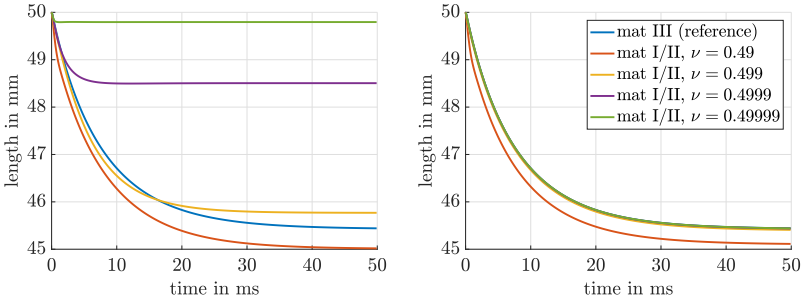

(a) Material I. (b) Material II.

Figure 5.11: Response of the boxed DEA cube to the applied voltage versus time for different Poisson ratios.

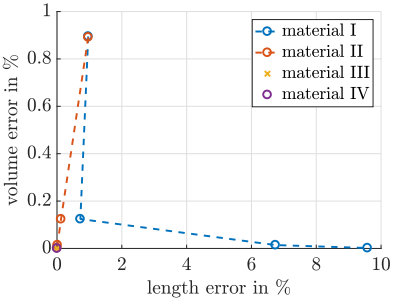

Figure 5.12: Relative error concerning length and volume of the DEA cube.

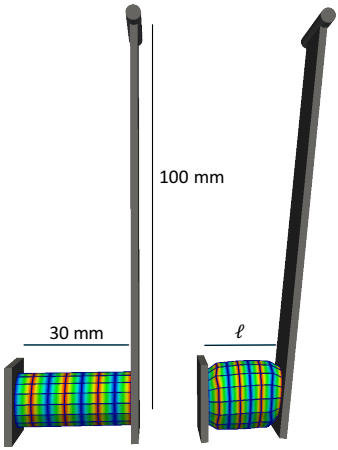

Figure 5.13: Dielectric elastomer switch model to investigate volumetric locking.

are fixed and an applied voltage exerts pressure to part of the top surface, as illustrated in Figure 5.10. The resulting contracted lengths for different Poisson rations ranging between 0.49 and 0.49999 are shown in Figure 5.11a for material I and in Figure 5.11b for material II. The blue curve corresponds to a simulation with material III and is considered as the reference solution. It can be observed that material I is locking for almost all ν and it is not possible to obtain physically meaningful results for nearly incompressible materials. Material II however, shows good accuracy. For $\nu = 0.49$, incompressibility is not achieved yet, but when ν is further increased towards the limit 0.5, locking effects do not occur. In Figure 5.12, the relative error regarding contracted length (steady state) and volume conservation is shown for the different material models, where the results from material III act as a reference solution. Note that the simulation results of material model IV are identical to the results from model III (to numerical accuracy). It can be observed that the ideal point (zero error, lower left corner) is reached by material II for large Poisson ratios. Even though material I does not reach this point for any value of ν, it should be noted that the error in volume conservation is quite small (less than 0.2 %) for still acceptable length errors (less than 1 %).

The second example is a switch in form of a small stacked dielectric actuator that is connected to a rigid body fixed in space by revolute joint, as illustrated in Figure 5.13. When a voltage is applied to the stacked actuator, the switch is moved, where the damping parameter η is chosen large enough such that

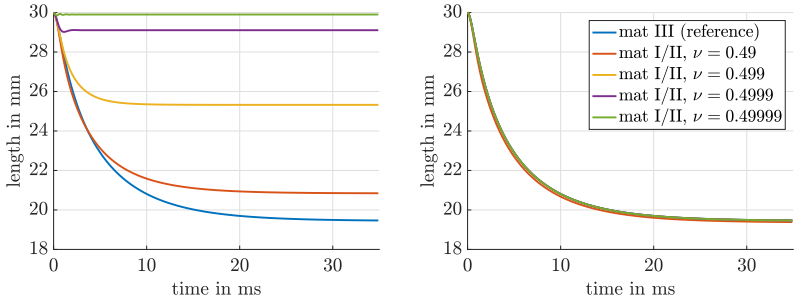

(a) Material I. (b) Material II.

Figure 5.14: Response of the DEA switch to the applied voltage versus time for different Poisson ratios.

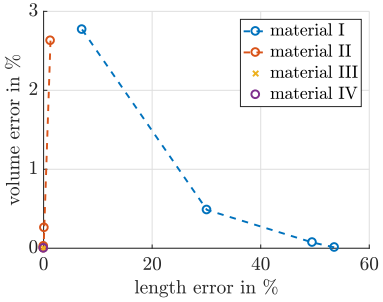

Figure 5.15: Relative error concerning length and volume of the DEA switch.

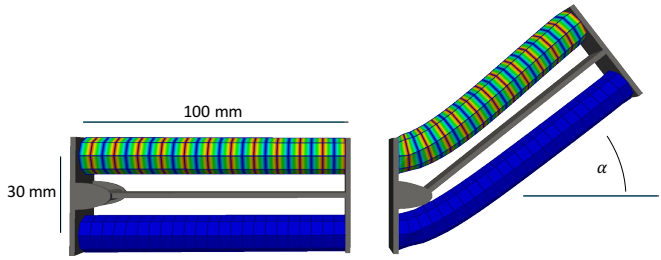

Figure 5.16: Dielectric elastomer actuated joint to investigate volumetric locking.

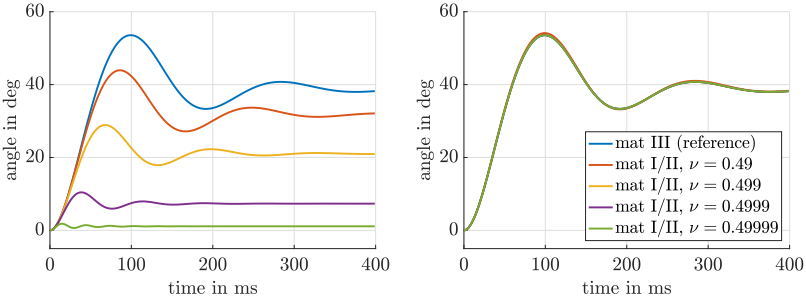

(a) Material I.

(b) Material II.

Figure 5.17: Response of the DEA joint to the applied voltage versus time for different Poisson ratios.

no oscillations occur. The expansion of the cross section area of the actuator during compression is hindered on both sides of the actuator due to constraints coupling the actuator to the rigid body. The length of the contracted muscle is chosen as the quantity for further evaluation of volumetric locking. In Figure 5.14a it is seen very clearly that material I shows very poor behaviour for the nearly incompressible case. Again, material III (blue curve) is considered as being the reference solution and the results from material IV are identical to the results from material III. Volumetric locking happens for all tested values of ν. Material II, to be observed in Figure 5.14b shows very good behaviour for all values of ν. In Figure 5.15, the relative errors for different material models of the contracted steady state are plotted again. For this example, material model I shows even worse performance than for the boxed DEA cube.

The last example is a revolute joint controlled by two stacked actuators in

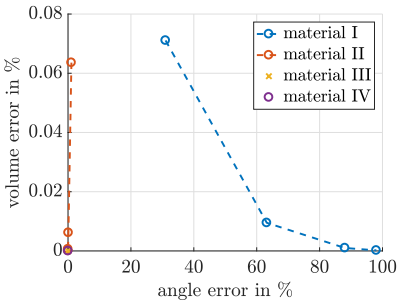

Figure 5.18: Relative error concerning length and volume of the DEA joint.

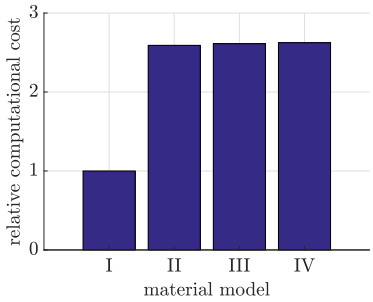

Figure 5.19: Relative computational cost of the material models.

agonist-antagonist configuration, as illustrated in Figure 5.16. Due to inertia terms of the actuated joint, the joint is oscillating after applying a voltage before it approaches its steady state. Figure 5.17a confirms the poor behaviour of material model I for the nearly incompressible actuator, while material II (Figure 5.17b) shows similar results (being consistent with respect to model III) for all values of ν. Figure 5.18 illustrates the large errors in the resulting steady state angle of the joint when material I is used. Note that again, model III and model IV give identical simulation results (to numerical accuracy).

The results show that material model I is not suited to approximate the incompressible material behaviour of dielectric elastomers. Large Poisson ratios inevitably lead to volumetric locking, even though the model is quite easy to implement and computationally very quick. Model II covers nearly incompressible behaviour very well in all applications, but the computational cost rises by a factor of about 2.6 compared to model I. Figure 5.19 compares the computational cost between the different material models. Model III performs quite well, especially in combination with the structure preserving time integration scheme, allowing for exact incompressibility without any significant increase in computational cost. Model IV does remarkably not decrease the computational cost compared to model III and hence does not offer any notable advantage. Moreover, pressure oscillations might occur (checkerboard pattern) [Holz00] so that in general model III should be preferred over model IV.

6 MulDi – A variational multibody director library

Experience has shown that the set-up of new kinematic models that are actuated by artificial muscles is very time consuming. While the creation and alignment of finite element meshes for dielectric elastomers is straightforward and easy to automate (using software like Trelis[1] or libraries like deal.II [Bang07]), the assembly of kinematic chains in the presented formulation has to be done manually. This involves several tasks like specifying consistent initial configurations including appropriate orientation of the directors and dealing with singularities that might occur for certain joints [Bets06].

One of the most challenging tasks is the derivation of the null space matrix for the assembled multibody system. For simple kinematic pairs, null space matrices can be found in literature like [Bets06, Leye08b, Maas12], however for more complex kinematic systems, the assembly of the null space matrix is not described in literature. In [Bets06], the assembly of a null space matrix for a kinematic chain without tree structure, without spatially fixed points (from now on called "anchor") and with consecutive numbering of the rigid bodies is shown. However, the described approach can not easily be extended for the automated creation of null space matrices for more general kinematic chains. Finally, obtaining higher order derivative information (that is for example needed for optimisation tasks) about kinematic systems is in general very complex as well.

Because the director formulation generally allows for a very modular design but no supporting software or library is currently available (to the best of my knowledge), within the scope of this work, a variational multibody director based C++ library, in short MulDi, has been created. The main features of this library are summarised as follows:

- support the set-up, analysis, simulation and optimal control of multibody systems
- based on the director formulation and variational integration
- easy to use, self-explanatory operation
- support of open kinematic chains, closed kinematic chains, tree structured systems, anchored chains and free chains

[1] http://www.csimsoft.com/trelis

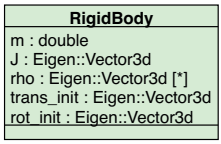

Figure 6.1: UML diagram of the `RigidBody` class with most important attributes.

- support of the null space method whenever possible
- provide exact gradients (Jacobian, Hessian) via automatic differentiation
- internally based on CppAD [Bell17] for automatic differentiation and on the linear algebra package Eigen [Guen17] for high efficiency (invisible to user)

The following sections give an introduction to the general structure of the library and discuss the assembly of the null space matrix in some more detail.

6.1 The basic data structures

The core of MulDi is composed of only three structures: the `RigidBody` class, the abstract `Joint` class and the `MultibodySystem` class. A UML (unified modelling language) diagram of the most important attributes of the `RigidBody` class is shown in Figure 6.1. A rigid body has a mass `m` and moments of inertia in principle axis stored in a three dimensional vector `J`. Moreover, each rigid body can have an arbitrary amount of connectors `rho`. Each connector is a three dimensional vector with coordinates given in the local rigid body coordinate system. The connectors specify points where other elements can be attached to, like joints or user defined elements. The rigid body object does not store information about its current configuration. Configurations are only passed to functions of the class via arguments and return objects. However, the `RigidBody` class stores information about the rigid bodies initial configuration. Therefore, `trans_init` is a vector pointing to the initial location of the centre of gravity of the rigid body and `rot_init` accounts for the initial orientation. The initial orientation is specified by three angles that correspond to rotations about principle axes.

The abstract `Joint` class acts as an interface for various types of Joints that can be further specified by the user of the library. While the `Joint` class itself only provides functionality that is consistent for all joints (like that they

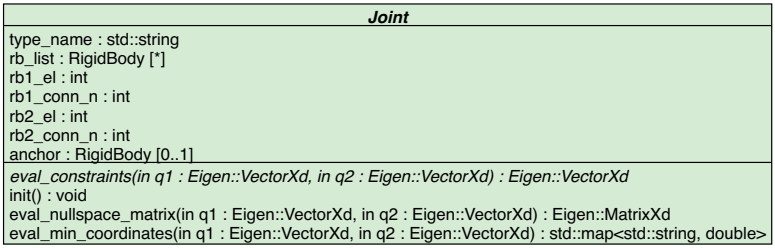

Figure 6.2: UML diagram of the abstract `Joint` class with most important attributes and functions.

connect two rigid bodies), joint specific properties (like the joint constraints) are to be implemented by the user. Implementations for some standard joints are provided by the library. In Figure 6.2, the most important attributes and functions of the abstract `Joint` class are summarised. The variable `type_name` holds a name for the joint type that can be used for post processing to distinguish different types of joints. The two rigid bodies that are connected by the joint must be included in `rb_list` that holds an arbitrary number of `RigidBody` objects. The `Joint` class actually stores only a reference to a global rigid body list. This allows to associate rigid bodies with several joints without storing duplicates. The variables `rb1_el` and `rb1_conn_n` store the number of the rigid body in the rigid body list and the concerned connector number, respectively. The associated connector specifies the position where the joint should be attached to. The same holds for the variables `rb2_el` and `rb2_conn_n` that relate to the second rigid body being involved. If the joint is anchored, i.e. it is fixed in space with one end and there is only one rigid body that is connected to the other end, then `anchor` acts as a replacement for the missing rigid body, storing the spatial fixing point as the initial translation of a fictive rigid body. Note that talking about the two "ends" of a joint is a symbolic expression, referring to the fact that a MulDi joint always connects two rigid bodies.

The only necessary function of the abstract `Joint` class that has to be implemented before creating a specific instance is `eval_constraints()`. As a function of the configurations of the two involved rigid bodies, `eval_constraints()` returns a vector with an arbitrary number of constraint expressions that equal zero. Optionally, the `init()` function can be implemented to handle singularities that might occur for certain configurations. The optional function `eval_nullspace_matrix()` returns the null space matrix for a simple kinematic pair. This information is used to assemble the null space matrix for the whole multibody system, as shown in Section 6.3. Only if `eval_nullspace_matrix()`

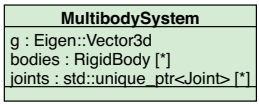

Figure 6.3: UML diagram of the `MultibodySystem` class with most important attributes.

is implemented for all joints in use, a global null space matrix can be assembled. Finally, the function `eval_min_coordinates` provides an interface to work with minimal coordinates. It returns a list with an arbitrary number of pairs, where each pair consists of a name (for the physical interpretation of the minimal coordinate) and the current value of the coordinate as a function of the configuration of the two rigid bodies.

The `MultibodySystem` class, illustrated in Figure 6.3 holds the multibody system together. It stores a gravitation vector `g`, the global list `bodies` of all rigid bodies that contribute to the multibody system and a list `joints` of all joints that constrain the system. Because `Joint` is abstract, only `unique_ptr` pointers to specific joint implementations are stored. While from this point of view, the `MultibodySystem` class looks very simple, it actually is very powerful as by operating on the two lists for the rigid bodies and the joints, most other information to analyse, simulate and optimise the system can be derived. Not visualised in Figure 6.3, the `MultibodySystem` class provides many functions to work with the system and some of these functions will be introduced in more detail in the following sections.

6.2 Numerical derivation of the discrete Euler-Lagrange-Equations

Once the Lagrange function of a multibody system is set up, all the dynamics and especially the discrete Euler-Lagrange-Equations can be derived from it automatically. The mass matrix of a single rigid body (5.5) can be assembled using the information stored in the `RigidBody` class. Together with the global mass matrix (5.4), the kinetic energy of the system can be obtained as a function of the time derivative of the multibody system configuration $\underline{\dot{s}}$. Also the potential energy can be obtained as a function of the configuration $\underline{s}$ via a loop over all rigid bodies in the system. This is done in the `MultibodySystem` class.

In the `Lagrange` class that stores a reference `mbs` to the `MultibodySystem` object, the continuous Lagrange function is composed of the difference of kinetic and potential energy and the discrete Lagrange function

```
double get_d_Lagrange_fct(VectorXd s, VectorXd s_dot) {...}
```

implements the quadrature rules that were introduced in Equation (3.4). The first derivatives of this function contribute to the discrete Euler-Lagrange-Equations and hence the variational time integration scheme. The second derivatives are required for the Jacobian of the integration scheme when solving forward dynamics. The third derivatives (Hessian of the integration scheme) are needed when solving optimal control tasks. The automatic differentiation (AD) library CppAD [Bell17] is used to compute these derivatives with numerical accuracy.

CppAD is a "tape-based" AD framework. The operations necessary for the evaluation of the function that is to be derived are recorded into a so called tape. Because all algorithms can be decomposed into basic operations (like addition, multiplication, harmonic functions, ...) and for all these basic operations the corresponding derivative operation is known, the AD tapes can be used to evaluate complex derivatives. CppAD provides drivers for first and second derivatives only, however the tape recording can be nested into itself to provide higher derivatives. In the following, this is illustrated in some more detail. First, a tape is recorded for the discrete Lagrangian. Then, the calculation of the derivative of the Lagrangian with respect to the first argument is recorded. Note that code examples in this chapter might be neither complete nor semantically correct. For the sake of simplicity, only relevant parts are highlighted. The examples can be seen as pseudo code with a syntax similar to C++.

The following example illustrates the tape recording for the discrete Lagrangian.

```
typedef CppAD::AD<double> cdouble;
typedef CppAD::AD<cdouble> ccdouble;
CppAD::ADFun<cdouble> tape_Ld;

int n_dof = mbs.get_no_of_dof();
Matrix<ccdouble,Dynamic,1> u(n_dof*2);
u <<   mbs.get_init_config().cast<ccdouble>(), // s_n
       mbs.get_init_config().cast<ccdouble>(), // s_np1
CppAD::Independent(u);

Matrix<ccdouble,Dynamic,1> Ld(1);
Ld(0) = get_d_Lagrange_fct<ccdouble>( u.head(n_dof),
                                      u.tail(n_dof) );
```

```
15 tape_Ld.Dependent(u, Ld);
   tape_Ld.optimize();
```

In order to record a tape, a certain data type for the variables has to be used. In the first two lines, the CppAD type `cdouble`, as well as the nested type `ccdouble` are defined. In line three, the object that will store the tape is initialised. Note that the template parameter of the object specifies the return type. Here, the return type is an AD type meaning that the evaluation of the tape (once it is recorded) can be part of another nested tape recording. In line five and six, an array `u` is initialised that will hold the independent variables, for which derivative information is needed. In this case, the independent variables are the configurations $\underline{s}_n$ and $\underline{s}_{n+1}$. In line seven and eight, the independent variables are initialised with the initial configuration of the multibody system. This avoids singularities that might occur during tape recording if the Lagrangian is evaluated with a zero vector (which is not physically meaningful for the director formulation). In line nine, the tape recording is started. From now on, all operations on the independent variables will be recorded. In line 11, a variable to store the result of the evaluation of the Lagrangian is initialised. CppAD supports and expects vector valued functions. As the Lagrange function returns a scalar only, an array `Ld` that can hold only one variable is created. In line 12 and 13, the Lagrangian is evaluated and the result is stored in the previously created array. The independent variable array `u` is used as an input parameter such that the operations needed to evaluate the Lagrangian are recorded into `Ld`. Finally, in line 15, the tape recording is stopped and stored in `tape_Ld`. The tape now holds all operations needed to compute `Ld` from the independent variables `u`. Line 16 is optional and optimises the tape in terms of memory consumption and evaluation performance.

Next, the recorded tape `tape_Ld` is used to evaluate the first derivatives that are needed for Equation (3.12). However, this evaluation itself is recorded. This is shown in detail for the derivative with respect to the first argument $\underline{s}_n$.

```
CppAD::ADFun<double> tape_D1Ld;

int n_dof = mbs.get_no_of_dof();
Matrix<cdouble,Dynamic,1> u(n_dof*2);
u <<  mbs_.get_init_config().cast<cdouble>(), // s_n
      mbs_.get_init_config().cast<cdouble>(), // s_np1
CppAD::Independent(u);

Matrix<cdouble,Dynamic,1> full_jac = tape_Ld.Jacobian(u);
Matrix<cdouble,Dynamic,1> D1Ld = full_jac.head(n_dof);

tape_D1Ld.Dependent(u, D1Ld);
tape_D1Ld.optimize();
```

In the first line, the variable `tape_D1Ld` that will store the tape for the derivative of the Lagrangian with respect to $\underline{s}_n$ is initialised. Note that the return type of the tape is specified as `double` via the template parameter. The evaluation of the tape later returns common `double` values. In lines three to seven, the independent variables are initialised with default values and tape recording is started as before. However, now the independent variables `u` are of type `cdouble` instead of `ccdouble` as in the tape recording of the Lagrangian. In line nine, the previously recorded tape for the Lagrangian is evaluated to obtain the first derivatives of the Lagrangian. Because the independent variables `u` are used for the evaluation, the evaluation itself is recorded into the variable `full_jac` that is of type `cdouble`. The first `n_dof` entries of `full_jac` correspond to the derivatives with respect to $\underline{s}_n$ and the last `n_dof` entries of `full_jac` correspond to the derivatives with respect to $\underline{s}_{n+1}$. Because the latter derivatives are not needed for now, only the first `n_dof` entries of `full_jac` are stored in the variable `D1Ld`. Finally, in lines 12 and 13, the tape recording is stopped, stored in the variable `tape_D1Ld` and optimised as before.

The tape `tape_D1Ld` can now be used to compute the values via a zero order forward sweep `tape_D1Ld.Forward(0, u)`, to determine the first derivatives via `tape_D1Ld.Jacobian(u)` and to compute the second derivatives via `tape_D1Ld.Hessian(u, i)`, where `i` corresponds to the row in `tape_D1Ld` for which the Hessian matrix is requested. Note that in order to record the tapes, all functions that are used during tape recording (like `get_d_Lagrange_fct`) have to be templated to allow for the CppAD types.

The same procedure is being applied to other derivatives of the Lagrangian (with respect to $\underline{s}_{n+1}$) and to further contributions like non-conservative quantities and null space projections. Moreover the procedure is extended to allow for additional control variables.

6.3 The null space matrix assembly

The automatic assembly of the global null space matrix from the contributions of all joints in the system is split into two tasks: First, independent kinematic chains are identified and involved rigid bodies and joints are sorted such that the global null space matrix can be assembled piecewise while traversing the kinematic chains. The requirements hereto arise from the assembly process of the null space matrix itself that is done in a second step.

The general idea of the matrix assembly algorithm is presented in Section 6.3.1.

Figure 6.4: Kinematic pair with two rigid bodies (vertices 0, 1) that are connected via a joint (edge 0).

Then, in Section 6.3.2, the implementation algorithm is illustrated.

6.3.1 Null space matrix assembly approach

At first, the null space matrix assembly for a kinematic pair is reviewed. Then, the assembly is extended for a chain of several bodies as well as tree structured systems and anchored chains.

Kinematic pair

An isolated kinematic pair consists of two rigid bodies that are connected via a joint, as illustrated in Figure 6.4. In MulDi, rigid bodies are numbered consecutively in the order in which they are added to the system. The same applies for joints. Note that the edge representing the joint is directed. The way null space matrices for kinematic pairs are constructed in [Bets06, Leye08b] assigns a unique direction to the joints. The joint constrains the degrees of freedom of the body where the arrow points to. This rigid body is also referred to as the right rigid body, in contrast to the left rigid body where the arrow originates from. The kinematic pair in Figure 6.4 has $6 + (6 - n_c)$ degrees of freedom, where n_c is the number of constraints the joint imposes on the second rigid body. The minimal velocity array for the kinematic pair can be given by

$$\underline{\dot{s}}^{\min} = \begin{pmatrix} \underline{t}_0 & \underline{\Theta}_1 \end{pmatrix}^T \quad \in \mathbb{R}^{6+(6-n_c)}, \tag{6.1}$$

where $\underline{t}_0 \in \mathbb{R}^6$ is the spin of the left rigid body and $\underline{\Theta}_1 \in \mathbb{R}^{6-n_c}$ contains the minimal velocities of the right rigid body. The spin contains six velocities that correspond to the six degrees of freedom of a rigid body in a three-dimensional space, namely three translational and three rotational. The joint null space matrix $\underline{\underline{T}}_0(\underline{s}) \in \mathbb{R}^{6\times 6+(6-n_c)}$ connects the minimal velocities with the spin of the right rigid body such that

$$\underline{t}_1 = \underline{\underline{T}}_0 \cdot \begin{pmatrix} \underline{t}_0 \\ \underline{\Theta}_1 \end{pmatrix}. \tag{6.2}$$

Figure 6.5: Multibody system with three rigid bodies and two joints in a straight chain.

This joint null space matrix is given for various types of joints in [Bets06]. The total spin of the kinematic pair can be obtained by

$$\begin{pmatrix} \underline{t}_0 \\ \underline{t}_1 \end{pmatrix} = \underbrace{\begin{pmatrix} \underline{\underline{1}} & \underline{\underline{0}} \\ \underline{\underline{T}}_0^a & \underline{\underline{T}}_0^b \end{pmatrix}}_{\underline{\underline{T}}_{\text{ext}}} \cdot \begin{pmatrix} \underline{t}_0 \\ \underline{\Theta}_1 \end{pmatrix}, \tag{6.3}$$

with the 6×6 identity matrix $\underline{\underline{1}}$ and where $\underline{\underline{T}}_0$ is separated such that

$$\underline{\underline{T}}_0 = \begin{pmatrix} \underline{\underline{T}}_0^a & \underline{\underline{T}}_0^b \end{pmatrix} \tag{6.4}$$

with $\underline{\underline{T}}_0^a \in \mathbb{R}^{6\times 6}$ and $\underline{\underline{T}}_0^b \in \mathbb{R}^{6\times(6-n_c)}$.

The connection between the total spin and the redundant director formulation velocities $\dot{\underline{s}}$ is covered by the internal null space matrix $\underline{\underline{T}}_{\text{int}} \in \mathbb{R}^{12\times 6}$ that accounts for the internal rigid body constraints, i.e.

$$\dot{\underline{s}} = \begin{pmatrix} \dot{\underline{s}}^0 \\ \dot{\underline{s}}^1 \end{pmatrix} = \underbrace{\begin{pmatrix} \underline{\underline{T}}_{\text{int}}^0 & \underline{\underline{0}} \\ \underline{\underline{0}} & \underline{\underline{T}}_{\text{int}}^1 \end{pmatrix}}_{\underline{\underline{T}}_{\text{int}}} \cdot \begin{pmatrix} \underline{t}_0 \\ \underline{t}_1 \end{pmatrix}. \tag{6.5}$$

The total null space matrix that directly connects minimal velocities to the redundant director formulation is then given by

$$\underline{\underline{T}} = \underline{\underline{T}}_{\text{int}} \cdot \underline{\underline{T}}_{\text{ext}} \tag{6.6}$$

such that

$$\dot{\underline{s}} = \underline{\underline{T}} \cdot \begin{pmatrix} \underline{t}_0 \\ \underline{\Theta}_1 \end{pmatrix}. \tag{6.7}$$

Multibody chain

The general idea of assembling the null space matrix for a larger system is to split the total composition into the assembly of single kinematic pairs that are extended to account for the surrounding system. This will be illustrated for

the system shown in Figure 6.5. As the composition of the internal null space matrix is straightforward, in the following only the external null space matrix that accounts for the joint constraints is regarded.

It is assumed that for the two joints in Figure 6.5, the two null space matrices $\underline{\underline{T}}_0$ and $\underline{\underline{T}}_1$ are available and that they can be split as described in Equation (6.4). The aim is to find a null space matrix that connects the minimal velocities $\begin{pmatrix}\underline{t}_0 & \underline{\Phi}_1 & \underline{\Phi}_2\end{pmatrix}^T$ with the total spin $\begin{pmatrix}\underline{t}_0 & \underline{t}_1 & \underline{t}_2\end{pmatrix}^T$. In a first step, joint 0 is dealt with such that

$$\begin{pmatrix}\underline{t}_0\\ \underline{t}_1\\ \underline{\Phi}_2\end{pmatrix} = \underbrace{\begin{pmatrix}\underline{\underline{1}} & \underline{\underline{0}} & \underline{\underline{0}}\\ \underline{\underline{T}}^a_0 & \underline{\underline{T}}^b_0 & \underline{\underline{0}}\\ \underline{\underline{0}} & \underline{\underline{0}} & \underline{\underline{\tilde{1}}}\end{pmatrix}}_{\underline{\underline{T}}^0_{\text{ext}}} \cdot \begin{pmatrix}\underline{t}_0\\ \underline{\Phi}_1\\ \underline{\Phi}_2\end{pmatrix}, \tag{6.8}$$

where $\underline{\underline{\tilde{1}}}$ is the identity matrix of appropriate size (here with respect to the minimal velocities $\underline{\Phi}_2$). In a second step, joint 1 is processed, i.e.

$$\begin{pmatrix}\underline{t}_0\\ \underline{t}_1\\ \underline{t}_2\end{pmatrix} = \underbrace{\begin{pmatrix}\underline{\underline{1}} & \underline{\underline{0}} & \underline{\underline{0}}\\ \underline{\underline{0}} & \underline{\underline{1}} & \underline{\underline{0}}\\ \underline{\underline{0}} & \underline{\underline{T}}^a_1 & \underline{\underline{T}}^b_1\end{pmatrix}}_{\underline{\underline{T}}^1_{\text{ext}}} \cdot \begin{pmatrix}\underline{t}_0\\ \underline{t}_1\\ \underline{\Phi}_2\end{pmatrix}. \tag{6.9}$$

The total matrix is then obtained by

$$\underline{\underline{T}}_{\text{ext}} = \underline{\underline{T}}^0_{\text{ext}} \cdot \underline{\underline{T}}^1_{\text{ext}}, \tag{6.10}$$

such that

$$\begin{pmatrix}\underline{t}_0\\ \underline{t}_1\\ \underline{t}_2\end{pmatrix} = \underline{\underline{T}}_{\text{ext}} \cdot \begin{pmatrix}\underline{t}_0\\ \underline{\Phi}_1\\ \underline{\Phi}_2\end{pmatrix}. \tag{6.11}$$

Tree structured system

The system illustrated in Figure 6.6 contains branches. For such systems, the composition works as follows. In a first step

$$\begin{pmatrix}\underline{t}_0\\ \underline{t}_1\\ \underline{\Phi}_2\\ \underline{\Phi}_3\end{pmatrix} = \underbrace{\begin{pmatrix}\underline{\underline{1}} & \underline{\underline{0}} & \underline{\underline{0}} & \underline{\underline{0}}\\ \underline{\underline{T}}^a_0 & \underline{\underline{T}}^b_0 & \underline{\underline{0}} & \underline{\underline{0}}\\ \underline{\underline{0}} & \underline{\underline{0}} & \underline{\underline{1}} & \underline{\underline{0}}\\ \underline{\underline{0}} & \underline{\underline{0}} & \underline{\underline{0}} & \underline{\underline{\tilde{1}}}\end{pmatrix}}_{\underline{\underline{T}}^0_{\text{ext}}} \cdot \begin{pmatrix}\underline{t}_0\\ \underline{\Phi}_1\\ \underline{\Phi}_2\\ \underline{\Phi}_3\end{pmatrix}, \tag{6.12}$$

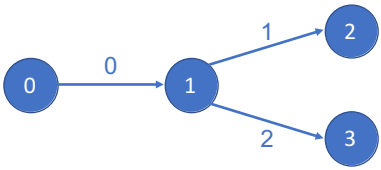

Figure 6.6: Tree structured multibody system with four rigid bodies and three joints.

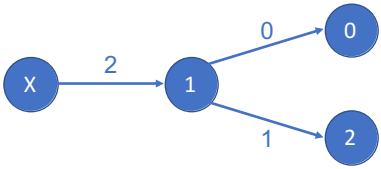

Figure 6.7: Unordered and anchored multibody system with three bodies and three joints.

in a second step

$$\begin{pmatrix} \underline{t}_0 \\ \underline{t}_1 \\ \underline{t}_2 \\ \underline{\Phi}_3 \end{pmatrix} = \underbrace{\begin{pmatrix} \underline{\underline{1}} & \underline{\underline{0}} & \underline{\underline{0}} & \underline{\underline{0}} \\ \underline{\underline{0}} & \underline{\underline{1}} & \underline{\underline{0}} & \underline{\underline{0}} \\ \underline{\underline{0}} & \underline{\underline{T}}^a_1 & \underline{\underline{T}}^b_1 & \underline{\underline{0}} \\ \underline{\underline{0}} & \underline{\underline{0}} & \underline{\underline{0}} & \underline{\underline{1}} \end{pmatrix}}_{\underline{\underline{T}}^1_{\text{ext}}} \cdot \begin{pmatrix} \underline{t}_0 \\ \underline{t}_1 \\ \underline{\Phi}_2 \\ \underline{\Phi}_3 \end{pmatrix}, \tag{6.13}$$

and in a third step

$$\begin{pmatrix} \underline{t}_0 \\ \underline{t}_1 \\ \underline{t}_2 \\ \underline{t}_3 \end{pmatrix} = \underbrace{\begin{pmatrix} \underline{\underline{1}} & \underline{\underline{0}} & \underline{\underline{0}} & \underline{\underline{0}} \\ \underline{\underline{0}} & \underline{\underline{1}} & \underline{\underline{0}} & \underline{\underline{0}} \\ \underline{\underline{0}} & \underline{\underline{0}} & \underline{\underline{1}} & \underline{\underline{0}} \\ \underline{\underline{0}} & \underline{\underline{T}}^a_2 & \underline{\underline{0}} & \underline{\underline{T}}^b_2 \end{pmatrix}}_{\underline{\underline{T}}^2_{\text{ext}}} \cdot \begin{pmatrix} \underline{t}_0 \\ \underline{t}_1 \\ \underline{t}_2 \\ \underline{\Phi}_3 \end{pmatrix}, \tag{6.14}$$

such that the total matrix is given by

$$\underline{\underline{T}}_{\text{ext}} = \underline{\underline{T}}^2_{\text{ext}} \cdot \underline{\underline{T}}^1_{\text{ext}} \cdot \underline{\underline{T}}^0_{\text{ext}}. \tag{6.15}$$

Unordered and anchored system

As the user of MulDi is totally free to set-up multibody systems of arbitrary shape, the joints and bodies might be disordered as illustrated in Figure 6.7. Additionally, joint 2 is anchored, meaning that the left end of the joint is fixed in space and not connected to a rigid body. For such a system, the null space composition might look as follows. First

$$\begin{pmatrix} \underline{t}_1 \\ \underline{\Phi}_2 \\ \underline{\Phi}_0 \end{pmatrix} = \underbrace{\begin{pmatrix} \underline{\underline{T}}^b_2 & \underline{\underline{0}} & \underline{\underline{0}} \\ \underline{\underline{0}} & \underline{\underline{\tilde{1}}} & \underline{\underline{0}} \\ \underline{\underline{0}} & \underline{\underline{0}} & \underline{\underline{\tilde{1}}} \end{pmatrix}}_{\underline{\underline{T}}^2_{\text{ext}}} \cdot \begin{pmatrix} \underline{\Phi}_1 \\ \underline{\Phi}_2 \\ \underline{\Phi}_0 \end{pmatrix}, \tag{6.16}$$

then

$$\begin{pmatrix} \underline{t}_1 \\ \underline{t}_2 \\ \underline{\Phi}_0 \end{pmatrix} = \underbrace{\begin{pmatrix} \underline{\underline{1}} & \underline{\underline{0}} & \underline{\underline{0}} \\ \underline{\underline{T}}^a_1 & \underline{\underline{T}}^b_1 & \underline{\underline{0}} \\ \underline{\underline{0}} & \underline{\underline{0}} & \underline{\underline{\tilde{1}}} \end{pmatrix}}_{\underline{\underline{T}}^1_{\text{ext}}} \cdot \begin{pmatrix} \underline{t}_1 \\ \underline{\Phi}_2 \\ \underline{\Phi}_0 \end{pmatrix}, \tag{6.17}$$

and finally

$$\begin{pmatrix} \underline{t}_1 \\ \underline{t}_2 \\ \underline{t}_0 \end{pmatrix} = \underbrace{\begin{pmatrix} \underline{\underline{1}} & \underline{\underline{0}} & \underline{\underline{0}} \\ \underline{\underline{0}} & \underline{\underline{1}} & \underline{\underline{0}} \\ \underline{\underline{T}}^a_0 & \underline{\underline{0}} & \underline{\underline{T}}^b_0 \end{pmatrix}}_{\underline{\underline{T}}^0_{\text{ext}}} \cdot \begin{pmatrix} \underline{t}_1 \\ \underline{t}_2 \\ \underline{\Phi}_0 \end{pmatrix}, \tag{6.18}$$

such that the total null space matrix can be composed by

$$\underline{\underline{T}}_{\text{ext}} = \underline{\underline{T}}^0_{\text{ext}} \cdot \underline{\underline{T}}^1_{\text{ext}} \cdot \underline{\underline{T}}^2_{\text{ext}}. \tag{6.19}$$

Note that in order to retain a unified assembly process, the rigid body degrees of freedom need to be reordered and the same applies to the order in which joints are processed.

6.3.2 Numerical implementation

To allow for arbitrarily ordered multibody systems as shown in the previous examples, the numerical implementation is composed of two parts. In the first part, a suitable chain traversing scheme for the multibody system is identified, i.e. the order in which rigid bodies and joint are to be processed such that the unified assembly process of the previous examples can be applied. In the second part, the actual assembly of the total null space matrix happens.

Table 6.1: Simplified representation of the available information in the `joints` array within the `MultibodySystem` class after assembling the system of Figure 6.7.

joint number	left rigid body	right rigid body
0	1	0
1	1	2
2	X	1

Table 6.2: Content of `rb_joints` for the system in Figure 6.7.

rigid body number	associated joints
0	0
1	0, 1, 2
2	1

Traversing the kinematic chain

The ordering algorithm will be presented via an application to the system in Figure 6.7. After the user set-up this system, only two arrays are available (see Figure 6.3). The `bodies` array contains the rigid bodies in the order they were added to the system and the `joints` array contains the joints in the order in which they were added. The content of the `joints` array is illustrated in Table 6.1. The entry "X" symbolises the anchor.

The traverse ordering information is stored in the `KinematicChain` class:

```
class KinematicChain {
public:
  KinematicChain();
  bool is_anchored();
  std::vector<int> rb_order;
  std::vector<int> joint_order;
};
```

This class stores the order of rigid body degrees of freedom in `rb_order` and the order of joints in `joint_order`. Moreover, it returns whether or not the chain is anchored.

The following algorithm finds all joints that have a connection to a certain rigid body by traversing the information stored in Table 6.1.

Table 6.3: Kinematic chain representation for the system in Figure 6.7.

joint_order	rb_order
2	1
1	2
0	0

```
vector<int> anchored_joints;
vector< vector<int> > rb_joints(bodies.size());

for (unsigned int i=0; i<joints.size(); ++i) {
  if (joints[i]->is_anchored()) {
    anchored_joints.push_back(i);
  } else {
    rb_joints[joints[i]->get_left_rb()].push_back(i);
  }
  rb_joints[joints[i]->get_right_rb()].push_back(i);
}
```

The array `anchored_joints` holds a list of all joints that are anchored (there might be multiple independent kinematic chains in a system), while the nested array `rb_joints` holds a list of associated joints for all bodies that are present in the system. After applying the algorithm to the example system, the `anchored_joints` array does only have one entry that is 2 (because only joint 2 is anchored) and the content of `rb_joints` is summarised in Table 6.2.

Next, the following algorithm is used to traverse the multibody system.

```
vector<KinematicChain> chain_vector;
vector<int> jointswaiting;

// traverse all kinematic chains that are anchored, start at anchor
while(anchored_joints.size() > 0) {
  KinematicChain chain;

  jointswaiting.push_back(anchored_joints.back());
  anchored_joints.pop_back();

  while (jointswaiting.size() > 0) {
    chain.joint_order.push_back(jointswaiting.back());
    jointswaiting.pop_back();

    int rb_el = joints[chain.joint_order.back()]->get_right_rb();
    chain.rb_order.push_back(rb_el);

    for (unsigned int i=0; i<rb_joints[rb_el].size(); ++i) {
      if (find( chain.joint_order.begin(),
            chain.joint_order.end(),
            rb_joints[rb_el][i] ) == chain.joint_order.end()) {
        jointswaiting.push_back(rb_joints[rb_el][i]);
```

```
      }
    }
  }

  chain_vector.push_back(chain);
}
```

The `chain_vector` object stores information about all kinematic chains of the system. In the current example, there is only one independent chain. Consequently, the `while`-loop in line five is only executed once (for joint 2). The array `jointswaiting` temporarily stores joints numbers. In lines eight and nine, the anchored joint 2 is moved from the `anchored_joints` array to the `jointswaiting` array. In lines 12 and 13, the only entry from joint 2 in `jointswaiting` is moved as the first element to the `joint_order` array of the kinematic chain. In lines 15 and 16, the right rigid body of joint 2 (which is body number 1) is added as the first rigid body to the array `rb_order` of the kinematic chain representation. In lines 18 to 24, all joints that are connected to rigid body 1 (namely 0, 1, 2) and that are not yet contained in `joint_order` are added to `jointswaiting`. As `jointswaiting` was empty, after the operation it contains (0, 1). Then, the `while`-loop in line eleven starts again. The last element in `jointswaiting` (1) is moved to the end of `joint_order`, which now contains (2, 1). Then, the right rigid body of joint 1 (2) is added to `rb_order` which now contains (1, 2). In lines 18 to 24 again, all joints that are associated with rigid body 2 (1) and that are not yet in `joint_order` are added to `jointswaiting` (none). Finally, the `while`-loop in line eleven is executed a last time for the last joint in `jointswaiting` (0). Joint 0 is moved from `jointswaiting` to the end of `joint_order` which now contains (2, 1, 0) and the right rigid body of joint 0 (namely 0) is added to `rb_order`. All of the joints that are connected to rigid body 0 are already in `joint_order` and `jointswaiting` is empty, so the algorithm finishes.

The final contents of the two arrays that describe the kinematic chain are presented in Table 6.3. Note that the given order matches the sequence in which the joints were processed and rigid body degrees of freedom were sorted in Equations (6.16) to (6.18).

If a system also contains non-anchored kinematic chains, they are covered by the following code.

```
while (get_no_of_ordered_rbs(chain_vector) < (int)bodies.size()) {
  KinematicChain chain;

  int rb_el = 0;
  while (is_rb_contained(chain_vector, rb_el)) {
    ++rb_el;
  }
```

```
  chain.rb_order.push_back(rb_el);

  [...]   // fill jointswaiting will all joints associated with rb_el
          // and not yet in joint_order

  while (jointswaiting.size() > 0) {
    [...]
  }

  chain_vector.push_back(chain);
}
```

As long as there are rigid bodies that are not contained in any kinematic chain (line one), create a new chain (line two) and find the first rigid body that is not part of an existing chain (lines four to seven). Then add this body to the current `rb_order` list (line 8), fill `jointswaiting` with all associated joints and execute the while loop (line 13) as before.

It is important to note that the code examples presented in this section do for the sake of clarity not include any exception handling. To illustrate that point, the algorithm does not cover closed loops and the actual implementation in MulDi provides various tests to detect such cases and abort the execution of the traversing algorithm.

Assembling the null space matrix

In this section, the null space matrix assembly process for one kinematic chain is illustrated for the example system of Figure 6.7. It is assumed that the traverse information is given by the arrays `joint_order` and `rb_order`. Before single joint matrices are assembled, general information about the joint degrees of freedom are collected.

```
vector<int> no_of_joint_dof;
int total_no_of_joint_dof = 0;
for (const auto& joint : joint_order) {
  no_of_joint_dof.push_back(6 - joints_[joint]->get_no_of_constraints());
  total_no_of_joint_dof += no_of_joint_dof.back();
}
```

`no_of_joint_dof` (line one) stores information about the degrees of freedom that the joints allow for concerning their right rigid body. The order of entries corresponds to the order of the joints in `joint_order`. The number of degrees of freedom is evaluated in line four by subtracting the number of joint constraints from six. In value `total_no_of_joint_dof`, the total number of all degrees of freedom of the joints is stored. This number corresponds to the

total number of degrees of freedom of an anchored kinematic chain. For free kinematic chains, the total number of degrees of freedom is six plus the value of `total_no_of_joint_dof`.

In the following code, the joint null space matrices ($\underline{\underline{T}}^0_{\text{ext}}$, $\underline{\underline{T}}^1_{\text{ext}}$ and $\underline{\underline{T}}^2_{\text{ext}}$) are assembled.

```
vector< MatrixXd > ext_joint_nullspace_vector;
for (unsigned int i=0; i<joint_order.size(); ++i) {
  int joint = joint_order[i];

  int cols =    (chain.is_anchored() ? 0 : 6)
              + i*6
              + total_no_of_joint_dof;
  total_no_of_joint_dof -= no_of_joint_dof[i];
  int rows =    (chain.is_anchored() ? 0 : 6)
              + (i+1)*6
              + total_no_of_joint_dof;
  MatrixXd ext_joint_nullspace = MatrixXd::Zero(rows, cols);

  ext_joint_nullspace.topLeftCorner(
                (chain.is_anchored() ? i : i+1)*6,
                (chain.is_anchored() ? i : i+1)*6 ).setIdentity();
  ext_joint_nullspace.bottomRightCorner(
                total_no_of_joint_dof,
                total_no_of_joint_dof ).setIdentity();

  MatrixXd joint_nullspace = joints_[joint]->get_nullspace_matrix([...]);
  if (!joints_[joint]->is_anchored()) {
    MatrixXd Ta = joint_nullspace.leftCols(6);
    int left_rb_pos = get_element_pos(  rb_order,
                      joints_[joint]->get_left_rb() );
    ext_joint_nullspace.block(
                              (chain.is_anchored() ? i : i+1)*6,
                              left_rb_pos*6,
                              6,
                              6                   ) = Ta;
  }

  MatrixXd Tb = joint_nullspace.rightCols(no_of_joint_dof[i]);
  ext_joint_nullspace.block(  (chain.is_anchored() ? i : i+1)*6,
                              (chain.is_anchored() ? i : i+1)*6,
                              Tb.rows(),
                              Tb.cols()           ) = Tb;

  ext_joint_nullspace_vector.push_back(ext_joint_nullspace);
}
```

The variable `ext_joint_nullspace_vector` stores the null spaces matrices from the individual joints in the order given by `joint_order`. In the first loop of line two, the variable `joint` (line three) is initialised with the first joint in `joint_order`, here joint 2. The variable `cols` is initialised with the number of columns of $\underline{\underline{T}}^2_{\text{ext}}$ in lines five to seven. Because the chain is

anchored and `i = 0`, this number equals `total_no_of_joint_dof`. In line eight, `total_no_of_joint_dof` is decreased by the number of degrees of freedom of the current joint 2 such that the same variable can be used in lines nine to eleven to evaluate the number of rows of $\underline{\underline{T}}^2_{\text{ext}}$. To illustrate that point, for the rows, the number of entries of $\underline{\Phi}_1$ is replaced by the number of entries of the spin $\underline{t}_1$ (see Equation (6.16)). In line 12, the joint null space matrix is initialised with zeros. In lines 14 to 19 the ones on the diagonal of $\underline{\underline{T}}^2_{\text{ext}}$ are set. In line 21, the kinematic pair null space matrix is obtained and stored in `joint_nullspace`. This matrix depends on the current configuration $\underline{s}$. If the current joint 2 was not anchored, then in lines 22 to 31, the left part of the null space matrix $\underline{\underline{T}}^a_2$ (see Equation (6.4)) would be extracted and inserted into the corresponding position in $\underline{\underline{T}}^2_{\text{ext}}$. Because joint 2 is anchored, only the right part of the null space matrix $\underline{\underline{T}}^b_2$ is obtained and inserted into the corresponding position in $\underline{\underline{T}}^2_{\text{ext}}$ in lines 33 to 37. Finally, in line 39, the joint null space matrix is added to `ext_joint_nullspace_vector`. In subsequent loops (regarding line two), first $\underline{\underline{T}}^1_{\text{ext}}$ and then $\underline{\underline{T}}^0_{\text{ext}}$ are assembled and added to `ext_joint_nullspace_vector` analogously.

As a last step, the joint null space matrices need to be combined to the total null space matrix like in Equation (6.19).

```
MatrixXd P_ext_unordered = ext_joint_nullspace_vector.back();
for (int i = ext_joint_nullspace_vector.size() - 2; i>=0; --i) {
  P_ext_unordered *= ext_joint_nullspace_vector[i];
}
```

In line 3, the total null space matrix $\underline{\underline{T}}_{\text{ext}}$ is assembled by multiplying the joint null space matrices together in the right order. The variable `P_ext_unordered` contains the keyword "unordered", because the rigid body degrees of freedom are ordered as prescribed by `rb_order` and not consecutively. Therefore, the rows of the total null space matrix are rearranged such that the standard degree of freedom ordering is obtained and the ordered null space matrix $\tilde{\underline{\underline{T}}}_{\text{ext}}$ can be used such that

$$\begin{pmatrix} \underline{t}_0 \\ \underline{t}_1 \\ \underline{t}_2 \end{pmatrix} = \tilde{\underline{\underline{T}}}_{\text{ext}} \cdot \begin{pmatrix} \underline{\Phi}_1 \\ \underline{\Phi}_0 \\ \underline{\Phi}_2 \end{pmatrix}. \tag{6.20}$$

6.4 Custom elements

To allow for additional elements in the multibody system, other than rigid bodies and joints, a very general interface is provided that describes arbi-

trary elements via their contribution to kinetic energy, potential energy and non-conservative generalised forces, all being functions of the multibody configuration $\underline{s}$, its time derivative $\dot{\underline{s}}$ and the control array $\underline{u}$. These additional contributions are automatically considered in the Lagrangian and the derivation of the discrete Euler-Lagrange-Equations via automatic differentiation. Via this interface, elements like springs (that only have a potential contribution), external forces (only non-conservative contributions) but also actuating muscle models can be added to the system. Note that the additional elements do not introduce new degrees of freedom as they rely on the existent degrees of freedom of the rigid bodies. However, they can add an arbitrary number of control variables to the system. These control variables are then automatically considered when recording the automatic differentiation tapes such that derivative information with respect to the control variables can be obtained. This is useful when solving optimal control problems.

As many additional elements (like springs or muscles) are connected to the system via two (end) points, a more specialised interface `TwoPointElement` is provided. This interface simplifies the definition of concerning elements, because the contributions of the new element to the system can be defined via these two points and derived quantities (like the length, the time derivative of the length, the midpoint, the midpoint velocity, ...) instead of the global configuration $\underline{s}$. In order to specify the two points, connectors that are defined in the local rigid body coordinate systems (see Section 6.1) are used.

6.4.1 The length of a two-point element and associated quantities

The length z of an element is obtained as the norm of the difference of the two connection points $\boldsymbol{a}_1$ and $\boldsymbol{a}_2$ in global coordinates, i.e.

$$z = ||\boldsymbol{a}_1 - \boldsymbol{a}_2||. \tag{6.21}$$

A connection point $\boldsymbol{a}_i$ is evaluated via

$$\boldsymbol{a}_i = \boldsymbol{\varphi}^j + \xi_1^i \boldsymbol{d}_1^j + \xi_2^i \boldsymbol{d}_2^j + \xi_3^i \boldsymbol{d}_3^j \tag{6.22}$$

for a rigid body j and the connector point in local coordinates

$$\boldsymbol{\xi}^i = \begin{pmatrix} \xi_1^i & \xi_2^i & \xi_3^i \end{pmatrix}^T. \tag{6.23}$$

The time derivative of the length z can be computed via the chain rule such that

$$\dot{z} = \left(\frac{\partial z}{\partial \boldsymbol{a}_1} \cdot \frac{\partial \boldsymbol{a}_1}{\partial \underline{s}} + \frac{\partial z}{\partial \boldsymbol{a}_2} \cdot \frac{\partial \boldsymbol{a}_2}{\partial \underline{s}} \right) \cdot \dot{\underline{s}}, \tag{6.24}$$

where the partial derivatives of z are given by

$$\frac{\partial z}{\partial \boldsymbol{a}_1} = \frac{\boldsymbol{a}_1 - \boldsymbol{a}_2}{z} \tag{6.25a}$$

$$\frac{\partial z}{\partial \boldsymbol{a}_2} = \frac{\boldsymbol{a}_2 - \boldsymbol{a}_1}{z}, \tag{6.25b}$$

respectively. The derivative of a connector point $\boldsymbol{a}_i$ with respect to the rigid body configuration $\underline{s}^j$ is given by

$$\frac{\partial \boldsymbol{a}_i}{\partial \underline{s}^j} = \begin{pmatrix} \mathbf{1} & \xi_1 \mathbf{1} & \xi_2 \mathbf{1} & \xi_3 \mathbf{1} \end{pmatrix} \quad \in \mathbb{R}^{3\times 12}, \tag{6.26}$$

and hence the derivative with respect to the total multibody configuration $\underline{s}$ reads

$$\frac{\partial \boldsymbol{a}_i}{\partial \underline{s}} = \begin{pmatrix} \dots & \underline{\mathbf{0}} & \frac{\partial \boldsymbol{a}_i}{\partial \underline{s}^j} & \underline{\mathbf{0}} & \dots \end{pmatrix} \quad \in \mathbb{R}^{3\times 12J}, \tag{6.27}$$

i.e. all entries are zero except the ones being associated with the rigid body coordinates $\underline{s}^j$. Note the analogy to the constraint Jacobian of the coupled system given in Equation (5.31). The midpoint of the two point element and its time derivative can be evaluated similarly to the previous calculation including the use of Equation (6.26).

6.4.2 Non-conservative contribution of a two-point element

Usually, non-conservative contributions are given by a generalised force array $\underline{f}^{\text{ext}}(t)$. This array, multiplied with the variation of the multibody system configuration $\delta \underline{s}$, yields the virtual work as shown in Equation (3.22). For the two point element, the generalised force is given by a scalar quantity f^{ext} and multiplication with the variation of the two-point element length δz yields the virtual work δW^{ext}, i.e.

$$\delta W^{\text{ext}} = f^{\text{ext}} \delta z. \tag{6.28}$$

In order to take such a two-point element contribution into account when the global generalised force vector is assembled, the variation of the two-point element δz has to be expressed in terms of the global variation $\delta \underline{s}$. This can be achieved by

$$\delta z = \frac{\partial z}{\partial \underline{s}} \cdot \delta \underline{s}, \tag{6.29}$$

where the derivative of z with respect to the configuration $\underline{s}$ can be written as

$$\frac{\partial z}{\partial \underline{s}} = \frac{\partial z}{\partial \boldsymbol{a}_1} \cdot \frac{\partial \boldsymbol{a}_1}{\partial \underline{s}} + \frac{\partial z}{\partial \boldsymbol{a}_2} \cdot \frac{\partial \boldsymbol{a}_2}{\partial \underline{s}}, \tag{6.30}$$

analogously to Equation (6.24). Therefore, the virtual work can be given by

$$\delta W^{\mathrm{ext}} = \underbrace{f^{\mathrm{ext}} \frac{\partial z}{\partial \underline{s}}}_{\underline{f}^{\mathrm{ext}}(t)} \cdot \delta \underline{s}, \tag{6.31}$$

with the global generalised force array

$$\underline{f}^{\mathrm{ext}}(t) = f^{\mathrm{ext}} \frac{\partial z}{\partial \underline{s}}. \tag{6.32}$$

This framework serves as a basis to implement a reduced artificial muscle model as a two-point element into MulDi. The reduced model is expected to drastically decrease the computational cost for the optimal control of kinematic systems that are actuated by artificial muscles.

7 An energy consistent viscoelastic lumped parameter model for dielectric elastomers

The finite element based simulation framework that is presented in Chapter 4 provides a powerful tool to solve electromechanically coupled and dynamic problems of arbitrary geometry, however, the computational cost is quite demanding. Therefore, so called lumped parameter models are used for complex tasks like solving optimal control problems where a multibody system is actuated by several muscles at the same time.

Lumped parameter models for dielectric elastomer actuators reduce the computational cost by assuming symmetry and uniform deformation. The most important property of dielectric elastomer actuators is the electrostatic pressure that arises from electric stimulation. For symmetric and unconstrained deformation of the actuator, the electrostatic pressure can be described via one-dimensional models. Section 7.1 gives an overview on commonly used models and their range of validity. Some of the assumptions usually made when deriving these models are modified to allow for a more general formulation without increasing the complexity too much.

In Section 7.2, this lumped electrostatic pressure model is extended with corresponding dynamic terms such as inertia and viscoelasticity and implemented into MulDi as a two point element. Lumped parameter models inevitably introduce an error to the simulation results. Quantifying this deviation is difficult as the lumped model is usually based on different modelling and time integration techniques compared to the three-dimensional counterpart, providing a different set of simulation parameters. In this work, the lumped parameter model is derived directly from the three-dimensional field theory within the framework of Lagrangian mechanics, including inertia terms and hyper-viscoelastic material behaviour. This allows for a consistent comparison between the lumped model and the corresponding three-dimensional finite element solution (from Chapter 5) in terms of performance and accuracy, which is illustrated by various numerical examples.

7.1 The electrostatic pressure in dielectric actuators

Large parts of this section are published in [Schl17]. A wide-spread lumped parameter model describing the electrostatic pressure p is presented by Pelrine et. al. in 1998 [Pelr98] and given by Equation (1.1). The fact that the electrostatic pressure present in a DEA is twice the pressure in a rigid plate capacitor is explained by the repelling of like charges within the electrodes. Because the elastomer is incompressible, the electrode surface area increases when the actuator contracts, releasing additional electric energy. In 2007, Wissler et. al. [Wiss07b] confirm this presumption by evaluating two-dimensional finite element simulations, finding electrostatic forces in 'in-plane' and 'out-of-plane' direction.

The electrostatic pressure given by Equation (1.1) is affected by the applied electric field strength e and by the relative permittivity ε_r of the material, also known as dielectric constant. The increase of the electric field strength e to gain a large electrostatic pressure is limited by manufacturing constraints [Lotz11, Reit16] as well as dielectric strength and instabilities [Xu10, Zhao07]. The relative permittivity plays a major role in the material selection and modelling. Remarkably enough, many researchers found that the dielectric constant ε_r is not constant at all, but decreasing with increasing pre-stretch of the material [Kofo03, Kofo08, Li11, Tröl13, Wiss07b]. From a physical point of view, polarisation within the dielectric material is responsible for the materials permittivity and in general, polarisation is deformation dependent [Land84].

In this section, first the common modelling approach for the electrostatic pressure that is based on the relative permittivity is presented in detail (Section 7.1.1). Then, the assumptions are modified to allow for a more general formulation (Section 7.1.2). Finally, the new model is validated with measurement data that is found in literature (Section 7.1.3), closing with a brief conclusion (Section 7.1.4).

7.1.1 Common modelling approach and inconsistencies

This section discusses the various assumptions that are implicitly and explicitly made in commonly used models and compares them to the actual requirements of DEAs. First, the consistency between three-dimensional Maxwell stress models and one-dimensional lumped parameter models is shown. Then, a possible derivation of Equation (1.1), based on the principle of virtual work, is presented in detail to provide a basis for the following modifications.

Maxwell stress, electrostriction and electrostatic pressure

The Maxwell stress tensor $\boldsymbol{\sigma}^{\text{elec}}$ describes the three-dimensional stress state within a dielectric material that is caused by an electric field. Yamwong et. al. 2002 [Yamw02] give this Maxwell stress as

$$\boldsymbol{\sigma}^{\text{elec}} = \varepsilon_0 \left(\frac{2\varepsilon_r - a_1}{2} \right) \boldsymbol{e} \otimes \boldsymbol{e} - \varepsilon_0 \boldsymbol{e} \cdot \boldsymbol{e} \left(\frac{\varepsilon_r + a_2}{2} \right) \mathbf{1}, \tag{7.1}$$

where a_1, a_2 are electrostrictive components. Electrostriction relates electrical and mechanical stored energy and hence is the reason for electromechanical coupling. Even though the main part of the cited work from Yamwong is about polar rubber (which is based on a different functional principle compared to DEAs), this basic equation is generally valid.

The electrostrictive components a_1, a_2 in Equation (7.1) arise from a few assumptions that are discussed in [Land84]. If the relationship between the electric displacement field and the electric field vector is linear and the material is homogeneous, the polarisation can be replaced by a tensor valued dielectric permeability. If it is further assumed that the displacement vector is small, neglecting higher order terms, the two electrostrictive coefficients a_1, a_2 of Equation (7.1) are obtained. Whereas some works consider the electrostrictive coefficients to be of importance [Shke96, Shke98], in many cases it is further (implicitly) assumed that the material is isotropic, resulting in only the scalar dielectric permittivity $\varepsilon = \varepsilon_0 \varepsilon_r$ introduced in Equation (1.1), without any further coefficients [Bers13, Kofo03, Kofo08, Pelr98].

If Equation (7.1) is evaluated without electrostrictive components ($a_1 = 0$, $a_2 = 0$) and for a unidirectional electric field $\boldsymbol{e} = \begin{pmatrix} 0 & 0 & e \end{pmatrix}^T$ acting in z-direction only, the Maxwell stress becomes

$$\boldsymbol{\sigma}^{\text{elec}} = \begin{pmatrix} -\frac{1}{2}\varepsilon_0 \varepsilon_r e^2 & 0 & 0 \\ 0 & -\frac{1}{2}\varepsilon_0 \varepsilon_r e^2 & 0 \\ 0 & 0 & \frac{1}{2}\varepsilon_0 \varepsilon_r e^2 \end{pmatrix}. \tag{7.2}$$

Because the DEA material is incompressible, its deformation state is independent of a superimposed hydrostatic pressure state. In other words, the atmospheric pressure has no effect on the material behaviour [Maco94]. The stress tensor

$$\hat{\boldsymbol{\sigma}}^{\text{elec}} = \boldsymbol{\sigma}^{\text{elec}} + \hat{p}\, \mathbf{1}, \tag{7.3}$$

with arbitrary pressure $\hat{p}$ leads to the same deformation state as $\boldsymbol{\sigma}^{\text{elec}}$ alone.

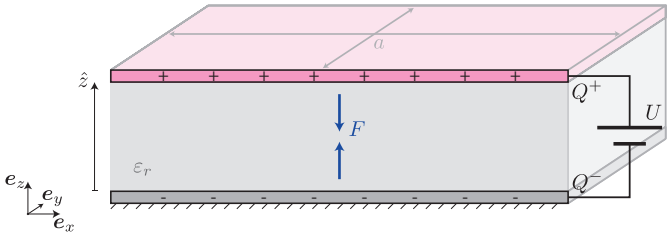

Figure 7.1: Lumped parameter model of DEA cell.

If $\hat{p}$ is chosen such that $\hat{p} = \frac{1}{2}\varepsilon_0\varepsilon_r e^2$, Equation (7.3) becomes

$$\hat{\boldsymbol{\sigma}}^{\text{elec}} = \begin{pmatrix} 0 & 0 & 0 \\ 0 & 0 & 0 \\ 0 & 0 & \varepsilon_0\varepsilon_r e^2 \end{pmatrix}. \tag{7.4}$$

The pressure in z-direction is now equivalent to the electrostatic pressure from Pelrine given in Equation (1.1). In practice, it does not make any difference whether the three-dimensional Maxwell stress (7.2) or only the scalar electrostatic pressure (1.1) is considered. Due to incompressibility, both stress states lead to the same deformation state.

Derivation of the electrostatic pressure with the principle of virtual work

The following derivation of the electrostatic pressure (1.1) is inspired by [Wiss07b], where the interaction between electrical and mechanical quantities is examined via the principle of virtual work. As illustrated in Figure 7.1, the two compliant electrodes with surface area $a(\hat{z})$ enclose the dielectric with permittivity ε_r. When a constant voltage U is applied, the electrodes get charged with the amount $Q(\hat{z})$, depending on the distance between the electrodes $\hat{z}$. The contractive force between the capacitor plates is assumed to be acting in z-direction only, with its z-component given by $F(\hat{z})$. All quantities are either constant or dependent on the distance $\hat{z}$ only, hence the dimension of the lumped parameter model is reduced to one degree of freedom. Moreover, all quantities are assumed to be quasi-static, neglecting any time dependent effects.

The unknown force $F(\hat{z})$ can be calculated by applying the principle of virtual work

$$\delta W^{\text{ext}}(\hat{z}) = \delta W^{\text{elec}}(\hat{z}) + \delta W^{\text{mech}}(\hat{z}), \tag{7.5}$$

requiring an infinitesimal amount of energy brought into the system via the external power supply $\delta W^{\mathrm{ext}}(\hat{z})$ to be identical with the change of energy stored in the system, separated into electrical energy $\delta W^{\mathrm{elec}}(\hat{z})$ and mechanical energy $\delta W^{\mathrm{mech}}(\hat{z})$. The individual energy contributions are given by

$$\delta W^{\mathrm{ext}}(\hat{z}) = U\,\delta Q(\hat{z}) \quad \text{with} \quad Q(\hat{z}) = C(\hat{z})\,U, \tag{7.6a}$$

$$\delta W^{\mathrm{elec}}(\hat{z}) = \frac{1}{2}\,\delta C(\hat{z})\,U^2 \quad \text{and} \tag{7.6b}$$

$$\delta W^{\mathrm{mech}}(\hat{z}) = -F(\hat{z})\,\delta\hat{z}, \tag{7.6c}$$

respectively, where $C(\hat{z})$ is the electric capacity of the system. For arbitrary capacity, (7.6) can be inserted into (7.5) and the contractive force becomes

$$F(\hat{z}) = -\frac{1}{2}\,U^2\,\partial_{\hat{z}} C(\hat{z}), \tag{7.7}$$

with $\partial_{\hat{z}} C(\hat{z})$ being the derivative of the capacity $C(\hat{z})$ with respect to $\hat{z}$. For the capacity of a parallel plate capacitor

$$C(\hat{z}) = \varepsilon_0 \varepsilon_r \frac{a(\hat{z})}{\hat{z}} \tag{7.8}$$

and constant volume $V = v = a(\hat{z})\,\hat{z}$ (due to the incompressibility of the dielectric and compliant electrodes), the derivative of the capacity becomes

$$\partial_{\hat{z}} C(\hat{z}) = -2\varepsilon_0 \varepsilon_r \frac{a(\hat{z})}{\hat{z}^2}. \tag{7.9}$$

Introducing the latter result into Equation (7.7), the contractive force is given as

$$F(\hat{z}) = \varepsilon_0 \varepsilon_r a(\hat{z}) \frac{U^2}{\hat{z}^2}. \tag{7.10}$$

Substituting the voltage with the electric field strength $U = e(\hat{z})\,\hat{z}$ and dividing the contractive force $F(\hat{z})$ by the electrode surface area $a(\hat{z})$, the electrostatic pressure (1.1) is obtained.

Note that in this derivation, constant voltage is assumed and for changing capacity, the power supply has to do work to maintain the voltage, as this is the case for many real world applications. However, the same electrostatic pressure (1.1) is obtained, if instead the charge Q is assumed to be constant, while the voltage then varies with changing capacity and no external power supply has to be considered. Even if both, the charge Q and the voltage U, are kept variable simultaneously, the resulting electrostatic pressure given by Equation (1.1) holds true.

Stretch dependent polarisation

In measurements concerning VHB 4910, the electrostatic pressure decreases with increasing pre-stretch of the material [Kofo03, Kofo08, Li11, Tröl13, Wiss07b]. This effect is not explained by Equation (1.1), where ε_r is constant. Even if the electrostrictive coefficients a_1, a_2 in Equation (7.1) are considered, they do not adequately explain the drop of the permittivity for large strains [Kofo03]. In the following paragraphs, assumptions that are made during the derivation of Equation (1.1) are identified and discussed.

In general, the spatial electric displacement field $\mathfrak{d}$ is defined by

$$\mathfrak{d} = \varepsilon_0 \boldsymbol{e} + \boldsymbol{p}^{\mathrm{pol}}, \tag{7.11}$$

where $\boldsymbol{p}^{\mathrm{pol}}$ is the spatial polarisation vector [Land84]. To obtain the electrostatic pressure given by Equation (1.1) (that is based on the capacity given by Equation (7.8)), the relative permittivity ε_r is introduced by replacing Equation (7.11) with

$$\mathfrak{d} = \varepsilon_0 \varepsilon_r \boldsymbol{e} \tag{7.12}$$

and hence assuming that

$$\boldsymbol{p}^{\mathrm{pol}} = \varepsilon_0 \boldsymbol{e}(\varepsilon_r - 1), \tag{7.13}$$

i.e. the polarisation is a linear function of the electric field. This assumption is justified with the fact that the applied electric fields are usually small [Land84]. However, this is questionable as the electric fields applied to DEAs are usually very large and close to the dielectric breakdown strength.

Moreover, a deformed body is not necessarily isotropic any more, even if it used to be in its undeformed state. This is important especially if pre-stretching of the DEA is considered, which is the case for many experiments, giving reason not to neglect electrostrictive components. In the following section, the derivation of the electrostatic pressure that is presented in Section 7.1.1 is generalised for arbitrary non-linear polarisation of the material, covering all electrostrictive effects.

7.1.2 Non-linear polarisation based approach

First, the derivation presented in Section 7.1.1 is generalised, leading to an electrostatic pressure formula that depends on the polarisation directly. Then, a general polarisation model that is based on invariants of the electromechanically

coupled problem is introduced. Finally, an example implementation illustrates the application of the derived formula. For the sake of readability, dependency on the electrode distance $\hat{z}$ is omitted. All quantities except for the constant voltage U and constant volume V depend on $\hat{z}$.

Polarisation based electrostatic pressure

In general, the capacity C describes the ratio between the charge Q and the applied voltage U

$$C = \frac{Q}{U}. \tag{7.14}$$

For arbitrary electrode geometry and charge distribution, the charge Q is calculated by integrating the electric displacement field $\mathfrak{d}$ over the surface such that

$$Q = \oint_a \mathfrak{d} \cdot d\boldsymbol{a}, \tag{7.15}$$

The voltage U can be obtained by integrating the electric field $\boldsymbol{e}$ over the line element $\boldsymbol{s}$

$$U = \int_s \boldsymbol{e} \cdot d\boldsymbol{s}. \tag{7.16}$$

For the symmetric capacitor geometry illustrated in Figure 7.1, $\mathfrak{d}$ is constant over the electrode area a and $\boldsymbol{e}$ is constant in between the electrodes such that Equation (7.14) becomes

$$C = \frac{d\,a}{e\,\hat{z}}, \tag{7.17}$$

where d is the z-component of the spatial electric displacement vector $\mathfrak{d} = \begin{pmatrix} 0 & 0 & d \end{pmatrix}^T$.

Next, the general definition of the electric displacement field given by Equation (7.11) is inserted, leading to the capacity

$$C = \left(\varepsilon_0 + \frac{p^{\mathrm{pol}}}{e} \right) \frac{a}{\hat{z}}. \tag{7.18}$$

Comparing coefficients with the capacity of a rigid plate capacitor given in Equation (7.8) gives rise to introduce the polarisation based capacity related permittivity

$$\tilde{\varepsilon}_C = 1 + \frac{p^{\mathrm{pol}}}{e\,\varepsilon_0} \tag{7.19}$$

that allows to write Equation (7.18) as

$$C = \varepsilon_0 \tilde{\varepsilon}_C \frac{a}{\hat{z}}. \tag{7.20}$$

Analogously to the derivation of Equation (7.9), assuming incompressibility and strain dependent polarisation $p^{\mathrm{pol}}(\hat{z})$, the derivative of the capacity now becomes

$$\partial_{\hat{z}} C = -2\varepsilon_0 \frac{a}{\hat{z}^2} + \frac{\partial_{\hat{z}} p^{\mathrm{pol}}}{U} a - \frac{p^{\mathrm{pol}}}{U} \frac{a}{\hat{z}}, \tag{7.21}$$

where $\partial_{\hat{z}} p^{\mathrm{pol}}$ is the derivative of p^{pol} with respect to $\hat{z}$. Inserting Equation (7.21) into Equation (7.7) to compute the mechanical force from the principle of virtual work and dividing by the surface area a then leads to the polarisation based electrostatic pressure

$$p = \varepsilon_0 e^2 - \frac{1}{2}\, \partial_{\hat{z}} p^{\mathrm{pol}}\, e\, \hat{z} + \frac{1}{2}\, p^{\mathrm{pol}}\, e. \tag{7.22}$$

Comparison with Pelrine's equation (1.1) yields the polarisation based force related permittivity

$$\tilde{\varepsilon}_F = 1 - \frac{1}{2\, e\, \varepsilon_0} \left(\hat{z}\, \partial_{\hat{z}} p^{\mathrm{pol}} - p^{\mathrm{pol}} \right) \tag{7.23}$$

that allows to write the polarisation based electrostatic pressure (7.22) as

$$p = \varepsilon_0\, \tilde{\varepsilon}_F\, e^2. \tag{7.24}$$

The electrostatic pressure is now dependent on the polarisation $p^{\mathrm{pol}}(\hat{z})$ of the material and hence allows for physically motivated strain dependency. In the following section, a general polarisation model is introduced.

General polarisation model

Electromechanically coupled, hyperelastic material models for incompressible and isotropic DEAs can be formulated based on five invariants (taken from Equation (4.33)), namely

$$I_1 = \boldsymbol{C} : \boldsymbol{1} \tag{7.25a}$$

$$I_2 = \frac{1}{2} \Big[(\boldsymbol{C} : \boldsymbol{1})^2 - \boldsymbol{C}^2 : \boldsymbol{1} \Big] \tag{7.25b}$$

$$I_3 = \boldsymbol{E} \cdot \boldsymbol{E} \tag{7.25c}$$

$$I_4 = \boldsymbol{E} \cdot \boldsymbol{C}^{-1} \cdot \boldsymbol{E} \tag{7.25d}$$

$$I_5 = \boldsymbol{E} \cdot \boldsymbol{C}^{-2} \cdot \boldsymbol{E}. \tag{7.25e}$$

Note that the commonly used invariant $\det(\boldsymbol{C})$ is omitted here, because the material is assumed to be incompressible, hence $\det(\boldsymbol{C}) = 1$. Equation (4.5a)

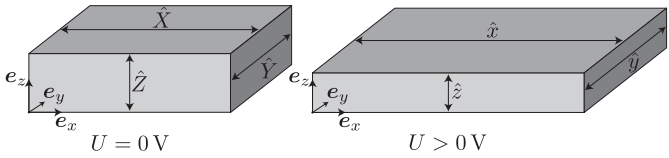

Figure 7.2: Deformation of DEA cell due to an applied voltage.

links the material electric field vector $\boldsymbol{E}$ with the spatial electric field vector $\boldsymbol{e}$. Note that for the sake of simplicity, the invariants are renumbered within this chapter as compared with Equation (4.33)).

If the coupled incompressible hyperelastic material model is given as a (generally non-linear) material free energy density function based on the introduced invariants

$$\Phi(I_1, \ldots, I_5), \tag{7.26}$$

then the spatial polarisation vector is obtained by

$$\boldsymbol{p}^{\mathrm{pol}} = -\boldsymbol{F} \cdot \partial_{\boldsymbol{E}} \Phi, \tag{7.27}$$

which evaluates to

$$\boldsymbol{p}^{\mathrm{pol}} = -2\boldsymbol{F} \cdot \left(\partial_{I_3} \Phi \; \mathbf{1} + \partial_{I_4} \Phi \; \boldsymbol{C}^{-1} + \partial_{I_5} \Phi \; \boldsymbol{C}^{-2} \right) \cdot \boldsymbol{E}. \tag{7.28}$$

Next, the deformation gradient for the lumped parameter model of the DEA cell is investigated. Figure 7.2 shows the DEA cell in its reference state on the left hand side and in its actuated state on the right hand side. It is assumed that the DEA cell is a square cuboid with edge length $\hat{X} = \hat{Y}$ and thickness $\hat{Z}$. In the deformed state, the edge length is given by $\hat{x} = \hat{y}$ and the thickness is $\hat{z}$, while the volume $V = \hat{x}\,\hat{y}\,\hat{z} = \hat{X}\,\hat{Y}\,\hat{Z}$ is constant. This setting allows for the introduction of a single dimensionless deformation quantity $\Lambda = {}^{\hat{z}}/_{\hat{Z}}$ such that the deformation gradient is given by

$$\boldsymbol{F} = \begin{pmatrix} \sqrt{\Lambda^{-1}} & 0 & 0 \\ 0 & \sqrt{\Lambda^{-1}} & 0 \\ 0 & 0 & \Lambda \end{pmatrix}. \tag{7.29}$$

Introducing this deformation gradient as well as the material electric field vector

$$\boldsymbol{E} = \begin{pmatrix} 0 & 0 & \frac{U}{\hat{Z}} \end{pmatrix}^T \tag{7.30}$$

into Equation (7.28), the deformation specific spatial polarisation vector $\boldsymbol{p}^{\mathrm{pol}} = \begin{pmatrix} 0 & 0 & p^{\mathrm{pol}} \end{pmatrix}^T$ is obtained, with its z-component given by

$$p^{\mathrm{pol}} = -2\frac{U}{\hat{Z}}\left(\Lambda\ \partial_{I_3}\Phi + \Lambda^{-1}\ \partial_{I_4}\Phi + \Lambda^{-3}\ \partial_{I_5}\Phi\right). \tag{7.31}$$

Finally, the deformation specific polarisation vector from Equation (7.31) can be introduced into Equation (7.22), such that the electrostatic pressure evaluates to

$$\begin{aligned} p = e^2\Big(&\varepsilon_0 - 2\ \partial_{I_4}\Phi - 4\Lambda^{-2}\ \partial_{I_5}\Phi\Big) \\ &+E^2\Big(\Lambda\ \partial_\Lambda(\partial_{I_3}\Phi) + \Lambda^{-1}\ \partial_\Lambda(\partial_{I_4}\Phi) + \Lambda^{-3}\ \partial_\Lambda(\partial_{I_5}\Phi)\Big). \end{aligned} \tag{7.32}$$

In the next section, the electrostatic pressure is evaluated for an example energy function.

Linear energy approach

Is it assumed that the free energy density (7.26) is a linear function with respect to the invariants concerning electrical contributions, such that

$$\Phi(I_1, \ldots, I_5) = \Phi_{\mathrm{mech}}(I_1, I_2) + c_1 I_3 + c_2 I_4 + c_3 I_5, \tag{7.33}$$

where Φ_{mech} represents a purely mechanical material model. As the electrostatic pressure (7.32) only depends on electromechanical coupling terms, material parameters for purely mechanical material models are irrelevant here. Even purely electrical contributions like $c_1 I_3$ will have no effect on the electrostatic pressure which evaluates to

$$p = e^2\left(\varepsilon_0 - 2c_2 - 4\Lambda^{-2}c_3\right). \tag{7.34}$$

Comparison of the coefficients of the previous equation with (1.1) leads to the polarisation based force related permittivity (7.23) that in this case is given as

$$\tilde{\varepsilon}_F = 1 - 2\frac{c_2}{\varepsilon_0} - 4\frac{c_3}{\varepsilon_0}\Lambda^{-2}. \tag{7.35}$$

Introducing new coefficients $\bar{c}_2 = -2\,{}^{c_2}\!/_{\varepsilon_0}$ and $\bar{c}_3 = 2\,{}^{c_3}\!/_{\varepsilon_0}$, the permittivity becomes

$$\tilde{\varepsilon}_F = 1 + \bar{c}_2 - 2\bar{c}_3\Lambda^{-2}. \tag{7.36}$$

Note that this permittivity only relates to the electrostatic pressure, whereas the capacity related permittivity (7.19) is also affected by parameter c_1, i.e.

$$\tilde{\varepsilon}_C = 1 + \bar{c}_1\Lambda^2 + \bar{c}_2 - \bar{c}_3\Lambda^{-2}, \tag{7.37}$$

where $\bar{c}_1 = -2\,c_1/\varepsilon_0$. This allows to separate force measurement data from capacity measurement data.

Equations (7.36) and (7.37) clearly show the strain dependency of the 'dielectric constant'. With increasing stretch ($\hat{z} < \hat{Z}$), the strain $\Lambda = \hat{z}/\hat{Z}$ is decreasing and hence, for $\bar{c}_3 > 0$, the permittivity is decreasing as well. For the material model chosen in this example, the permittivity depends on the strain quadratically.

Note that for the special case where the free energy function is given as

$$\Phi(I_1, \ldots, I_5) = \Phi_{\text{mech}}(I_1, I_2) - \frac{1}{2}\varepsilon_0(\varepsilon_r - 1)I_4, \tag{7.38}$$

the simplified polarisation approach given in Equation (7.13) is recovered. The polarisation is then independent of the deformation gradient introduced in Equation (7.29). It further follows that the polarisation based capacity related permittivity (7.19) and the polarisation based force related permittivity (7.23) are identical, i.e. $\tilde{\varepsilon}_C = \tilde{\varepsilon}_F = \varepsilon_r$, such that Pelrine's Equation (1.1) is obtained. Hence the free energy approach (7.38) covers the existing theory including Pelrine's electrostatic pressure and the dielectric constant as a special case.

7.1.3 Validation with measurement data from literature

The permittivity model introduced in the previous section is compared to measurement data that is found in literature. This section is divided into two parts, where the first part covers permittivity data that is based on blocked force measurements, and the second part covers permittivity data that is based on capacity measurements of DEAs.

Force related permittivity

In 2003, Kofod et. al. [Kofo03] performed blocked force measurements of thin DEA membranes made of VHB 4910 acrylic tape. The electrostatic pressure is indirectly measured via the normal stress difference, which, according to Kofod, equals the electrostatic pressure. The dielectric permittivity is evaluated using Pelrine's equation (1.1) for three different pre-stretch states. It can be observed that the dielectric constant drops with increasing pre-stretch of the membrane actuator. This drop is not explained by Equation (1.1).

While the in-plane pre-stretch orthogonal to the measurement direction is kept constant at $\Lambda_x = \hat{x}/\hat{X} = 6$, the pre-stretch in measurement direction $\Lambda_y = \hat{y}/\hat{Y}$

Table 7.1: Relative permittivity of 3M VHB 4910 measured by Kofod [Kofo03].

Λ	ε_r
$0.041\overline{6}$	4.089
$0.0\overline{3}$	3.807
$0.02\overline{7}$	3.572

Table 7.2: Relative permittivity of 3M VHB 4910 at 100 Hz measured by Wissler [Wiss07b].

Λ	ε_r
1.0	4.68
$0.\overline{1}$	3.71
0.0625	3.34
0.04	2.62

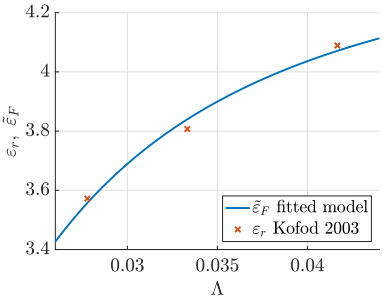

Figure 7.3: Relative permittivity measured by Kofod [Kofo03] and model fit based on Equation (7.36).

is set to $\Lambda_y = 4, \Lambda_y = 5$ and $\Lambda_y = 6$. The associated dielectric constant is given in per cent of the the manufacturer's specification of $\varepsilon_r = 4.7$ with 87 %, 81 % and 76 %. Due to the material's incompressibility, the measurement data can be converted to a strain in thickness direction of the membrane via $\Lambda = (\Lambda_x \Lambda_y)^{-1}$. Table 7.1 summarises Kofod's results.

Because the permittivity is here evaluated based on force measurements, Kofod's data is compared to the model given by Equation (7.36). Using a non-linear least squares trust-region algorithm provided by MATLAB's curve fitting toolbox, the model's parameters are identified as $\bar{c}_2 \approx 3.482$ and $\bar{c}_3 \approx 3.568 \cdot 10^{-4}$. Figure 7.3 compares the obtained permittivity model to the measurement data. Even though there are only three measurement points available to fit a model with two parameters, the fit is of a very good quality given that the polarisation is based on a very simple free energy function (see Section 7.1.2).

Table 7.3: Relative permittivity of 3M VHB 4910 at 0.5 Hz measured by Li [Li11].

Λ	ε_r
1.0	4.5
$0.\overline{4}$	3.65
0.25	3.25
0.16	2.75
$0.\overline{1}$	3.25
0.0816	2.5
0.0625	1.75

Table 7.4: Relative permittivity of 3M VHB 4910 at 1 Hz measured by Tröls [Tröl13].

Λ	ε_r
1.0	4.24
$0.\overline{1}$	3.83
0.04	3.44

Capacity related permittivity

Measuring the capacity of DEAs is easier than obtaining blocked actuation forces and hence more capacity related measurements are found in literature. Wissler [Wiss07b] took measurements of a symmetrically stretched circular DEA membrane made of VHB 4910 using the 4263B LCR-meter from Agilent. The given stretch ratios Λ_p are associated with the radial diameter change of the membrane. Due to incompressibility of the material, the given stretch Λ_p is connected to the stretch in thickness direction Λ used in this work via $\Lambda = \Lambda_p^{-2}$. Table 7.2 summarises Wissler's results for LCR-measurements at 100 Hz.

Li [Li11] also took measurements of DEAs with circular shaped electrodes, however, the VHB 4910 membranes were stretched biaxially in a frame, before the capacity was measured. The in-plane stretch ratios are given by Λ_1^p and Λ_2^p. Only measurements associated with symmetrically pre-stretched membranes where $\Lambda_1^p = \Lambda_2^p = \Lambda_p$ are considered in this work and given in Table 7.3.

Finally, Tröls [Tröl13] measured the capacity of symmetrically stretched DEAs with a Novocontrol broadband dielectric spectrometer. The given radial stretch ratios are again converted to the stretch in membrane thickness and the results are presented in Table 7.4 for 1 Hz measurements. The measurement data of all three authors is summarised in Figure 7.4. It can be seen that there is a large variation between data provided in different papers. Reason for this deviation might be the viscoelastic behaviour of VHB 4910 that explains a time dependence of the stress-strain relation of the material, which is more pronounced for larger deformation (small Λ). Therefore, Li [Li11] took measurements only seven days after pre-stretching, whereas the other

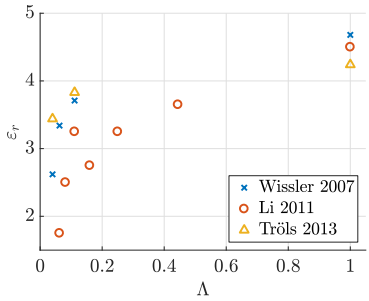

Figure 7.4: Relative permittivity of VHB 4910 measured by various authors via capacity [Li11, Tröl13, Wiss07b].

Table 7.5: Model fit parameters for capacity based measurements.

	$\bar{c}_1$	$\bar{c}_2$	$\bar{c}_3$
Wissler 2007	0.8285	2.854	$1.981 \cdot 10^{-3}$
Li 2011	1.1820	2.334	$5.793 \cdot 10^{-3}$
Tröls 2013	0.3576	2.883	$7.098 \cdot 10^{-4}$

authors did not mention any waiting time. Another reason might be different measurement devices, different measuring electrodes and different measuring frequencies. Finally, the individual stretching frames might lead so slightly different stretch ratios.

Consequently, the measurement data is fitted to the capacity based permittivity model given by Equation (7.37) for individual data sources separately. The parameters $\bar{c}_1, \bar{c}_2$ and $\bar{c}_3$ are again identified using MATLAB's non-linear least squares trust-region algorithm and presented in Table 7.5. Figure 7.5 compares the fitted models with the measurement data. The individual parameters vary between different authors as expected because the measurement data is inconsistent as well. This holds especially for parameter $\bar{c}_1$. Parameter $\bar{c}_2$ however, shows consistent tendency, while $\bar{c}_3$ is relatively small in all cases compared to $\bar{c}_1$ and $\bar{c}_2$. Unsurprisingly, the fit in Figure 7.5c is perfect, as only three measurement points are available to fit the three parameters of the model. But the qualitative curve progression is still consistent with the other fits. Finally, the fit in Figure 7.5a is of remarkable quality.

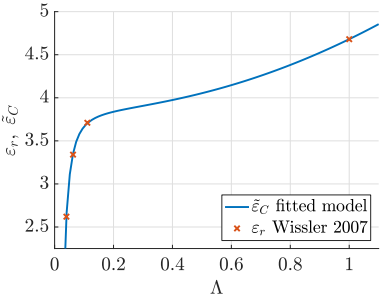

(a) Wissler [Wiss07b]

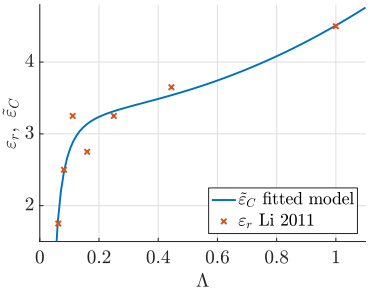

(b) Li [Li11]

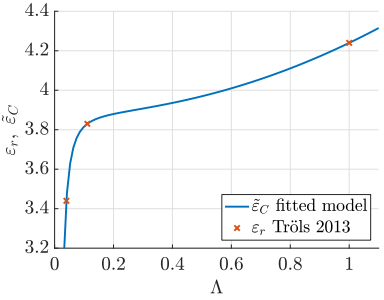

(c) Tröls [Tröl13]

Figure 7.5: Relative permittivity from capacity measurements and model fit based on Equation (7.37).

7.1.4 Conclusions

For many elastomers such as silicones or natural rubber, the material's permittivity seems to be unaffected by an imposed pre-stretch [Tröl13]. However, this is not the case for acrylic materials such as VHB 4910, where the relative permittivity drops with increasing stretch. As these materials are often used to build dielectric elastomer actuators, a suitable material model is required, describing the stretch dependent electrostatic pressure. The well known electrostatic pressure model from Pelrine et. al. can not give a physically motivated reason for this behaviour, because implicitly, the polarisation of the material is assumed to be linear in the electric field strength, as shown in Section 7.1.1.

In this work, Pelrine's approach is modified to allow for a more general polarisation field, resulting in a polarisation dependent electrostatic pressure, where the contractive force directly depends on the material's polarisation and its derivative with respect to deformation. Additionally, a general polarisation model is derived from three-dimensional electromechanically coupled field theory, based on invariants of the coupled problem. The combination of both, the polarisation dependent electrostatic pressure and the polarisation model, yields a physically motivated and stretch dependent formulation for the contractive force within a dielectric elastomer actuator.

Comparison of the new formulation with Pelrine's approach provides the identification of a polarisation based capacity related permittivity $\tilde{\varepsilon}_C$ as well as a polarisation based force related permittivity $\tilde{\varepsilon}_F$ of the material. Both quantities depend on the material's deformation and drop with increasing pre-stretch. It should be noted that $\tilde{\varepsilon}_C$ and $\tilde{\varepsilon}_F$ differ from each other. This allows and requires to handle parameter identification based on force measurement data and capacity related measurements individually.

The new formulation allows for any (non-linear) electromechanically coupled hyperelastic material approach and is thus very flexible. It is shown that if the free energy function is chosen appropriately, Pelrine's model (that is appropriate to model the silicone used in this work) including the well established concept of the dielectric constant ε_r is covered as a special case of the new formulation. Comparison of the new formulation to measurement data that is found in literature gives remarkably good results, even for the simple material model that is presented in Equation (7.33). It can be concluded that the new approach presented in this work gives a physically motivated explanation of the stretch dependent permittivity of dielectric elastomers.

In the following section, the electrostatic pressure model for dielectric actuators

is extended with dynamic terms such that it can be used in a forward dynamics simulation.

7.2 Energy consistent viscoelastic model for assumed deformation

The electromechanically coupled model for dielectric elastomers being used in this work is based on a continuous Lagrangian, from which the equations of motion are derived. Because for arbitrary settings the equations of motion can not be solved analytically, the system is discretised in space via finite elements and in time via a variational integration scheme (see Chapter 4). In this section, the spatial finite element discretisation is replaced by a lumped parameter approach, where a parametrised deformation gradient represents a reduced set of possible deformations. The deformation gradient is parametrised such that it covers the assumed deformation of a symmetric and free actuator with uniaxial electric stimulation. The number of degrees of freedom of the actuator is then reduced to the number of parameters of the deformation gradient, which in this case is just one parameter that corresponds to the length of the actuator. As both models, the finite element approach and the lumped parameter approach, consequently share the same modelling basis and hence material parameters, they can be easily compared and used side by side. The more the assumed deformation of the lumped parameter model deviates from the 'real' deformation (that is approximated by the finite element model), the larger is the error of the lumped model. If the assumed deformation exactly matches the real deformation, then no error is introduced at all. The Lagrangian of the lumped parameter model is then identical to the continuous Lagrangian and the simulation results are "energy consistent".

First, an elastic energy potential for the lumped parameter model is derived and investigated for the static case. Then, dynamic contributions are added to allow for forward dynamics simulations.

7.2.1 Uniaxial elastic energy potential

In accordance to the deviation of the electrostatic pressure in Section 7.1, the actuator is presumed to have a quadratic cross section area and deforms symmetrically as illustrated in Figure 7.2. For this deformation, the deformation gradient is given by Equation (7.29). Inserting this deformation gradient into

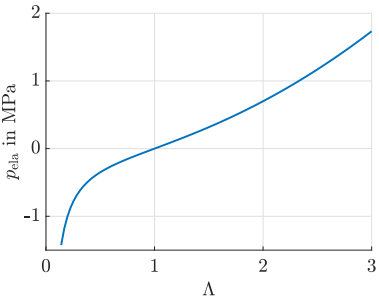

Figure 7.6: Neo-Hookean stress as a function of uniaxial stretch Λ for $\mu = 0.2\,\mathrm{MPa}$.

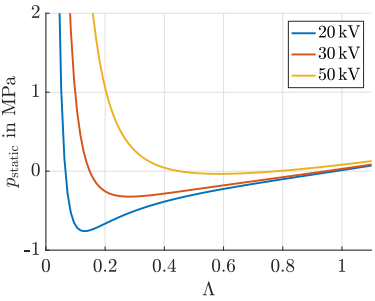

Figure 7.7: Sum of mechanical pressure and electrostatic pressure in MPa as a function of the strain Λ.

the mechanical energy model given by Equation (2.20) yields the strain energy density

$$\Phi_{\mathrm{ela}} = \frac{\mu}{2}\left(\frac{2+\Lambda^3-3\Lambda}{\Lambda}\right) \tag{7.39}$$

that can now be expressed in terms of the scalar strain Λ. The potential energy is obtained by integrating the strain energy density over the volume of the geometry such that

$$\Pi_{\mathrm{ela}} = \int_{\mathcal{B}_0} \Phi_{\mathrm{ela}}\, dV. \tag{7.40}$$

Because the deformation gradient and hence the strain energy are spatially constant, this integral simplifies to

$$\Pi_{\mathrm{ela}} = \Phi_{\mathrm{ela}} V. \tag{7.41}$$

The mechanical force F_{ela} that originates from the elastic potential is obtained by deriving the strain energy with respect to the actuator length $\hat{z}$. This force, divided by the cross section area a gives the mechanical pressure

$$p_{\mathrm{ela}} = \frac{F_{\mathrm{ela}}}{a} = \mu\left(\Lambda^2 - \Lambda^{-1}\right). \tag{7.42}$$

Figure 7.6 illustrates the mechanical pressure p_{ela} in MPa for $\mu = 0.2\,\mathrm{MPa}$. The curve shape illustrates the typical behaviour of Neo-Hookean materials [Ali10]. Under compression ($\Lambda < 1$), the material becomes stiff very quickly. Under expansion ($\Lambda > 1$) the material stays soft and stiffens only slowly.

The static equilibrium of the dielectric actuator is obtained by solving

$$p_{\mathrm{static}} = p_{\mathrm{ela}} + p = 0, \tag{7.43}$$

where p is the electrostatic pressure given by Equation (1.1). With $\mu = 0.2\,\mathrm{MPa}, \varepsilon_r = 3.7$ and an initial actuator length, respectively, membrane thickness of $\hat{Z} = 1\,\mathrm{mm}$, p_{static} is plotted as a function of Λ for different voltages U in Figure 7.7. It can be observed that besides the usual equilibrium where $\Lambda > 0.5$, there is another equilibrium point ($p_{\mathrm{static}} = 0$) for very small Λ. The usual equilibrium point (for $\Lambda > 0.5$) decreases with increasing voltage, i.e. higher voltages lead to a larger compression. If the voltage exceeds a certain limit, no equilibrium can be achieved any more, the contractive effect reinforces itself and instability occurs. This behaviour is consistent with the non-linear effect that is observed in the numerical example in Section 5.4.3 and also found in literature [Xu10].

7.2.2 Kinetic energy

In order to solve forward dynamics problems and compare the results of the lumped parameter model to finite element simulations, the static pressure p_{static} must be extended with inertia terms and viscoelastic contributions. With the kinetic energy density from Equation (2.29), the kinetic energy can be obtained by

$$T = \frac{1}{2}\rho_0 \int_{\mathcal{B}_0} \dot{\boldsymbol{x}}^2 \, dV \tag{7.44}$$

for homogeneous materials. The assumed deformation field that corresponds to the deformation gradient (7.29) is given by

$$x_1 = X_1 \frac{\hat{x}}{\hat{X}} = X_1 \sqrt{\Lambda^{-1}} \tag{7.45a}$$

$$x_2 = X_2 \frac{\hat{y}}{\hat{Y}} = X_2 \sqrt{\Lambda^{-1}} \tag{7.45b}$$

$$x_3 = X_3 \frac{\hat{z}}{\hat{Z}} = X_3 \Lambda, \tag{7.45c}$$

if it is further assumed that the material accelerates symmetrically during deformation, i.e. there is a centre line along the longitudinal muscle axis that is at rest. Equation (7.44) then becomes

$$T = \frac{1}{2}\rho_0 \int_{-\frac{\hat{Z}}{2}}^{\frac{\hat{Z}}{2}} \int_{-\frac{\hat{Y}}{2}}^{\frac{\hat{Y}}{2}} \int_{-\frac{\hat{X}}{2}}^{\frac{\hat{X}}{2}} \dot{\boldsymbol{x}}^2 \, dx \, dy \, dz \tag{7.46}$$

that, after some calculation evaluates to

$$T = \frac{1}{48} m \dot{\hat{z}}^2 \left(V \hat{z}^{-3} + 2 \right), \tag{7.47}$$

where m is the mass and V the (constant) volume of the artificial muscle. Note that the origin of coordinates is located in the midpoint of the actuator cube when evaluating Equation (7.46) and the obtained expression (7.47) is equal to the derivation found in [Xu12].

7.2.3 Viscoelastic contributions

Inserting the deformation gradient (7.29) and its time derivative

$$\dot{\boldsymbol{F}} = \begin{pmatrix} -\frac{1}{2}\sqrt{\hat{Z}}\hat{z}^{-\frac{3}{2}}\dot{\hat{z}} & 0 & 0 \\ 0 & -\frac{1}{2}\sqrt{\hat{Z}}\hat{z}^{-\frac{3}{2}}\dot{\hat{z}} & 0 \\ 0 & 0 & \hat{Z}^{-1}\dot{\hat{z}} \end{pmatrix} \tag{7.48}$$

into the viscoelastic stress model (2.24), it follows that

$$\boldsymbol{P}^{\mathrm{vis}} = \eta\dot{\hat{z}} \begin{pmatrix} -\frac{1}{2\sqrt{\hat{Z}\hat{z}}} & 0 & 0 \\ 0 & -\frac{1}{2\sqrt{\hat{Z}\hat{z}}} & 0 \\ 0 & 0 & \frac{\hat{Z}}{\hat{z}^2} \end{pmatrix}. \tag{7.49}$$

The virtual viscoelastic work is given by

$$\delta W^{\mathrm{vis}} = \int_{\mathcal{B}_0} \delta\boldsymbol{F} : \boldsymbol{P}^{\mathrm{vis}}\, dV, \tag{7.50}$$

where

$$\delta\boldsymbol{F} = \frac{\partial\delta\boldsymbol{x}}{\partial\boldsymbol{X}} \tag{7.51}$$

and

$$\delta\boldsymbol{x} = \begin{pmatrix} -\frac{1}{2}X_1\hat{Z}^{\frac{1}{2}}\hat{z}^{-\frac{3}{2}} \\ -\frac{1}{2}X_2\hat{Z}^{\frac{1}{2}}\hat{z}^{-\frac{3}{2}} \\ X_3\hat{Z}^{-1} \end{pmatrix}\delta\hat{z}, \tag{7.52}$$

such that the virtual work (7.50) can be given as

$$\delta W^{\mathrm{vis}} = -\frac{3}{2}\eta V\frac{\dot{\hat{z}}}{\hat{z}^2}\delta\hat{z}. \tag{7.53}$$

Note that again, the deformation gradient and hence the viscoelastic stress (7.49) are constant within the volume $\mathcal{B}_0$ and the integral in (7.50) is easily computed.

7.2.4 Uniaxial electromechanically coupled energy potential

As for commonly used silicones, the relative permittivity is constant and does not vary for different strains as it is the case for acrylic materials (see Section 7.1.4), the energy approach from Equation (7.38) is utilised, leading to Pelrine's electrostatic pressure formula (1.1). With the deformation gradient (7.29) and an electric field acting in longitudinal z-direction of the artificial muscle only, the fourth invariant (7.25d) becomes

$$I_4 = \frac{U^2}{\hat{z}^2} \tag{7.54}$$

and the polarisation energy can be given by

$$\Pi_{\text{ele, pol}} = -\frac{1}{2} V \varepsilon_0 (\varepsilon_r - 1) \frac{U^2}{\hat{z}^2}. \tag{7.55}$$

Together with the free space contribution (compare to Equation (4.34))

$$\Pi_{\text{ele, free}} = -\frac{1}{2} V \varepsilon_0 \frac{U^2}{\hat{z}^2}, \tag{7.56}$$

the total electrical energy becomes

$$\Pi_{\text{ele}} = \Pi_{\text{ele, pol}} + \Pi_{\text{ele, free}} = -\frac{1}{2} V \varepsilon_0 \varepsilon_r \frac{U^2}{\hat{z}^2}. \tag{7.57}$$

The individual energy contributions can be composed to a Lagrangian such that

$$L(\hat{z}, \dot{\hat{z}}) = T - \Pi_{\text{ela}} - \Pi_{\text{ele}}, \tag{7.58}$$

with T from Equation (7.47), Π_{ela} from Equation (7.41) and Π_{ele} from Equation (7.57). Note that the Lagrangian is now a function of only $\hat{z}$ and $\dot{\hat{z}}$. Scalar non-conservative contributions that are introduced in (6.28) and further specified in (7.53) are given by

$$f^{\text{ext}} = -\frac{3}{2} \eta V \frac{\dot{\hat{z}}}{\hat{z}^2}. \tag{7.59}$$

7.2.5 Performance analysis

First, simulations of the isolated actuator lumped parameter model are compared to simulation results of corresponding finite element models. Then, the lumped parameter model is implemented into MulDi (as a two-point element) and the accuracy of simulation results for dielectric elastomer actuated multibody systems is explored.

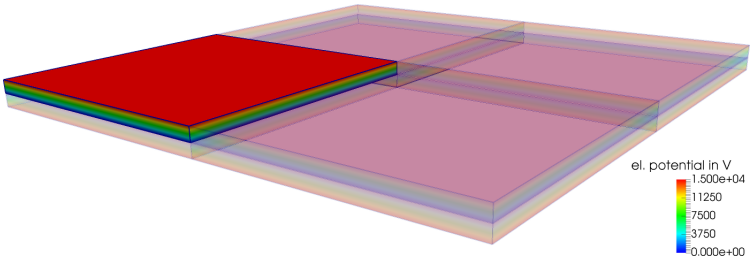

Figure 7.8: Coarse finite element mesh of a thin membrane with symmetry constraints.

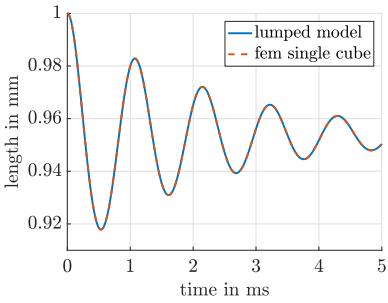

Figure 7.9: Comparison between the lumped DEA model and finite element simulation results for a square actuator.

Verification via a dielectric elastomer membrane

The first example geometry is a 1 mm thick square silicone membrane with an edge length of 20 mm and electrodes at the top and at the bottom. The relative permittivity is set to $\varepsilon_r = 3.7$ and for the damping parameter, a small value of $\eta = 0.01\,{}^{\mathrm{g}}/_{\mathrm{ms\,mm}}$ is used. A constant voltage is applied to the electrodes such that the initial electric field strength within the membrane is given by $E = 30\,{}^{\mathrm{kV}}/_{\mathrm{mm}}$. The forward dynamics behaviour of the membrane is simulated for 5 ms with a time step size of $\Delta t = 0.01$ ms. Due to symmetry, the finite element model covers only a part of the problem as illustrated in Figure 7.8. Appropriate symmetry boundary conditions avoid rigid body motion. In Figure 7.9, the simulation results from the finite element model concerning the thickness of the membrane versus time are compared to the corresponding results from the lumped parameter model. As the expansion of the membrane is not constrained at all, the deformation gradient in the finite

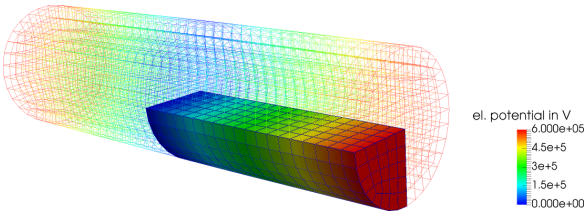

Figure 7.10: Finite element model of a long actuator with symmetry constraints.

element model exactly matches the parametrised deformation gradient from the lumped parameter model. Therefore, the simulation results are identical. This verifies the derived energy contributions for the lumped parameter model.

Long round actuator with slight damping

The second example is a long round actuator with a length of 40 mm and a diameter of 1 cm with the same material properties as in the example before. The voltage is applied such that the initial electric field strength equals $E = 30\,\mathrm{kV/mm}$. Most of the energy contributions in the Lagrangian of the lumped parameter model (7.58) are independent of the cross section area shape of the dielectric actuator, only the kinetic energy differs. Assuming a symmetric deformation for the round actuator, where the diameter increases during contraction such that the volume is preserved, the kinetic energy can be integrated in cylinder coordinates and becomes

$$T = \frac{1}{48} m \dot{\hat{z}}^2 \left(\frac{3}{\pi} V \hat{z}^{-3} + 2 \right). \tag{7.60}$$

Note that a comparison with the kinetic energy of the square actuator (7.47) reveals that the only difference is the factor of $3/\pi$ that appears in the kinetic energy of the round model.

The finite element model that is used for comparison with the lumped parameter model is illustrated in Figure 7.10. Again, to save computational cost and to avoid rigid body motion, only a part of the actuator is meshed and used to run the simulation, while corresponding symmetry boundary conditions are applied. The finite element mesh is now much finer than in the previous example. In Figure 7.11a the actuator length versus time is compared between the finite element model and the lumped parameter model. Even though the

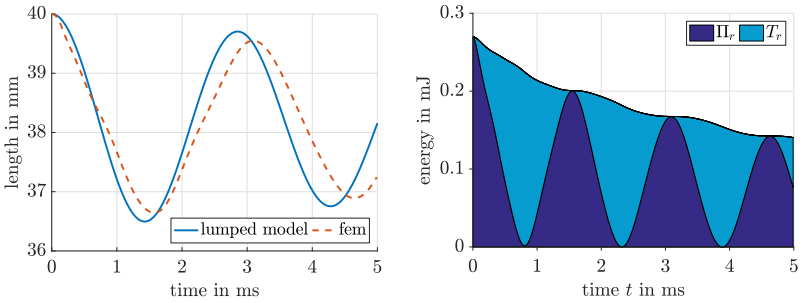

(a) Length vs. time.

(b) Energy oscillations.

Figure 7.11: Comparison of the lumped model to finite element simulation results for a long round actuator.

general behaviour of the lumped model is of acceptable quality, there are some differences in length as well as frequency of the oscillation. These differences result from high frequency oscillations in the finite element mesh. The energy of the finite element model is illustrated in Figure 7.11b. It can be observed that the kinetic energy slightly oscillates with a high frequency. The finite element mesh with its fine resolution allows to resolve and transport these oscillations, whereas the lumped parameter model assumes homogeneous deformation.

Long round actuator with realistic viscoelastic behaviour

If the unconstrained contraction of a real stacked dielectric elastomer actuator is observed, no oscillations are present at all. When a voltage is applied, the actuator quickly approaches its contracted steady state without overshooting. It is therefore assumed that in reality, viscoelastic effects play a major role compared to inertia terms.

If the viscoelastic damping parameter in the long round actuator simulation model is increased to $\eta = 0.5\,\mathrm{g/ms\,mm}$, critical damping is exceeded and oscillations have vanished. Figure 7.12 shows the simulations results for the model with increased damping. Here, the lumped parameter model performs quite well and there is almost no difference in the length prediction of the two models.

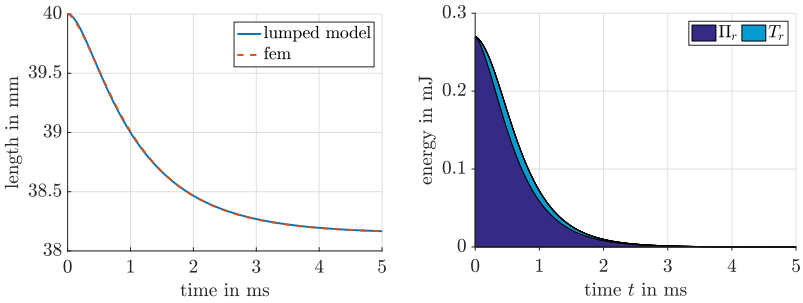

(a) Length vs. time.

(b) Energy.

Figure 7.12: Comparison of the lumped model to finite element simulation results for a long round actuator with increased damping.

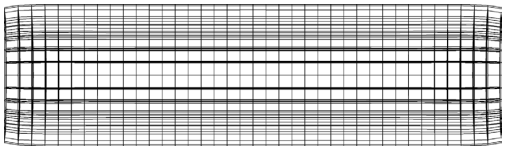

Figure 7.13: Deformed finite element mesh of the contracted state of a 4 cm long round muscle with clamped ends.

Clamped actuator

If the artificial muscle is used to actuate multibody systems, its motion is constrained due to rigid body coupling constraints as described in Section 5.2. This applies in particular to the ends of the muscle, where the expansion of the cross section area is hindered. To make this effect visible, the finite element simulation of the previous example (same parameters and $\eta = 0.5\,\mathrm{g/ms\,mm}$) is extended with additional constraints. The finite element nodes at both ends of the muscle are only allowed to move along the longitudinal axis of the actuator, whereas the motion within the cross section area is constrained. As the influence of this constraint on the muscle behaviour grows with increasing contraction, the applied voltage is adapted (to $E = 40\,\mathrm{kV/mm}$) such that the obtained shortening of the muscle of approximately 10 % of the original actuator length matches the maximum achievable contraction of commercially available stacked actuators[1].

[1] http://www.ct-systems.ch

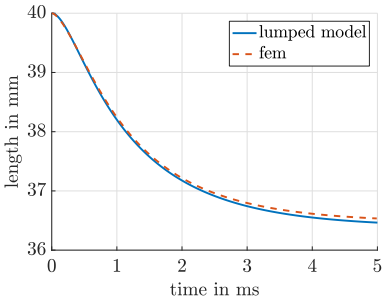

Figure 7.14: Error of the lumped parameter model due to clamped ends of the finite element muscle.

In Figure 7.13, the mesh deformation of the actuator in its fully contracted state is visualised. It can be observed that the end constraints that hinder expansion of the cross section area have only very local impact. Most of the actuator geometry deforms symmetrically and evenly as assumed in the lumped parameter model deformation gradient. Only in a region very close to the ends of the actuator, the deformation is different. In Figure 7.14, the lumped parameter model simulation results are compared to the results from the finite element model with constrained ends. The small deviation between the two models grows with increasing contraction, as expected. The contracted length of the lumped parameter model slightly overestimates the finite element model contraction, where the displacement is constrained and hence slightly smaller. It should be noted however, that the simulation of the finite element model with highly optimised and parallelised finite element C++ code running on a workstation with two Intel Xeon E5-2690 CPUs providing 24 cores took about ten minutes, whereas the simulation of the lumped parameter model running on a MacBook Pro in MATLAB finished after about 20 milliseconds. This corresponds to a remarkable speed-up factor of about 30 000 for the lumped parameter model compared to the finite element model.

Actuated multibody system

The lumped parameter model for the artificial muscle is implemented into MulDi as a two-point element via its energy contributions to the Lagrangian. The kinetic energy of the reduced dielectric elastomer model is extended to allow for rigid body motion (via translational velocity of its centre of mass) and the potential energy is extended to account for gravity.

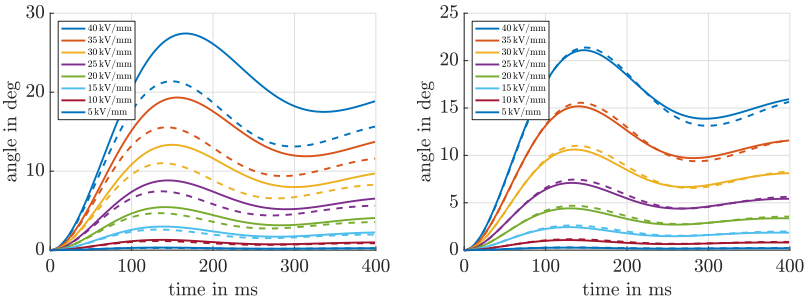

(a) Original parameters.

(b) Modified parameters.

Figure 7.15: Lumped parameter model results for the artificial muscle actuated revolute joint (MulDi: solid, FEM: dashed).

The actuated revolute joint in agonist-antagonist configuration from Section 5.4 is used to compare simulation results from the lumped parameter model to the finite element model. The actuated rigid body system including energy contributions and involved constraints is provided by MulDi for both systems, lumped parameter and finite element model, and hence identical. The finite element muscles are simulated using the fully incompressible material model (from Section 5.5.2), where the electromechanical coupling part is based on Equation (7.38) including the relative permittivity ε_r. In both models, the damping parameter is set to $\eta = 10\,{}^{\mathrm{g}}/_{\mathrm{ms\,mm}}$.

In Figure 7.15a, it can be observed that the lumped parameter model results (solid lines) exceed the joint deflections computed with the finite element model (dashed lines) for all applied constant voltages. In the finite element model, the muscles are constrained at both ends and bending occurs for larger joint angles (Figure 5.4). These effects are not covered by the lumped parameter model. For the simulation results shown in Figure 7.15b, the parameters of the lumped model are modified to achieve better matching. Decreasing the relative permittivity from $\varepsilon_r = 3.7$ to $\varepsilon_r = 3.1$ and increasing the muscle diameter from 10 mm to 11 mm for the lumped model, the error between the finite element model and the lumped model is clearly reduced, while the qualitative curve progression of the lumped model is preserved.

The modification of the lumped model parameters to increase accuracy while retaining the qualitative behaviour can be improved using curve fitting algorithms. Relevant parameters can be identified and modified such that the difference between lumped model simulation results and finite element simulation results (or measurement data) are minimised. This is of course only

possible if some (accurate) data set is available for comparison.

8 Optimal control of dielectric elastomer actuated systems

In the previous chapters, the voltages applied to the artificial muscles are prescribed in advance and the response of the actuated multibody system is computed via a forward dynamics simulation. In practical applications, where the actuated system should carry out a certain task involving a prescribed motion, information about the required control voltages is needed. Very often, a system must be transferred from a given initial state to a prescribed final state. Generally, there is an infinite number of control trajectories and resulting motion paths that fulfil this boundary value problem. To further constrain this variety of solutions, an objective function is defined that is to be minimised by the control trajectory and related motion of the system. To name a few examples, this objective function might affect the time, the control effort or the acceleration of the system required to reach the prescribed state.

The first difficulty however, is to find a feasible control sequence that yields the final state at all, which is not a trivial task for complex systems. This holds true especially for underactuated systems, where the system's state can not be exactly prescribed by control inputs but rather results from the system's dynamics as a response to the control input. Due to the elastic nature of dielectric elastomer actuated multibody systems, oscillations are inherently present and need to be avoided by appropriate control strategies.

The optimal control problem for dielectric elastomer actuated systems in this work is based on the direct transcription method DMOCC [Leye09]. This method allows to formulate the optimal control problem as a general nonlinear program (NLP) for which the Karush-Kuhn-Tucker conditions can be formulated and solved while at the same time all properties of the structure preserving integration scheme (Section 3) are adopted. The form and solution strategy of the NLP is presented in Section 8.1. In Section 8.2, the DMOCC method is applied to the electromechanically coupled problem of dielectric elastomer actuated multibody systems. Finally, in Section 8.3, numerical examples illustrate the application and capabilities of the electromechanically coupled optimal control framework.

8.1 General optimisation problem

The general form of a constrained non-linear optimisation problem that covers all needs of this work can be written as

$$\min_{\underline{x}} \quad \mathcal{J}(\underline{x}) \tag{8.1a}$$

$$\text{subject to} \quad \underline{c}(\underline{x}) = \underline{0} \tag{8.1b}$$

$$\underline{x}_l \leq \underline{x} \leq \underline{x}_u, \tag{8.1c}$$

where $\underline{x} \in \mathbb{R}^{n_{\text{opt}}}$ contains the n_{opt} optimisation variables, $\mathcal{J}(\underline{x})$ is the scalar objective function that is to be minimised, $\underline{c}(\underline{x}) \in \mathbb{R}^{n_{\text{constr}}}$ are n_{constr} equality constraints and $\underline{x}_l, \underline{x}_u \in \mathbb{R}^{n_{\text{opt}}}$ constrain the optimisation variables via lower and upper bounds, respectively [Geig02, Noce99]. A more general formulation might include non-linear inequality constraints as well. However, by introducing so called slack variables, inequality constraints can be transformed into equality constraints as shown in [Noce99]. Moreover, within this work inequality constraints appear solely as bound constraints on the optimisation variables, such that the formulation in Equations (8.1) is convenient.

8.1.1 Numerical solution methods

To solve the optimisation problem (8.1), stochastic and deterministic algorithms can be utilised. Stochastic methods like evolutionary algorithms or swarm algorithms are suited for systems with unknown quantities or unknown functional principles ("black box" system), discontinuities as well as uncertainty [Noce99]. By introducing randomness, these algorithms try and escape local optima and eventually yield global solutions of the optimisation problem. However, due to a lack of information about potential relationships in the system concerning the optimisation variables, stochastic algorithms are rather slow and computationally costly. Metaphorically speaking, they systematically poke around in the set of feasible solutions and pick the best hit.

On the other hand, deterministic algorithms exploit information about the inner relationships of the system. Gradient information is used to quickly minimise the optimisation function $\mathcal{J}$ and approach the nearest (local) minimum. This requires the underlying system equations to be sufficiently smooth. Moreover, an initial guess is required from where the algorithm iteratively converges to an optimal solution. This initial guess is of great importance as it strongly influences the local minimum to which the algorithm converges. It is important to note that many local optima may exist in the set of feasibly solutions and

there is no guarantee that a global optimum is found. In this work, only deterministic algorithms are used.

8.1.2 Gradient based methods

Many different algorithms for deterministic optimisation problems like line search methods, trust-region methods, interior point methods, sequential quadratic programming (SQP) or active set methods, to name just some of them, exist [Noce99]. Some of these algorithms solve non-linear problems directly and some other algorithms that were initially developed for linear optimisation problems are extended to solve non-linear problems as well. Within this work, existing optimisation algorithms are used as a tool to obtain optimal control trajectories rather than modifying the algorithm itself. Therefore, available software solutions are utilised.

Important and wide spread software packages that handle non-linear optimisation problems are the `fmincon` solver from MATLAB, SNOPT[1] and Ipopt[2]. Via `fmincon`, MATLAB provides a whole set of solution algorithms like interior point, SQP, active set and trust-region in a mature, well maintained and commercially distributed package. SNOPT, also commercially distributed and originally written in Fortran, provides wrappers for C and is based on a SQP algorithm. Ipopt is written in C++ and released as open source code. The interior point optimiser advertises with its ability to solve large-scale non-linear optimisation problems.

Because the models to be optimised within this work are implemented as C++ code and due to the free open source distribution, Ipopt is utilised for all optimisation tasks in this work. However, MulDi provides an intermediate interface where optimal control problems including constraints are defined. Ipopt is then just called as a solver for this problem and could easily be replaced by another algorithm. Historically, interior point methods can be seen as a derivative of the simplex method. Instead of having a large number of inexpensive iteration steps, each interior point iteration is rather computationally costly but can make significant progress towards the solution [Noce99]. Detailed information about the primal-dual interior point method that is implemented in Ipopt can be found in [Noce09, Wäch02, Wäch05a, Wäch05b, Wäch06].

[1] http://www.sbsi-sol-optimize.com
[2] http://projects.coin-or.org/Ipopt

8.2 Optimal control of dielectric elastomer actuated systems

To solve optimal control problems numerically, they need to be discretised. Depending on the level at which the discretisation is introduced, numerical solution methods can be classified, see [Bett98, vS92] for an overview. Indirect methods formulate the equations of motion as well as the objective functional in the continuous space and discretisation is introduced in the very last step, leading to discrete minimum/maximum principles [Leye11, OB08]. Direct methods first discretise the equations of motion and then solve the optimisation problem via discrete variation, leading to the Karush-Kuhn-Tucker equations. In this work, the direct transcription method DMOCC from [Leye09] is used. In consistency with the variational time integration scheme introduced in Chapter 3, in DMOCC, the discretisation is introduced as early as possible directly into the Lagrangian. The optimisation problem is then based on the discrete Euler-Lagrange-Equations, leading to Karush-Kuhn-Tucker equations that inherit the structure preserving characteristics of the variational time integration scheme. Hence, like in forward dynamics, also the solution obtained from the optimal control problem guarantees preservation of conjugate momenta.

8.2.1 Optimisation variables

For the optimal control problem, the optimisation variables $\underline{x}$ contain the discrete configurations $\underline{q}_n$ and control variables $\underline{u}_n$ for all time steps such that

$$\underline{x} = \begin{pmatrix} \underline{q}_0 \\ \underline{u}_0 \\ \underline{q}_1 \\ \underline{u}_1 \\ \vdots \\ \underline{q}_N \\ \underline{u}_N \end{pmatrix}. \tag{8.2}$$

During optimisation, not only the discrete control variables $\underline{u}_n$ are optimised such that the system approaches for example a desired final state, but also the configuration variables $\underline{q}_n$ are part of the optimisation problem. Optimisation constraints ensure that the configuration variables fulfil the discrete equations of motion, i.e. that the configuration trajectory that arises from the control trajectory is physically meaningful.

The number of optimisation variables is composed of the number of configuration and control variables of the model multiplied with the number of time steps that cover the time interval in which the optimisation takes place. Note that the number of time steps and hence the number of optimisation variables is constant during the optimisation and has to be chosen in advance. In order to optimise a system with respect to the time needed for a certain motion, additionally the time step size Δt can be introduced as an optimisation variable. The total number of optimisation variables dramatically affects the computational cost required to solve the optimal control problem. As a minimum amount of time is required to allow the system to transition into a new state, it is important to keep the number of configuration variables of the model that is to be optimised small.

8.2.2 Equations of motion constraints

Because the finite element method in three dimensional space introduces a huge number of degrees of freedom to the artificial muscle model, the reduced lumped parameter model from Chapter 7 is used instead to actuate the multibody system. The obtained optimal control trajectory is then applied to the full finite element model to explore the validity of the lumped parameter model optimisation.

The actuating artificial muscle is implemented into MulDi as a two-point element as described in Section 7.2. Therefore, no additional degrees of freedom are added on top of the multibody system configuration $\underline{s}$, but only a single control variable that corresponds to the applied voltage U from Equation (7.57) is introduced for each artificial muscle. Consequently, the control array $\underline{u}$ contains the voltages of all muscles. The optimisation variables therefore include

$$\underline{x} = \begin{pmatrix} \underline{s}_0 \\ \underline{u}_0 \\ \underline{s}_1 \\ \underline{u}_1 \\ \vdots \\ \underline{s}_N \\ \underline{u}_N \end{pmatrix}, \tag{8.3}$$

and the discrete Euler-Lagrange-Equations (5.18) for $n = 1, \ldots, N-1$ constitute the equality constraints $\underline{c}$ from the optimisation problem (8.1) to ensure physically meaningful and structure preserving motion. Note that the discrete equations of motion (5.18) here already include the null space projection

method such that Lagrange multipliers associated with internal and joint constraints are avoided and do not appear as additional optimisation variables. However, the constraints (5.11) itself must also be included for all time steps $n = 1, \dots, N-1$ in the equality constraints of the optimisation problem to ensure that all configurations are feasible.

8.2.3 Prescribing initial and final configurations

If initial or final configurations are fully prescribed and these configurations are feasible, i.e. they fulfil the constraints (5.11), then the constraints (5.11) for the first, respectively, last configuration do not have to be added as equality constraints to the optimisation problem. It is actually possible to remove also the corresponding configuration variables ($\underline{s}_0$, respectively, $\underline{s}_N$) from the optimisation variables. However, for writing modular code, it is generally easier to keep the initial and final configuration variables part of the optimisation problem and include additional equality constraints of the form

$$\underline{c} = \begin{pmatrix} \underline{s}_0 - \bar{\underline{s}}_0 \\ \underline{s}_N - \bar{\underline{s}}_N \end{pmatrix} = \underline{0}, \tag{8.4}$$

where $\bar{\underline{s}}_0$ and $\bar{\underline{s}}_N$ are the prescribed and constant initial and final configurations, respectively.

If the configuration of only some rigid bodies of the multibody system is prescribed, then only associated entries of the constraints (8.4) have to be included as equality constraints, where the configuration variables associated with other (free) rigid bodies still have to fulfil the constraints (5.11). To provide even more flexibility, MulDi allows to define independent orientation and connector constraints for single rigid bodies. Orientation constraints prescribe only the rotational orientation of a rigid body at the beginning or end of an optimal control problem, where the translation of the centre of gravity of the rigid body is still free. Connector constraints ensure that a certain point of the rigid body (specified via a connector as introduced in Section 6.1) is located at a prescribed position in space, without directly prescribing the orientation and translation of the concerned rigid body. Nevertheless, internal constraints that arise from the director formulation and possibly joint constraints have to be included to ensure feasibility. This is automatically covered by the MulDi optimisation framework when specifying appropriate constraints.

8.2.4 Prescribing initial and final momenta

Initial or final velocities of the system can indirectly be prescribed via additional constraints based on the discrete Legendre transform evaluated at t_0 or t_N as in Equations (3.34a) and (3.35) in Section 3.6.1. For rest-to-rest manoeuvres, the prescribed conjugate momenta $\bar{\underline{p}}_0$ and $\bar{\underline{p}}_N$ equal zero. This also holds true for the null space projected conjugate momenta, i.e. $\underline{\underline{T}}(\underline{s}_0) \cdot \bar{\underline{p}}_0 = \underline{0}$ and $\underline{\underline{T}}(\underline{s}_N) \cdot \bar{\underline{p}}_N = \underline{0}$, respectively.

A convenient way to prescribe the system's initial or final state regarding kinetic terms is to specify the joint velocities. The joint velocities $\dot{\underline{s}}^{\min}$ are connected to the director configuration velocity $\dot{\underline{s}}$ via the null space matrix $\underline{\underline{T}}(\underline{s})$ such that

$$\dot{\underline{s}} = \underline{\underline{T}}(\underline{s}) \cdot \dot{\underline{s}}^{\min}, \tag{8.5}$$

as introduced generally in Equation (3.18). The conjugate momentum in the tangential space is abbreviated by

$$\tilde{\underline{p}} = \underline{\underline{T}}^T(\underline{s}) \cdot \underline{p} \tag{8.6}$$

and the momentum $\underline{p}$ is connected to the director configuration velocity $\dot{\underline{s}}$ via the mass matrix $\underline{\underline{M}}$ such that

$$\underline{p} = \underline{\underline{M}} \cdot \dot{\underline{s}}. \tag{8.7}$$

For the null space projected momentum $\tilde{\underline{p}}$ it follows that

$$\tilde{\underline{p}} = \underline{\underline{T}}^T(\underline{s}) \cdot \underline{\underline{M}} \cdot \underline{\underline{T}}(\underline{s}) \cdot \dot{\underline{s}}^{\min}, \tag{8.8}$$

giving rise to introduce the reduced mass matrix

$$\tilde{\underline{\underline{M}}}(\underline{s}) = \underline{\underline{T}}^T(\underline{s}) \cdot \underline{\underline{M}} \cdot \underline{\underline{T}}(\underline{s}). \tag{8.9}$$

Finally, the null space projected initial or final momentum can be derived from (minimal) joint velocities by

$$\tilde{\underline{p}} = \tilde{\underline{\underline{M}}}(\underline{s}) \cdot \dot{\underline{s}}^{\min}. \tag{8.10}$$

Note that after introducing the artificial muscle lumped parameter model to the multibody system, the total mass matrix can not be derived from single rigid body mass matrices as shown in Equation (5.4) any more. Because the artificial muscle model adds kinetic energy contributions to the Lagrangian, the total mass matrix has to be derived from the Lagrangian as shown in Equation (3.38).

MulDi allows to specify whether no constraints apply for the momentum, the system should be at rest, or minimal joint velocities are prescribed for the initial and final states individually. Relevant equations are then automatically derived and included as equality constraints to the optimisation problem. Note that because the reduced mass matrix $\underline{\underline{\tilde{M}}}$ is generally dense, the individual entries in $\underline{\dot{s}}^{\min}$ are not decoupled from each other in the discrete equations of motion. Therefore constraining the velocity of just some joints, whereas other joint velocities are free, can not be achieved by just including some entries of Equations (3.34a) or (3.35) as equality constraints to the optimisation problem.

8.2.5 Control variables

Control variables have to be bounded in order to avoid physically impossible or destructive values that would harm the real system. MulDi allows to set bounds for all control variables individually, which are then included in the optimisation problem via bound constraints in Equation (8.1c). In this work, bound constraints only affect control variables, whereas configuration variables are indirectly constrained via the discrete Euler-Lagrange-Equations.

For a typical rest-to-rest optimal control problem, the optimisation problem takes the form

$$\min_{\underline{x}} \quad \mathcal{J}(\underline{x}) \tag{8.11a}$$

$$\text{subject to} \quad \underline{c}(\underline{x}) = \begin{pmatrix} \underline{s}_0 - \bar{\underline{s}}_0 \\ \tilde{\underline{p}}_0^-(\underline{s}_0, \underline{u}_0, \underline{s}_1) \\ \begin{Bmatrix} \underline{F}_s(\underline{s}_0, \underline{u}_0, \underline{s}_1, \underline{u}_1, \underline{s}_2) \\ \underline{h}(\underline{s}_1) \end{Bmatrix} \\ \begin{Bmatrix} \underline{F}_s(\underline{s}_1, \underline{u}_1, \underline{s}_2, \underline{u}_2, \underline{s}_3) \\ \underline{h}(\underline{s}_2) \end{Bmatrix} \\ \vdots \\ \begin{Bmatrix} \underline{F}_s(\underline{s}_{N-2}, \underline{u}_{N-2}, \underline{s}_{N-1}, \underline{u}_{N-1}, \underline{s}_N) \\ \underline{h}(\underline{s}_{N-1}) \end{Bmatrix} \\ \tilde{\underline{p}}_N^+(\underline{s}_{N-1}, \underline{u}_{N-1}, \underline{s}_N) \\ \underline{s}_N - \bar{\underline{s}}_N \end{pmatrix} = \underline{0} \tag{8.11b}$$

$$\underline{u}_l \leq \underline{u} \leq \underline{u}_u, \tag{8.11c}$$

where $\underline{F}_s$ is taken from Equation (5.18) (extended by control variables as described in Section 3.5) and $\underline{h}$ is taken from Equation (5.11) such that just the objective function $\mathcal{J}(\underline{x})$ is left to be further specified.

Note that even though the array of optimisation variables $\underline{x}$ might contain a large number n_{opt} of entries, usually there is also a large number n_{constr} of equality constraints. Only the difference $n_{\mathrm{dof}} = n_{\mathrm{opt}} - n_{\mathrm{constr}}$ specifies the number of degrees of freedom of the optimisation problem. Therefore, the number of time steps has to be large enough providing sufficient control variables in order to satisfy all constraints and minimise the objective.

8.2.6 Objective functions

In many real applications, especially for underactuated systems, the most difficult part in solving an optimal control problem is to find a feasible solution at all, i.e. a sequence of configuration and control variables that satisfy the Euler-Lagrange-Equations and additionally fulfil imposed initial and final conditions. Therefore mainly two different objective functions are applied within this work.

The first objective function

$$\mathcal{J}_{\mathrm{const}} = 0 \tag{8.12}$$

represents a constant value. As this function is constant and not depending on any optimisation variable, it does not impose any further restriction on the optimisation process apart from the equality and bound constraints. This objective function is therefore helpful in finding a feasible solution for the optimisation problem, especially if no valuable initial guess is available. The feasible solution obtained with the constant objective can then be used as an initial guess for further optimisations including more restrictive constraints or a non-constant objective.

Moreover, the constant objective is helpful in solving so called square optimisation problems that have no degrees of freedom left, because the number of constraints equals the number of optimisation variables. These problems arise if an actual forward dynamics problem is solved as one big system of equations monolithically, instead of being solved iteratively in time. The square problem can be obtained by prescribing initial configuration and momentum, not specifying any final conditions and bounding the control variables such that they are fixed. The solution of this problem is unique and equal to the solution of the corresponding forward dynamics simulation. This procedure is used to verify the implementation of the optimal control problem.

The second objective function is the so-called control effort. The control effort

is defined as

$$\mathcal{J}_{\text{effort}}(\underline{x}) = \sum_{n=0}^{N} ||\underline{u}_n||^2 \tag{8.13}$$

and represents the sum of the squared norms of all control arrays. By minimising the control effort, in this work, the squared sum of the applied voltages over all time steps is minimised. This avoids single voltage peaks and prefers smooth voltage trajectories. Moreover, when starting the optimisation in a steady state where all control voltages equal zero, the physical time needed for approaching the prescribed final state can be minimised indirectly. To illustrate that point, the system might be kept at rest for some time in the beginning and a voltage is first applied only at a later time point such that motion happens only in the last part of the optimisation time interval.

Because the voltages applied to the artificial muscles are rather large, the control effort objective $\mathcal{J}_{\text{effort}}$ might be several magnitudes greater than the integrator constraints, leading to an ill conditioned system. This can be avoided by scaling the objective such that

$$\tilde{\mathcal{J}}_{\text{effort}}(\underline{x}) = \gamma\, \mathcal{J}_{\text{effort}}(\underline{x}), \tag{8.14}$$

where γ is the scaling factor.

8.2.7 Initial guess

An initial guess for the optimal control solution has to be provided to the interior point algorithm. This initial guess is of great importance as it affects whether or not an optimal solution for the problem is found at all and if so, which local optimum is found. MulDi allows to specify three different types of initial guesses.

The first and most simple approach is to use a zero vector as initial guess. This approach is free of any presumptions and hence very neutral. However, due to the director parametrisation of the multibody system, the zero vector initial guess is infeasible regarding all of the internal director constraints and hence might not lead to a feasible solution. The second approach is to use the initial configuration of the multibody system and zero controls for all time steps as initial guess. This guess has the advantage that all constraints except the final conditions are already fulfilled including the Euler-Lagrange-Equations and initial conditions. However, in order to also fulfil the final conditions in the optimal control problem solution, it is very likely that the initial guess changes drastically. The third approach is to use the result of a previous optimal

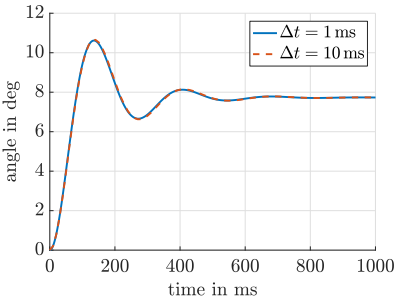

Figure 8.1: Oscillations of the revolute joints with a constant applied voltage simulated for different time step sizes.

control solution or the result of a forward dynamics simulation as initial guess. This is also possible if the previous optimisation did not finish successfully and did not find a sufficiently feasible solution.

8.3 Numerical examples

In this section, numerical examples illustrate the solution of optimal control problems in electromechanically coupled systems. To reduce the computational cost, the lumped parameter model from Chapter 7 is used for the artificial muscle actuation of the multibody systems. Because the reduced actuator model inevitably introduces some error to the simulations results, for validation reasons the obtained optimal control trajectory is applied to the finite element model in a forward dynamics simulation for each example.

8.3.1 Revolute joint oscillations

The first example is the revolute joint from Section 5.4 with the lumped parameter approach from Section 7.2.5. When a constant voltage s applied to one of the muscles such that the initial electric field magnitude is $E = 30\,\mathrm{kV/mm}$, the revolute joint oscillates for about 1 s before it approaches its steady state angle of $\alpha = 7.73\,\mathrm{deg}$, as illustrated in Figure 8.1. It is also shown that if the time step size of the simulation is increased from 1 ms to 10 ms, the simulation results hardly differ and hence it can be concluded that the large time step size

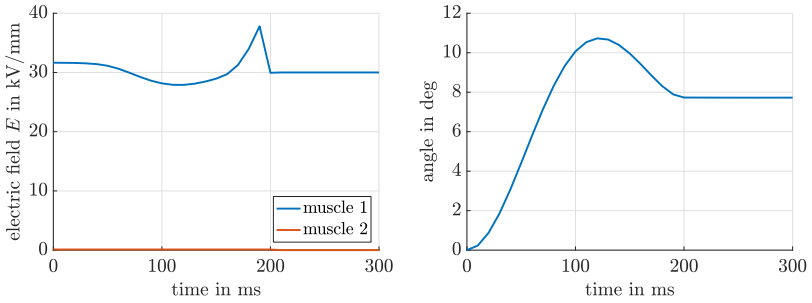

(a) Optimised voltage trajectories. (b) Optimised joint angle over time.

Figure 8.2: First optimisation result of the revolute joint.

is still accurate enough. The larger time step size reduces the computational cost of the optimal control problem significantly.

To make the artificial muscle actuated revolute joint more suitable for e.g. positioning tasks, the oscillations as well as the time needed to reach the steady state is reduced by using optimal control theory. The problem is set-up with rest-to-rest constraints, where the initial configuration corresponds to zero joint deflection and the final configuration is prescribed by a joint deflection of $\alpha = 7.73\,\text{deg}$ at $t = 200\,\text{ms}$. The control voltages for the muscles are both bounded such that negative values do not occur and the electric field strength in the material configuration does not exceed $E = 50\,\text{kV/mm}$.

Whereas Ipopt does not converge to any feasible optimal solution when minimising the control effort, for a constant objective the result presented in Figure 8.2 is obtained. The plots are created by evaluating a forward dynamics simulation with the control input taken from the optimisation result. As the optimisation does only cover the first 200 ms, after that time the voltage of the first muscle is set to its default value such that $E = 30\,\text{kV/mm}$ and the voltage of the second muscle is set to zero. With these values, the steady state angle is retained. In Figure 8.2b, it can be observed that the joint angle first overshoots its target but when swinging back it quickly decelerates and after exactly 200 ms it reaches its steady state. Figure 8.2a reveals how this behaviour is obtained. When swinging back, just before $t = 200\,\text{ms}$ a voltage peak creates the decelerating force.

Since in this example the system has enough time to overshoot its target angle and swing back, the obvious question is whether the optimisation time interval can be further decreased. If the final condition is prescribed at $t = 70\,\text{ms}$ while

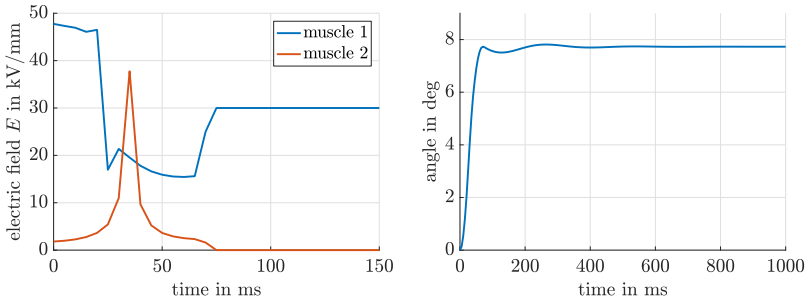

(a) Optimised voltage trajectories.

(b) Optimised joint angle over time.

Figure 8.3: Second optimisation result of the revolute joint.

the time step size is decreased to $\Delta t = 5\,\text{ms}$ and a constant objective is set, Ipopt converges to the feasible solution presented in Figure 8.3. From the voltage trajectories for the two muscles in Figure 8.3a, it can be concluded that the two muscles take on the roles of agonist and antagonist of the revolute joint. To start the deflection, the agonist (muscle 1) is stimulated with a high voltage. Moments later the voltage of the first muscle is reduced and the antagonist (muscle 2) is activated to decelerate the joint motion. Then the system is kept in its steady state via the default voltages. In Figure 8.3b however, it can be observed that there are still some minor oscillations in the joint deflection angle after $t = 70\,\text{ms}$. Very likely, the sudden change in the control voltages of the two muscles at the end of the optimisation interval and the associated change in the potential energy from electric field terms causes this oscillation. Remember that the muscle model is based on electrostatics and there are no dynamic interactions concerning electrical quantities in contrast to mechanical values that are affected by inertia terms.

Verification with finite element model

In order to validate the optimal control solution from the lumped parameter model, the obtained voltage trajectory is applied to the corresponding finite element model that is illustrated in Figure 5.16. Due to the finer spatial resolution, the finite element model requires a smaller time step size ($\Delta t = 1\,\text{ms}$) than the lumped parameter model ($\Delta t = 10\,\text{ms}$ and $\Delta t = 5\,\text{ms}$). Therefore some interpolation is necessary to apply the optimised control trajectory to the finite element model. In Figure 8.4, two different interpolation methods are compared for fictional control values. The linear interpolation connects

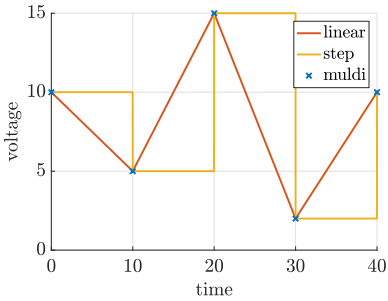

Figure 8.4: Different interpolation methods for the control trajectory.

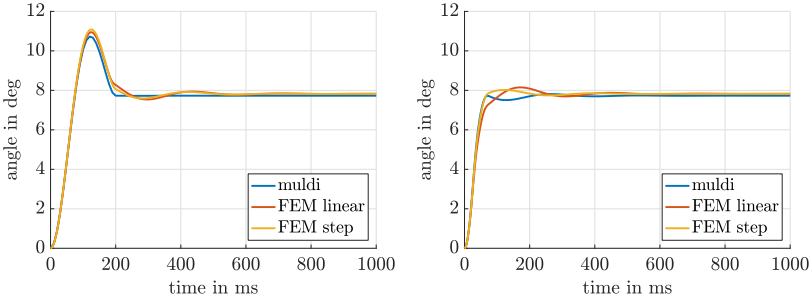

(a) First optimisation result.

(b) Second optimisation result.

Figure 8.5: Validation of the revolute joint optimisation with the finite element model.

two discrete neighbouring voltage values from the optimisation with a straight line. The step interpolation keeps the voltage constant for each time interval of 10 ms. As the approximation of the control variables in the Lagrangian (see Section 3.5) that is used by MulDi assumes constant values over the interval of one time step, the step interpolation based finite element simulation is presumed to be closer to the MulDi results. However, the linear interpolation is “smoother” and might be less disruptive in contrast to the sudden changes in the step interpolation. Therefore the two interpolation methods are both used and compared to each other.

In Figure 8.5a, the finite element simulation results for both interpolation methods are compared. It can be observed that the finite element model shows more oscillations than the lumped parameter model, however the joint

still reaches its steady state angle much quicker compared to the case where a constant voltage is applied (compare to Figure 7.15). The influence of the interpolation method is not that strong. The maximum angle difference between the two models for the linear interpolation is 0.54 deg, whereas the maximum difference for the step interpolation is 0.50 deg. In Figure 8.5b, the finite element simulation results for the second optimal control trajectory are shown. The maximum angle error for the linear interpolation is 0.62 deg and the maximum error for the step interpolation is 0.51 deg. This confirms the assumption that the step interpolation for the finite element model is more consistent to the optimisation results of lumped parameter model.

The overall difference between simulations of the finite element model and the lumped parameter model for the optimised voltage trajectories is quite small. Given the fact that even the finite element model will not match real measurements perfectly, in real applications of artificial muscle actuated systems a real-time closed loop control is necessary. The error between the real system and the model is presumed to be small enough to be handled by a closed loop control algorithm.

8.3.2 Elephant trunk

The second model is a kinematic chain that consists of series-connected revolute joints. Each joint is rotated relative to its predecessor by 90 degrees and actuated via two artificial muscles in agonist-antagonist configuration. This setting allows for motion in all space dimensions and is further referred to as elephant trunk.

Figure 8.6 shows the base element from which the elephant trunk is assembled. Several of these elements can be put together if rotated 90 degrees around the y-axis. The interface then acts as a revolute joint with the rotation axis alternating between the x-axis and z-axis. In Table 8.1, the mass properties and connector positions are given. The mass m is obtained by assuming the density of plastic and integrating over the geometry. The moments of inertia in principal axis J_{xx}, J_{yy}, J_{zz} are given with respect to the centre of gravity of the body. From this centre of gravity, the connectors $\boldsymbol{\varrho_1}, \ldots, \boldsymbol{\varrho_6}$ describe interaction points of the rigid body. The points $\boldsymbol{\varrho_1}$ and $\boldsymbol{\varrho_6}$ are used to connect the rigid bodies with each other while the points $\boldsymbol{\varrho_2}, \ldots, \boldsymbol{\varrho_5}$ describe insertion points for the artificial muscles. The muscles are 50 mm long and have a diameter of 8 mm. Material properties of the muscles are $\rho_0 = 1 \cdot 10^{-3}\,{}^{\mathrm{g}}/_{\mathrm{mm}^3}, \varepsilon_r = 3.7, Y = 0.7\,\mathrm{MPa}$ and $\eta = 100\,{}^{\mathrm{g}}/_{\mathrm{ms\,mm}}$.

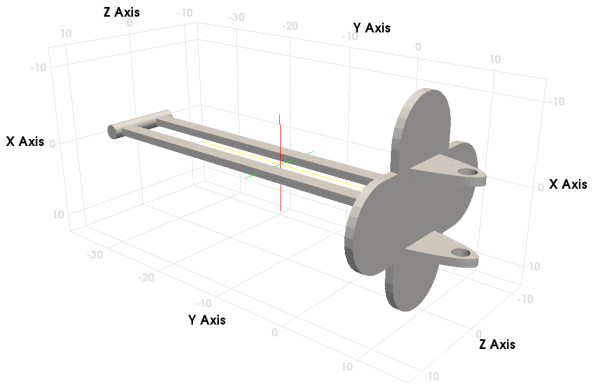

Figure 8.6: Single element of the elephant trunk with orientation and dimensions in mm.

Table 8.1: Properties of a single element of the elephant trunk.

parameter	value	unit
m	61	g
J_{xx}	15036	$\mathrm{g\,mm^2}$
J_{yy}	2524	$\mathrm{g\,mm^2}$
J_{zz}	14940	$\mathrm{g\,mm^2}$
$\boldsymbol{\varrho_1}$	$\begin{pmatrix}0 & -36.958872 & 0\end{pmatrix}^T$	mm
$\boldsymbol{\varrho_2}$	$\begin{pmatrix}-7.5 & 8.041128 & 0\end{pmatrix}^T$	mm
$\boldsymbol{\varrho_3}$	$\begin{pmatrix}7.5 & 8.041128 & 0\end{pmatrix}^T$	mm
$\boldsymbol{\varrho_4}$	$\begin{pmatrix}0 & 9.041128 & 7.5\end{pmatrix}^T$	mm
$\boldsymbol{\varrho_5}$	$\begin{pmatrix}0 & 9.041128 & -7.5\end{pmatrix}^T$	mm
$\boldsymbol{\varrho_6}$	$\begin{pmatrix}0 & 14.041128 & 0\end{pmatrix}^T$	mm

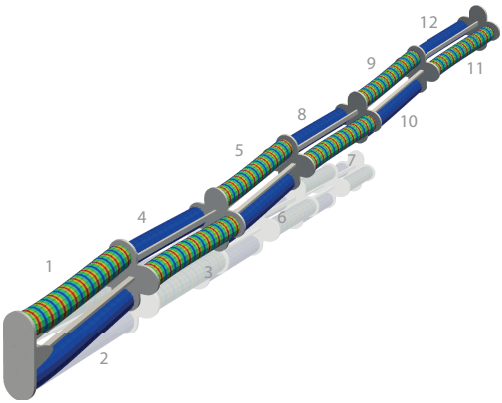

Figure 8.7: Assembled elephant trunk with six rigid bodies and twelve artificial muscles in its initial configuration (light grey) and deflected state (coloured). The colouring refers to the applied electric potential.

The assembled elephant trunk is illustrated in Figure 8.7. It consists of six rigid bodies that are connected via revolute joints, where the first revolute joint is spatially fixed. In total, the multibody system has six degrees of freedom. These degrees of freedom are each actuated by two opponent artificial muscles. The resulting twelve muscles are numbered as denoted in Figure 8.7. Gravity is neglected as otherwise the muscles are not powerful enough to withstand their own weight. The actuated model is implemented via finite elements for the muscles as well as via the lumped parameter model, where both implementations share exactly the same parameters.

When a constant voltage is applied to only odd muscles such that $E = 30\,\mathrm{kV/mm}$, then the elephant trunk bends diagonally as illustrated in Figure 8.7. In its steady state, the tip of the last body (director $\boldsymbol{\varrho_6}$) is located at $x = -95.8341\,\mathrm{mm}$, $y = 274.054\,\mathrm{mm}$ and $z = 73.0747\,\mathrm{mm}$. For the rest-to-rest optimal control problem, this location is prescribed as an end position via a director constraint as introduced in Section 8.2.3. The prescribed initial configuration corresponds to the initial (straight) state. The control voltages are bound to be positive and limiting the material electric field strength strength to $E = 40\,\mathrm{kV/mm}$. The optimal control problem covers a period of 1 s with a time step size of $\Delta t = 25\,\mathrm{ms}$.

First, by using the constant objective function, a feasible solution for the optimal control problem is obtained. Then, using the previous optimisation

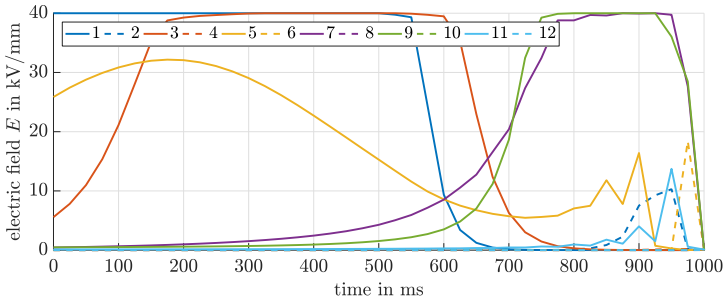

Figure 8.8: Optimised elephant trunk voltage trajectories for agonists (solid line) and antagonists (dashed line).

result as an initial guess, the control effort is successfully minimised using a scaling factor of $\gamma = 1 \cdot 10^{-14}$ (see Equation (8.14)). In Figure 8.8, the optimised voltage trajectories are illustrated. It can be observed that the maximum allowed voltages are fully exploited and that there is a complex interaction between agonists (odd muscles, solid) and some antagonists (even muscles, dashed).

In Figure 8.9, the forward dynamics simulation results for the constant voltage and the optimised voltage trajectories are compared to each other. Figure 8.9a shows the x, y and z coordinates of the tip of the elephant trunk. It is clearly seen that the optimised voltages lead to less oscillations and the steady state is approached very quickly. In Figure 8.9b, the motion of the elephant trunk tip in the (x-z)-plane can be observed. While the constant voltages lead to overshooting and oscillations around the steady state, the optimised trajectories actuate the system directly towards its final configuration.

Verification with finite element model

The finite element mesh containing all twelve muscles consists of 3 456 finite elements and 33 168 degrees of freedom, where 1 650 degrees of freedom are eliminated by multibody system coupling constraints. With a time step size of $\Delta t = 1\,\text{ms}$, a forward dynamics simulation period of 10 s takes about 35 h computing time on a high performance 24-core computer. The corresponding lumped parameter model simulation finished after about 10 s.

The simulation results for the finite element model are illustrated in Figure 8.10.

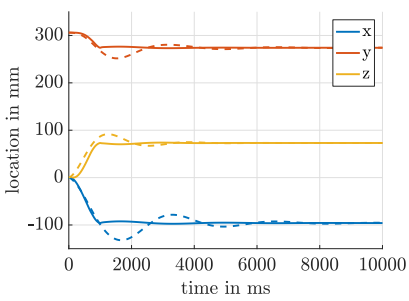

(a) Spatial connector position. Constant voltage (dashed) and optimised voltage (solid).

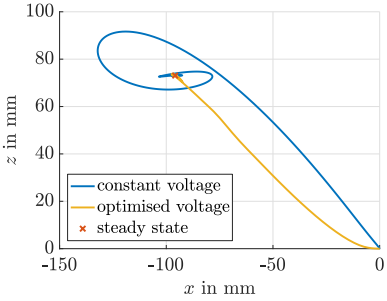

(b) Position in (x-z)-plane.

Figure 8.9: Comparison between constant and optimised voltage of the lumped parameter model.

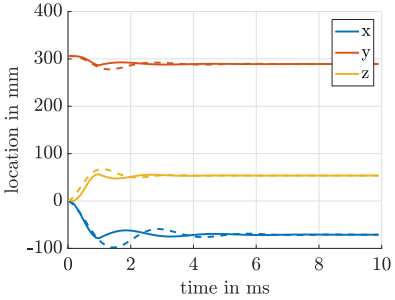

(a) Spatial connector position. Constant voltage (dashed) and optimised voltage (solid).

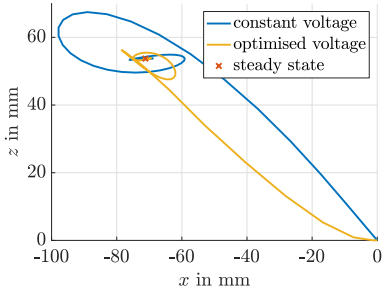

(b) Position in (x-z)-plane.

Figure 8.10: Comparison between constant and optimised voltage of the finite element model.

Note that in contrast to the revolute joint optimisation example, the parameters of the lumped parameter model are here not adjusted to match the finite element simulation results (compare to the "Actuated multibody system" example in Section 7.2.5). Instead, exactly the same parameters are used for both models. As a consequence, the finite element model converges to a different steady state compared to the lumped parameter model. However, the optimised control trajectory still slightly reduces emerging oscillations, as shown in Figure 8.10a. A look at the (x-z)-plane motion in Figure 8.10b also reveals that overshooting slightly decreased.

This example illustrates that optimal control trajectories obtained from the lumped parameter model have to be handled with care when being applied to the real system. The lumped parameter model should match the real behaviour of the system as closely as possible in order to obtain reliable control trajectories. Furthermore, robust optimisation criteria might be considered in the optimal control problem to decrease the effect of model variations on the optimised motion.

9 Conclusions

Summary In this work, a simulation framework is presented that allows to predict and control the behaviour of multibody systems that are actuated via dielectric elastomers. A complex finite element model for dielectric elastomers provides a flexible, versatile and accurate forward dynamics simulation of actuated structures. An energy consistent lumped parameter model for the artificial muscles reduces the computational cost required for the simulation and allows to solve optimal control problems. Using optimal control, oscillations that are inherent with the elastic structure of the artificial muscles can be avoided. The multibody simulation library MulDi that emerged from this work simplifies the set-up, analysis, simulation and optimal control of dielectric elastomer actuated multibody systems. All dynamic simulation in this work is based on variational integration schemes that provide structure preservation and a very good energy behaviour.

Relevance The finite element model for dielectric elastomers presented in this work is, to the best of my knowledge, the first monolithic formulation that provides structure preservation for electromechanically coupled three-dimensional continua. Besides the good energy conversation properties, the variational time integration scheme allows to fulfil algebraic constraints exactly (with numerical accuracy) at the discrete time nodes, avoiding the so-called drift of configuration variables. This feature is exploited two times in this work. First, the constraints in the partial differential algebraic system of equations (PDAE) resulting from the coupling between the finite element actuator model and the multibody system can be formulated at configuration level and fulfilled exactly, avoiding index reduction techniques. Second, the incompressibility constraint of the dielectric elastomer material in the finite element formulation is fulfilled exactly, allowing for not only nearly incompressibility (as in many common formulations) but also for true incompressibility. This might also be of interest in other fields of application where incompressibility plays a role, like human tissue modelling.

Another important aspect of this work is that it combines the use of complex and accurate finite element models and cost saving lumped parameter models for dielectric actuators. This allows to identify the relation between the two

approaches and reveal and assess limitations of reduced models. The energy consistent lumped parameter model for dielectric elastomers that is derived in this work complements the finite element model in terms of computational cost flexibility. The parallel use of consistent simulation models from both worlds allows for solving complex problems like obtaining optimal control solutions.

Findings The experience in simulating artificial muscle actuated multibody systems has shown that the application of dielectric elastomers as actuators in humanoid systems is quite limited. Due to electrical instabilities and a limited breakdown strength, the maximum achievable contraction of stacked actuators in real applications is approximately 10 %. If a revolute joint is equipped with two artificial muscles in agonist-antagonist configuration, large deflections can only be obtained via a short lever arm. However, the short lever arm increases the force required to actuate the joint. The maximum achievable blocked force of stacked actuators with a diameter of 1 cm lies in the range of only 1 N. If artificial muscles actuate a whole kinematic chain, they can hardly withstand their own weight. Promising applications of stacked dielectric elastomers include settings were only small displacements and small forces are required like in valves, linear drives, pumps, dosing systems, locks or relays.

Other promising applications utilise the large surface area (and hence increased electrostatic pressure) of dielectric elastomer membranes and the associated in-plane expansion instead of utilising the out-of-plane contraction of stacked actuators. Membrane actuators are also easier to produce because the stacking process of pile-up configurations is quite challenging. All applications share however, that sophisticated control strategies are required to operate the underactuated systems that result from the elastic nature of the actuators and inherent oscillations. The gradient based optimal control theory used in this work is shown to efficiently avoid oscillations by providing optimised voltage trajectories to actuate the artificial muscles. Moreover, optimal control allows to temporally exceed maximum static specifications of the actuators like the maximum allowed voltage without causing any failure like electrical breakdown.

Outlook The lumped parameter model for dielectric actuators presented in this work turned out to be a suitable representation of the dynamic behaviour of artificial muscles in simple settings. However, effects that arise from bending of the muscles are not covered by the reduced model. To further increase the simulation accuracy, beam models might be a useful approach. An artificial

muscle beam model might be able to cover bending effects without overly increasing the computational cost. A suitable balance between accuracy and complexity has to be further investigated. Independent of the simulation model accuracy, a closed loop real-time control algorithm will be required for practical applications of dielectric elastomer actuated systems. Even the most complex simulation tool will deviate from the real behaviour and external disturbances need to be handled in real-time in order to provide a reliable behaviour. Note that the application of optimal control theory happens "off-line" and does only cover predefined situations. Due to the electromechanical coupling and associated non-linearities as well as the underactuated control nature, a sophisticated and non-linear real-time control is necessary in practice.

This work covers only settings in which no dynamic contact between different muscles or between a muscle and a rigid body happens, apart from the fixed muscle ends. In more sophisticated applications, the muscle deformation might be hindered by contact with the system's structure or external objects. Such contact problems also play a major role in dielectric elastomer membrane applications, where a surrounding membrane actuator exerts a pressure on the wrapped body, like a compression bandage.

References

[Ali10] A. Ali, M. Hosseini, and B. B. Sahari. A review of constitutive models for rubber-like materials. *American Journal of Engineering and Applied Sciences*, 3(1):232–239, 2010.

[Ask10] A. Ask, A. Menzel, and M. Ristinmaa. On the modelling of electro-viscoelastic response of electrostrictive polyurethane elastomers. *IOP Conference Series: Materials Science and Engineering*, 10(1), 2010.

[Ask12a] A. Ask, A. Menzel, and M. Ristinmaa. Electrostriction in electro-viscoelastic polymers. *Mechanics of Materials*, 50:9–21, 2012.

[Ask12b] A. Ask, A. Menzel, and M. Ristinmaa. Phenomenological modeling of viscous electrostrictive polymers. *International Journal of Non-Linear Mechanics*, 47(2):156–165, 2012.

[Ask13] A. Ask, R. Denzer, A. Menzel, et al. Inverse-motion-based form finding for quasi-incompressible finite electroelasticity. *Numerical Methods in Engineering*, 94(6):554–572, 2013.

[Ask15] A. Ask, A. Menzel, and M. Ristinmaa. Modelling of viscoelastic dielectric elastomers with deformation dependent electric properties. In *Proceedings of the IUTAM Symposium on Mechanics of Soft Active Materials*, vol. 12, pp. 134–144, 2015.

[Bang07] W. Bangerth, R. Hartmann, and G. Kanschat. deal.II – a general purpose object oriented finite element library. *ACM Transactions on Mathematical Software*, 33(4):24/1–24/27, 2007.

[BC00] Y. Bar-Cohen. Electroactive polymers as artificial muscles: Capabilities, potentials and challenges. *Robotics 2000*, pp. 188–196, 2000.

[Bell17] B. Bell. CppAD: a package for C++ algorithmic differentiation. COIN-OR: http://www.coin-or.org/CppAD, 2017.

[Bers13] G. Berselli, R. Vertechy, M. Babič, et al. Dynamic modeling and experimental evaluation of a constant-force dielectric elastomer actuator. *Journal of Intelligent Material Systems and Structures*, 24(6):779–791, 2013.

[Bets00] P. Betsch and P. Steinmann. Inherently energy conserving time finite elements for classical mechanics. *Journal of Computational Physics*, 160(1):88–116, 2000.

[Bets06] P. Betsch and S. Leyendecker. The discrete null space method for the energy consistent integration of constrained mechanical systems. Part II: Multibody dynamics. *International Journal for Numerical Methods in Engineering*, 67:499–552, 2006.

[Bett98] J. T. Betts. Survey of numerical methods for trajectory optimization. *Journal of Guidance, Control, and Dynamics*, 21(2):193–207, 1998.

[Bone08] J. Bonet and R. D. Wood. *Nonlinear Continuum Mechanics for Finite Element Analysis*. Cambridge University Press, 2008.

[Brin96] U. Brink and E. Stein. On some mixed finite element methods for incompressible and nearly incompressible finite elasticity. *Computational Mechanics*, 19(1):105–119, 1996.

[Carp15] F. Carpi, I. Anderson, S. Bauer, et al. Standards for dielectric elastomer transducers. *Smart Materials and Structures*, 24(10), 2015.

[Chee16] P. S. Chee, C. K. Mah, and M. S. M. Ali. Soft dielectric elastomer actuator for micropump application. In *2016 IEEE 29th International Conference on Micro Electro Mechanical Systems (MEMS)*, pp. 561–564, 2016.

[Dorf03] A. Dorfmann and R. W. Ogden. Magnetoelastic modelling of elastomers. *European Journal of Mechanics - A/Solids*, 22(4):497–507, 2003.

[Dorf05] A. Dorfmann and R. W. Ogden. Nonlinear electroelasticity. *Acta Mechanica*, 174:167–183, 2005.

[Dorf06] A. Dorfmann and R. W. Ogden. Nonlinear electroelastic deformations. *Journal of Elasticity*, 82(2):99–127, 2006.

[Dorf10] A. Dorfmann and R. W. Ogden. Nonlinear electroelastostatics: Incremental equations and stability. *International Journal of Engineering Science*, 48(1):1–14, 2010.

[Erin63] A. C. Eringen. On the foundations of electroelastostatics. *International Journal of Engineering Science*, 1(1):127–153, 1963.

[Erin89] A. C. Eringen and G. A. Maugin. *Electrodynamics of Continua I: Foundations and Solid Media*. Springer, 1989.

[Fish07] J. Fish and T. Belytschko. *A First Course in Finite Elements*. Wiley, 2007.

[Fox09] J. Fox and N. Goulbourne. Electric field-induced surface transformations and experimental dynamic characteristics of dielectric elastomer membranes. *Journal of the Mechanics and Physics of Solids*, 57(8):1417–1435, 2009.

[Gei14] M. Gei, S. Colonnelli, and R. Springhetti. The role of electrostriction on the stability of dielectric elastomer actuators. *International Journal of Solids and Structures*, 51(3-4):848–860, 2014.

[Geig02] C. Geiger and C. Kanzow. *Theorie und Numerik restringierter Optimierungsaufgaben*. Springer, 2002.

[Ghaz17] F. A. M. Ghazali, C. K. Mah, A. AbuZaiter, et al. Soft dielectric elastomer actuator micropump. *Sensors and Actuators A: Physical*, 263:276–284, 2017.

[Goul05] N. Goulbourne. *Electroelastic Modeling of Dielectric Elastomer Membrane Actuators*. Ph.D. thesis, Pennsylvania State University, Department of Mechanical Engineering, 2005.

[Grif12] D. J. Griffiths. *Introduction to electrodynamics*. Addison-Wesley, 2012.

[Guen17] G. Guennebaud, B. Jacob, et al. Eigen. http://eigen.tuxfamily.org, 2017.

[Hair00] E. Hairer and C. Lubich. Long-time energy conservation of numerical methods for oscillatory differential equations. *SIAM Journal on Numerical Analysis*, 39(2):414–441, 2000.

[Hair06] E. Hairer, C. Lubich, and G. Wanner. *Geometric Numerical Integration*. Springer, 2006.

[Hero05] M. A. Heroux, R. A. Bartlett, V. E. Howle, et al. An overview of the trilinos project. *ACM Transactions on Mathematical Software*, 31(3):397–423, 2005.

[Holz00] G. A. Holzapfel. *Nonlinear Solid Mechanics: A Continuum Approach for Enineering*. Wiley, 2000.

[Huan12] J. Huang, T. Li, C. C. Foo, et al. Giant, voltage-actuated deformation of a dielectric elastomer under dead load. *Applied Physics Letters*, 100(4), 2012.

[Hugh78] T. J. R. Hughes, T. K. Caughey, and W. K. Liu. Finite-element methods for nonlinear elastodynamics which conserve energy. *Journal of Applied Mechanics*, 45(2):366–370, 1978.

[Hugh80] T. J. R. Hughes. Generalization of selective integration procedures to anisotropic and nonlinear media. *International Journal for Numerical Methods in Engineering*, 15(9):1413–1418, 1980.

[Imam17] H. Imamura, K. Kadooka, and M. Taya. A variable stiffness dielectric elastomer actuator based on electrostatic chucking. *Soft Matter*, 13:3440–3448, 2017.

[Jord10a] C. Jordi, S. Michel, and E. Fink. Fish-like propulsion of an airship with planar membrane dielectric elastomer actuators. *Bioinspiration and Biomimetics*, 5(2), 2010.

[Jord10b] C. Jordi, S. Michel, G. Kovacs, et al. Scaling of planar dielectric elastomer actuators in an agonist-antagonist configuration. *Sensors and Actuators A: Physical*, 161:182–190, 2010.

[Jung05] O. Junge, J. E. Marsden, and S. Ober-Blöbaum. Discrete mechanics and optimal control. *IFAC Proceedings Volumes*, 38(1):538–543, 2005.

[Kaal11] W. Kaal and S. Herold. Electroactive polymer actuators in dynamic applications. *IEEE/ASME Transactions on Mechatronics*, 16(1):24–32, 2011.

[Kali97] M. Kaliske and H. Rothert. On the finite element implementation

of rubber-like materials at finite strains. *Engineering Computations*, 14(2):216–232, 1997.

[Kepl10] C. Keplinger, M. Kaltenbrunner, N. Arnold, et al. Röntgen's electrode-free elastomer actuators without electromechanical pull-in instability. In *Proceedings of the National Academy of Sciences of the United States of America*, vol. 107, pp. 4505–4510, 2010.

[Klas11] M. Klassen, B.-X. Xu, and R. Müller. Numerical modelling and optimization aspects of soft dielectric actuators. In *Proceedings in Applied Mathematics and Mechanics*, vol. 11, pp. 477–478, 2011.

[Klas13] M. Klassen, B.-X. Xu, and R. Müller. The influence of incompressibility on the microstructure of dielectric elastomers. In *Proceedings of the 84th Annual Meeting of the International Association of Applied Mathematics and Mechanics (GAMM)*, vol. 13, 2013.

[Klas16] M. Klassen. *Numerical Modeling for the Static and Dynamic Analysis of Nearly Incompressible Dielectric Elastomers*. Ph.D. thesis, University of Kaiserslautern, 2016.

[Klin13] S. Klinkel, S. Zwecker, and R. Müller. A solid shell finite element formulation for dielectric elastomers. *Journal of Applied Mechanics*, 80(2), 2013.

[Kofo03] G. Kofod, P. Sommer-Larsen, R. D. Kornbluh, et al. Actuation response of polyacrylate dielectric elastomers. *Journal of Intelligent Material Systems and Structures*, 14(12):787–793, 2003.

[Kofo05] G. Kofod and P. Sommer-Larsen. Silicone dielectric elastomer actuators: Finite-elasticity model of actuation. *Sensors and Actuators A: Physical*, 122(2):273–283, 2005.

[Kofo07] G. Kofod and W. Wirges. Energy minimization for self-organized structure formation and actuation. *Applied Physics Letters*, 90(8), 2007.

[Kofo08] G. Kofod. The static actuation of dielectric elastomer actuators: how does pre-stretch improve actuation? *Journal of Physics D: Applied Physics*, 41(21), 2008.

[Korn07] R. D. Kornbluh, R. E. Pelrine, Q. Pei, et al. Electroactive polymer animated devices. *United States Patent 7,211,937 B2*, 2007.

[Kova09] G. Kovacs, L. Düring, S. Michel, et al. Stacked dielectric elastomer actuator for tensile force transmission. *Sensors and Actuators A: Physical*, 155:299–307, 2009.

[LaBu75] R. A. LaBudde and D. Greenspan. Energy and momentum conserving methods of arbitrary order for the numerical integration of equations of motion. I. Motion of a single particle. *Numerische Mathematik*, 25(4):323–346, 1975.

[LaBu76] R. A. LaBudde and D. Greenspan. Energy and momentum conserving methods of arbitrary order for the numerical integration of equations of motion. II. Motion of a system of particles. *Numerische Mathematik*, 26(1):1–16, 1976.

[Lake04] R. S. Lakes. Viscoelastic measurement techniques. *Review of Scientific Instruments*, 75(4), 2004.

[Land84] L. D. Landau and E. M. Lifshitz. *Electrodynamics of continuous media*. Pergamon Press, 1984.

[Lars13] T. Larson and L. Toth. Electro active compression bandage. *United States Patent 8,517,963 B2*, 2013.

[Lew03] A. Lew, J. E. Marsden, M. Ortiz, et al. Asynchronous variational integrators. *Archive for Rational Mechanics and Analysis*, 167(2):85–146, 2003.

[Lew04] A. Lew, J. E. Marsden, M. Ortiz, et al. Variational time integrators. *International Journal for Numerical Methods in Engineering*, 60(1):153–212, 2004.

[Leye08a] S. Leyendecker, P. Betsch, and P. Steinmann. The discrete null space method for the energy consistent integration of constrained mechanical systems. Part III: Flexible multibody dynamics. *Multibody System Dynamics*, 19(1):45–72, 2008.

[Leye08b] S. Leyendecker, J. E. Marsden, and M. Ortiz. Variational integrators for constrained dynamical systems. *Journal of Applied Mathematics and Mechanics*, 88:677–708, 2008.

[Leye09] S. Leyendecker, S. Ober-Blöbaum, J. E. Marsden, et al. Discrete mechanics and optimal control for constrained systems. *Optimal Control Applications and Methods*, 2009.

[Leye11] S. Leyendecker. *On optimal control simulations for mechanical systems*. Habilitation thesis, Chair of Applied Mechanics, University of Erlangen-Nuremberg, 2011.

[Li11] B. Li, H. Chen, J. Qiang, et al. Effect of mechanical pre-stretch on the stabilization of dielectric elastomer actuation. *Journal of Physics D: Applied Physics*, 44(15), 2011.

[Loch07] P. Lochmatter, G. Kovacs, and P. Ermanni. Design and characterization of shell-like actuators based on soft dielectric electroactive polymers. *Smart Materials and Structures*, 16(4):1415–1422, 2007.

[Lotz11] P. Lotz, M. Matysek, and H. F. Schlaak. Fabrication and application of miniaturized dielectric elastomer stack actuators. *IEEE/ASME Transactions on Mechatronics*, 16(1):58–66, 2011.

[Löwe05] C. Löwe, X. Zhang, and G. Kovacs. Dielectric elastomers in actuator technology. *Advanced Engineering Materials*, 7(5):361–367, 2005.

[Lu12] T.-Q. Lu and Z. Suo. Large conversion of energy in dielectric elastomers by electromechanical phase transition. *Acta Mechanica Sinica*, 28(4):1106–1114, 2012.

[Maas11] R. Maas, T. Siebert, and S. Leyendecker. On the relevance of structure preservation to simulations of muscle actuated movements. *Biomechanics and Modeling in Mechanobiology*, 2011.

[Maas12] R. Maas and S. Leyendecker. Optimal control of biomechanical motion using physiologically motivated cost functions. In *Proceedings of the 2nd Joint International Conference on Multibody System Dynamics*, 2012.

[Maco94] C. W. Macosko. *Rheology: Principles, Measurements, and Applications*. Wiley, 1994.

[Mars94] J. E. Marsden and T. J. R. Hughes. *Mathematical Foundations of Elasticity*. Dover Publications, 1994.

[Mars01] J. E. Marsden and M. West. Discrete mechanics and variational integrators. *Acta Numerica*, 10:357–514, 2001.

[Maug88] G. A. Maugin. *Continuum mechanics of electromagnetic solids*. Elsevier, 1988.

[McMe05] R. M. McMeeking and C. M. Landis. Electrostatic forces and stored energy for deformable dielectric materials. *Journal of Applied Mechanics*, 72(4):581–590, 2005.

[McMe07] R. M. McMeeking, C. M. Landis, and S. M. Jimenez. A principle of virtual work for combined electrostatic and mechanical loading of materials. *International Journal of Non-Linear Mechanics*, 42(6):831–838, 2007.

[MF11] J. Munch-Fals, M. Y. Benslimane, P. Gravesen, et al. Electro active elastic compression bandage. *United States Patent 7,868,221 B2*, 2011.

[Mich10] S. Michel, X. Zhang, M. Wissler, et al. A comparison between silicone and acrylic elastomers as dielectric materials in. *Polymer International*, 59:391–399, 2010.

[Mieh94] C. Miehe. Aspects of the formulation and finite element implementation of large strain isotropic elasticity. *International Journal for Numerical Methods in Engineering*, 37(12):1981–2004, 1994.

[Mock06] E. M. Mockensturm and N. Goulbourne. Dynamic response of dielectric elastomers. *International Journal of Non-Linear Mechanics*, 41(3):388–395, 2006.

[Müll10] R. Müller, B.-X. Xu, D. Gross, et al. Deformable dielectrics – optimization of heterogeneities. *International Journal of Engineering Science*, 48(7):647–657, 2010.

[Müll12] R. Müller, M. Klassen, and B.-X. Xu. Numerical modeling aspects of dielectric elastomer actuators. *Proceedings in Applied Mathematics and Mechanics*, 12:409–410, 2012.

[Noce99] J. Nocedal and S. J. Wright. *Numerical Optimization*. Springer, 1999.

[Noce09] J. Nocedal, A. Wächter, and R. A. Waltz. Adaptive barrier update strategies for nonlinear interior methods. *SIAM Journal on Optimization*, 19(4):1674–1693, 2009.

[OB08] S. Ober-Blöbaum. *Discrete Mechanics and Optimal Control*. Ph.D. thesis, Fakultät für Elektrotechnik, Informatik und Mathematik der Universität Paderborn, 2008.

[OB11] S. Ober-Blöbaum, O. Junge, and J. E. Marsden. Discrete mechanics and optimal control: An analysis. *ESAIM: Control, Optimisation and Calculus of Variations*, 17(2):322–352, 2011.

[Oden82] J. T. Oden and N. Kikuchi. Finite element methods for constrained problems in elasticity. *International Journal for Numerical Methods in Engineering*, 18(5):701–725, 1982.

[Pao78] Y.-H. Pao. Electromagnetic forces in deformable continua. *Mechanics today*, 4:209–305, 1978.

[Pari03] H. Parisch. *Festkörper-Kontinuumsmechanik*. Springer, 2003.

[Park12] H. S. Park, Z. Suo, J. Zhou, et al. A dynamic finite element method for inhomogeneous deformation and electromechanical instability of dielectric elastomer transducers. *International Journal of Solids and Structures*, 49:2187–2194, 2012.

[Pelr98] R. E. Pelrine, R. D. Kornbluh, and J. P. Joseph. Electrostriction of polymer dielectrics with compliant electrodes as a means of actuation. *Sensors and Actuators A: Physical*, 64:77–85, 1998.

[Pelr02] R. E. Pelrine, R. D. Kornbluh, Q. Pei, et al. Dielectric elastomer artificial muscle actuators: toward biomimetic motion. In *Electroactive Polymer Actuators and Devices (EAPAD)*, vol. 4695, pp. 126–137, 2002.

[Plan06] J.-S. Plante and S. Dubowsky. Large-scale failure modes of dielectric elastomer actuators. *International Journal of Solids and Structures*, 43:7727–7751, 2006.

[Pour14] S. Pourazadi, S. Ahmadi, and C. Menon. Towards the development of active compression bandages using dielectric elastomer actuators. *Smart Materials and Structures*, 23(6), 2014.

[Reit13a] S. Reitelshöfer, M. Landgraf, J. Franke, et al. Qualification of dielectric elastomer actuators as artificial muscles for highly dynamical n-dof robot kinematics. In *Proceedings of the 6th International Symposium on Adaptive Motion of Animals and Machines*, 2013.

[Reit13b] S. Reitelshöfer, M. Landgraf, T. Schlögl, et al. Qualifying dielectric elastomer actuators for usage in complex and compliant robot kinematics. In *Proceedings of the International Conference on*

Electromechanically Active Polymer (EAP) transducers & artificial muscles, 2013.

[Reit14] S. Reitelshöfer, M. Landgraf, I. Yoo, et al. Dielectric elastomer actuators – on the way to new actuation-systems driving future assistive, compliant and safe robots and prostheses. In *Biomedical Robotics and Biomechatronics (2014 5th IEEE RAS EMBS International Conference on*, pp. 803–808, 2014.

[Reit16] S. Reitelshöfer, M. Göttler, P. Schmidt, et al. Aerosol-jet-printing silicone layers and electrodes for stacked dielectric elastomer actuators in one processing device. In Y. Bar-Cohen and F. Vidal, eds., *Electroactive Polymer Actuators and Devices (EAPAD)*, vol. 9798, 2016.

[Rizz15] G. Rizzello, M. Hodgins, D. Naso, et al. Modeling and experimental validation of the effects of the electrical dynamics on the high-frequency electromechanical response of a mass–spring loaded deap circular actuator. *Smart Materials and Structures*, 24(9), 2015.

[Rudy12] S. Rudykh, K. Bhattacharya, and G. deBotton. Snap-through actuation of thick-wall electroactive balloons. *International Journal of Non-Linear Mechanics*, 47(2):206–209, 2012.

[Schl14a] T. Schlögl and S. Leyendecker. Electrostatic-elastodynamic finite element modelling of stacked dielectric actuators. In *Proceedings of the International Conference on Electromechanically Active Polymer (EAP) transducers & artificial muscles*. Linköping, 2014.

[Schl14b] T. Schlögl, S. Leyendecker, S. Reitelshöfer, et al. On modelling and simulation of dielectric elastomer actuators via electrostatic-elastodynamic coupling. In *Proceedings of the 3rd Joint International Conference on Multibody System Dynamics*, 2014.

[Schl16a] T. Schlögl and S. Leyendecker. Comparison of non-locking incompressible multi-field finite element models for dielectric actuators. In *Proceedings of the International Conference on Electromechanically Active Polymer (EAP) transducers & artificial muscles*, 2016.

[Schl16b] T. Schlögl and S. Leyendecker. Dynamic simulation of dielectric elastomer actuated multibody systems. In *Proceedings of the ASME 2016 Conference on Smart Materials, Adaptive Structures and Intelligent Systems*, 2016.

[Schl16c] T. Schlögl and S. Leyendecker. Electrostatic–viscoelastic finite element model of dielectric actuators. *Computer Methods in Applied Mechanics and Engineering*, 299:421–439, 2016.

[Schl17] T. Schlögl and S. Leyendecker. A polarisation based approach to model the strain dependent permittivity of dielectric elastomers. *Sensors and Actuators A: Physical*, 267:156–163, 2017.

[Shke96] Y. M. Shkel and D. J. Klingenberg. Material parameters for electrostriction. *Journal of Applied Physics*, 80(8), 1996.

[Shke98] Y. M. Shkel and D. J. Klingenberg. Electrostriction of polarizable materials: Comparison of models with experimental data. *Journal of Applied Physics*, 83(12), 1998.

[Sole10] M. Soleimani and C. Menon. Preliminary investigation of a balloon-shape actuator based on electroactive elastomers. *Smart Materials and Structures*, 19(4), 2010.

[Sund92] V. Sundar and R. E. Newham. Electrostriction and polarization. *Ferroelectrics*, 135:431–446, 1992.

[Suo08] Z. Suo, X. Zhao, and W. H. Greene. A nonlinear field theory of deformable dielectrics. *Journal of the Mechanics and Physics of Solids*, 56(2):467–486, 2008.

[Suo10] Z. Suo. Theory of dielectric elastomers. *Acta Mechanica Solida Sinica*, 23(6):549–578, 2010.

[Torn14] F. Tornabene, N. Fantuzzi, and M. Bacciocchi. The strong formulation finite element method: stability and accuracy. *Frattura ed Integritá Strutturale*, 29:251–265, 2014.

[Toup56] R. A. Toupin. The elastic dielectric. *Journal of Rational Mechanics and Analysis*, 5(6):849–915, 1956.

[Toup62] R. A. Toupin. Elastic materials with couple-stresses. *Archive for Rational Mechanics and Analysis*, 11(1):385–414, 1962.

[Triv08] D. Trivedi, C. D. Rahn, W. M. Kier, et al. Soft robotics: Biological inspiration, state of the art, and future research. *Applied Bionics and Biomechanics*, 5(3):99–117, 2008.

[Tröl13] A. Tröls, A. Kogler, R. Baumgartner, et al. Stretch dependence of the electrical breakdown strength and dielectric constant of dielectric elastomers. *Smart Materials and Structures*, 22(10), 2013.

[vS92] O. von Stryk and R. Bulirsch. Direct and indirect methods for trajectory optimization. *Annals of Operations Research*, 37(1):357–373, 1992.

[Vu07a] D. K. Vu and P. Steinmann. Nonlinear electro- and magneto-elastostatics: Material and spatial settings. *International Journal of Solids and Structures*, 44:7891–7905, 2007.

[Vu07b] D. K. Vu, P. Steinmann, and G. Possart. Numerical modelling of non-linear electroelasticity. *International Journal for Numerical Methods in Engineering*, 70(6):685–704, 2007.

[Vu10] D. K. Vu and P. Steinmann. A 2-D coupled BEM–FEM simulation of electro-elastostatics at large strain. *Computer Methods in Applied Mechanics and Engineering*, 199:1124–1133, 2010.

[Vu12a] D. K. Vu. *A study on nonlinear electro-elastostatics: Theory and numerical simulation.* Habilitation thesis, Chair of Applied Mechanics, University of Erlangen-Nuremberg, 2012.

[Vu12b] D. K. Vu and P. Steinmann. On 3-D coupled BEM–FEM simulation of nonlinear electro-elastostatics. *Computer Methods in Applied Mechanics and Engineering*, 201-204:82–90, 2012.

[Wäch02] A. Wächter. *An Interior Point Algorithm for Large-Scale Nonlinear Optimization with Applications in Process Engineering.* Ph.D. thesis, Carnegie Mellon University, Pittsburgh, PA, USA, 2002.

[Wäch05a] A. Wächter and L. T. Biegler. Line search filter methods for nonlinear programming: Local convergence. *SIAM Journal on Optimization*, 16(1):32–48, 2005.

[Wäch05b] A. Wächter and L. T. Biegler. Line search filter methods for nonlinear programming: Motivation and global convergence. *SIAM Journal on Optimization*, 16(1):1–31, 2005.

[Wäch06] A. Wächter and L. T. Biegler. On the implementation of an

interior-point filter line-search algorithm for large-scale nonlinear programming. *Mathematical Programming*, 106(1):25–57, 2006.

[Weis06] J. A. Weiss, B. N. Maker, and S. Govindjee. Finite element implementation of incompressible, transversely isotropic hyperelasticity. *Computer Methods in Applied Mechanics and Engineering*, 135(1):107–128, 1006.

[Wiss05] M. Wissler and E. Mazza. Modeling of a pre-strained circular actuator made of dielectric elastomers. *Sensors and Actuators A: Physical*, 120(1):184–192, 2005.

[Wiss07a] M. Wissler. *Modeling dielectric elastomer actuators*. Ph.D. thesis, Swiss Federal Institute of Technology, Zurich, 2007.

[Wiss07b] M. Wissler and E. Mazza. Electromechanical coupling in dielectric elastomer actuators. *Sensors and Actuators A: Physical*, 138:384–393, 2007.

[Wrig08] P. Wriggers. *Nonlinear Finite Element Methods*. Springer, 2008.

[Xu10] B.-X. Xu, R. Müller, M. Klassen, et al. On electromechanical stability analysis of dielectric elastomer actuators. *Applied Physics Letters*, 97, 2010.

[Xu12] B.-X. Xu, R. Müller, A. Theis, et al. Dynamic analysis of dielectric elastomer actuators. *Applied Physics Letters*, 100, 2012.

[Yamw02] T. Yamwong, A. M. Voice, and G. R. Davies. Electrostrictive response of an ideal polar rubber. *Journal of Applied Physics*, 91(3), 2002.

[Zhan02] Q. M. Zhang, H. Li, M. Poh, et al. An all-organic composite actuator material with a high dielectric constant. *Nature*, 419:284–287, 2002.

[Zhan05] B. X. Zhang, C. Löwe, M. Wissler, et al. Dielectric elastomers in actuator technology. *Advanced Engineering Materials*, 7(5):361–367, 2005.

[Zhao07] X. Zhao and Z. Suo. Method to analyze electromechanical stability of dielectric elastomers. *Applied Physics Letters*, 91(6), 2007.

[Zhao08] X. Zhao and Z. Suo. Electrostriction in elastic dielectrics undergoing large deformation. *Journal of Applied Physics*, 104(12), 2008.

[Zhao10] X. Zhao and Z. Suo. Theory of dielectric elastomers capable of giant deformation of actuation. *Physical Review Letters*, 104(17), 2010.